NUMERICAL MODELLING OF LOW TEMPERATURE RADIO-FREQUENCY HYDROGEN PLASMAS

A thesis for the degree of
PHILOSOPHIAE DOCTOR

Presented to
DUBLIN CITY UNIVERSITY

By
ROBERTO ZORAT
School of Physical Sciences
Dublin City University

Research Supervisors:
Dr. David Vender and Prof. Miles M. Turner

External Examiner: Prof. Jean-Pierre Boeuf
Internal Examiner: Dr. Albert R. Ellingboe

July 2003

Declaration

I hereby certify that this material, which I now submit for assessment on the programme of study leading to the award of Philosophiae Doctor is entirely my own work and has not been taken from the work of others save and to the extent that such work has been cited and acknowledged within the text of my work.

Signed: Roberto Zorat

Roberto Zorat

ID No: 97971200

Date: 17/09/03

Acknowledgments

I thank all people who have supported me and my work in several ways since I started my activity in DCU. I had the privilege to work with Dr. David Vender for most of the duration of my project. I appreciated his professional and human qualities and his valuable guidance has been an important factor in the development of the project. Prof. Miles Turner also gave a very important contribution to my project with his valuable advice and help. In the first year of my project Dr. Jonathan Goss proactively helped me to address some problems in the global model code. Dr. Deirdre Boilson and Deborah O'Connell collaborated with me by performing the experimental measurements, whose results are compared in this thesis with some of the results of my models. Dr. Mike Hopkins and Dr. Bert Ellingboe, the heads of the Plasma Research Laboratory (PRL) during my permanence in the group, set and kept favourable conditions for the accomplishment of my project and obtained funding for it from the European Union under EURATOM Contract. Samantha Fahy and Deirdre O'Riordan, the project managers of the group during my permanence in PRL, and all secretaries who worked with them always acted proactively and efficiently to sort out problems affecting my activity in PRL. Apart from the present or former PRL members already mentioned I thank Brendan, Neil, Declan, Kevin, Michelle, Catherine, Annalisa, George, Mike, Patrick, Bernard, Angus, Paul, Felipe, Ronan, Jim, Andrew, Shane, David, Taghrid, Timo, Jerome, Chanel, Peter and Niall for the nice moments shared. The same goes for the members of the School of Physical Sciences and the other people I have been in touch with here in Ireland, there are too many to be mentioned here. Finally and most importantly, my parents, who always have absolutely encouraged and supported me in pursuing my studies, and my brother.

Contents

List of Figures

List of Tables

Abstract

In this thesis low temperature hydrogen radio frequency (rf) plasmas discharges are modelled numerically by using both a global model and a Particle-In-Cell (PIC) simulation. Such plasmas are of interest because of their industrial applications and for the development of negative ion sources for fusion plasmas. The global model technique was adapted and then implemented to model rf inductively coupled hydrogen plasma discharges created in the DENISE experiment, with particular attention to the negative ion chemistry. For negative ions, assumed to be mainly produced by dissociative attachment, the densities obtained are always far less than 0.1 of the electron density even under the most favourable assumptions. A new numerical scheme coupling the PIC and the global model methods was devised and implemented to model rf capacitively coupled hydrogen plasma discharges, including the effects of the chemistry in the discharge. In the scheme a PIC code and a suitably modified version of the global model code are made interact by exchanging information. The global model adds the ability to handle the neutral species kinetics to the self-consistent simulation of the charged species particles of the PIC model. The scheme was used to calculate the energy cost per electron-ion pair created in plasmas with non-Maxwellian electron energy distributions. The energy losses obtained are much less than the values calculated by assuming a Maxwellian distribution with the same electron average thermal energy. The scheme was also used to obtain the energy distribution function of positive ions arriving at the electrodes. Some distributions are compared with the energy distributions measured in the CIRIS experiment, giving a reasonable agreement. Finally, negative ions were included in the simulation of rf capacitively coupled H_2 plasma discharges and the numerical scheme was used to model self-consistently their production by dissociative attachment of $H_2(0 \leq v \leq 9)$.

Chapter 1

Introduction

1.1 The plasma state of matter

If matter in the gaseous state is heated above a certain temperature, it assumes the plasma state, also called the fourth state of the matter (the other three being obviously solid, liquid and gas). A plasma is composed of charged particles whose typical thermal kinetic energy is much bigger than the typical potential energy between any of those particles and one of the other ones closest to it. Elements of plasma can interact even at large distances due to the long ranged Coulomb force, that varies with distance as $1/r^2$, and for this reason their dynamics does not depend only on local conditions. In this sense plasmas can exhibit a collective behaviour [1].

The effect of the charged particles on their dynamics is the maintenance of charge neutrality on a length scale comparable with the volume occupied by the gas itself. If a test charge is at rest and immersed in a plasma, its electrostatic potential will attract the particles having charge of the opposite sign and repel the particles having charge of the same sign until a new equilibrium state is reached, with the electrostatic potential of the test charge screened by the

plasma in the surrounding region.

The Debye length

$$\lambda_D = \left(\frac{\varepsilon_0 T}{e^2 n}\right)^{\frac{1}{2}} \tag{1.1}$$

is a distance at which the electrostatic potential of the test charge has not been screened completely by the surrounding plasma. The number of particles included in a sphere, having as radius the Debye length of the plasma, is called the plasma parameter, which is defined as

$$\Lambda = \frac{4}{3}\pi\lambda_D^3 n \tag{1.2}$$

The bigger Λ in the region close to the test charge, the more effective the screening of the plasma on the electrostatic potential of the test charge. The averaged charge density in a plasma may be appreciably non-zero over a Debye length. In equation 1.1, T and n are respectively the species temperature and density of the relevant particle species.

The plasma or Langmuir oscillations are the mechanism responsible for the maintenance of the macroscopic charge neutrality of the plasma. The plasma frequency

$$\omega_p = \left(\frac{e^2 n}{\varepsilon_0 m_e}\right)^{\frac{1}{2}}, \tag{1.3}$$

indicates how fast those oscillations are. In equation 1.3, ε_0 is the dielectric constant and e and m_e are the electronic charge and mass. The time averaged charge density in a plasma may be appreciably non-zero over a time interval proportional to the inverse of the plasma frequency.

Plasmas have been attracting scientific interest and research in physics for more than a century and their study is important both for having a more complete understanding of Nature and for improving and creating many useful technologies requiring the use of plasmas.

Most of the matter in the universe is in the plasma state. The sun, the other stars, the interstellar matter, the solar wind all contain matter in the plasma state. The Earth's magnetosphere and ionosphere also contain plasma. Despite its abundance outside our planet, generally matter is not found naturally in the plasma state on Earth, therefore plasma production is a prerequisite, and a complication, for its laboratory study.

1.2 Artificial plasmas

1.2.1 Fusion plasmas

After World War II a special interest in plasma physics began to rise with the attempts within many research programmes worldwide to develop a controlled thermonuclear fusion reactor, as a source of energy able to satisfy the industrialised world increasing energy demand in in an alternative way. For the following decades the research efforts of much of the plasma physics community focused on the challenge of devising reactor configurations suitable for energy production. The idea is to produce a plasma that will generate more energy through fusion reactions, than is required to create and sustain that plasma. Such a plasma should have an ion temperature, T_i, high enough and must satisfy the Lawson criterion, which requires that the product of the ion density, n_i, times the energy confinement time, τ_E, exceeds a certain function of T_i. For deuterium-tritium fusion it should be $T_i \sim$ 10-30 keV and $n_i \tau_E \geq 2 \times 10^{20}$ m^{-3} s [2, p. 189]. Two main methods were proposed to produce fusion plasmas satisfying those conditions.

In the first approach laser or high energy particle beams are used to strongly compress and heat a deuterium-tritium fuel pellet so fast that some thermonuclear fusion reactions are produced before the fuel is blown apart [3]. This

method is called inertial confinement, because the inertia of the fuel itself would be used to confine it long enough to produce the desired fusion reactions. For inertial confinement the compressed ion density can be 10^{31} m^{-3} over a time interval of 10^{-9} s. In the second method, called magnetic confinement, charged particles are confined by certain magnetic field configurations, generally toroidal, in order to keep them isolated from the walls, while various methods may be used to heat it. For magnetic confinement the ion densities are restricted to 10^{21} m^{-3} with a required $\tau_E \sim 1$ s. Although huge progress has been made in the field, the construction of a controlled thermonuclear fusion reactor that could be used as an economically viable source of energy is still several decades off.

1.2.2 Processing plasmas

In the last few decades, plasmas, whose temperatures are much lower than the millions degree Celsius of fusion plasmas, have been used for a wide range of industrial applications in materials processing. One of the best known fields where plasma processing technologies are widely used is the semiconductor processing for the microelectronics components manufacturing [4, 5]. Possible uses of plasma technologies for materials processing are surface treatment, etching, thin film deposition, processing of industrial waste, etc. In plasma treatment of surfaces, plasma technologies allow new products to be conceived which would be impossible to make with more traditional manufacturing processes. Moreover, plasma is accepted as a suitable environmentally friendly process technology, producing very low levels of industrial waste, especially when compared with the more traditional liquid chemical treatments [2, p. 339].

1.2.3 Plasmas for other applications

In addition, low temperature plasmas are used for other industrial applications. Two of the best known are lighting sources and plasma display panels.

Non-equilibrium plasmas are used to convert electrical energy into light in the widespread fluorescent lamps and neon signs [6]. The desired light is produced in a glow discharge, that usually may contain argon, mercury, neon or sodium gas. Local thermodynamic equilibrium (LTE) and near-LTE plasmas are widely used for lighting as well [7]. Their main advantage is that they are much more efficient in converting electrical energy into light than the conventional incandescent lamps. High-pressure mercury or sodium lamps and metal halide arc lamps are examples of LTE and near-LTE plasma discharge lamps.

Plasma display panels make use of lightly ionized glow discharges to produce light and perform switching and selection functions, or both [8] on each of their picture elements (pixels). In recent years alternate current (ac) dielectric barrier discharges have been used to produce microdischarge plasmas, whose emitted UV photons excite phosphor elements, which produce the light to be emitted form each pixel of the display [9]. These displays may be used for high quality television monitors.

1.3 Producing and sustaining plasmas

To produce artificial plasmas it is necessary to supply enough energy to a gas to create a sufficient number of charge carriers by ionisation. In order to achieve that, the most widely used method is based on the application of an electric field in the space where the gas is present. The field accelerates the charged particles initially present in the gas and an electrical breakdown eventually

produces the plasma. Charged particles accelerated by the electric field couple their energy into the plasma via collisions with other particles.

In direct current (dc) discharges a constant voltage is applied between two electrodes in a closed vessel. Different type of discharges can be obtained depending on the values of the applied voltage and of the current in the discharge [10]. Pulse discharges differ from dc discharges because they are not produced by a constant applied voltage, but by a pulsed voltage that is different than zero only for a certain fraction of its period. That offers extra control on the features and the behaviour of the plasma to be produced for the intended applications.

Plasmas can be obtained and sustained by applying a varying electric field as well, which can be produced in a number of ways. In radio-frequency (rf) capacitive discharges a driving ac voltage, having a certain frequency, typically 13.56 MHz, is applied between two electrodes and a plasma will be created between them. For etching applications a magnetic field parallel to the electrodes may be added to increase the plasma density and reduce the voltage between the bulk plasma and either electrode [11].

In rf inductively coupled discharges the coupling of the rf power to the plasma is made through a dielectric window, while in rf capacitive discharges is made directly through electrodes. That causes the sheath voltage, and therefore the energy gained by positive ions crossing the sheath, to be significantly lower in inductive discharges than in capacitive discharges. Consequently, higher plasma densities are reached in inductive discharges than in capacitive discharges, with the same values of the control parameters of the discharges.

An alternating current in the radio frequency range is applied to a coil near but out of the chamber containing the conducting plasma, producing a time-varying magnetic field, which produces in turn the time-varying electric

field accelerating the charge carriers in the plasma. Other different methods of coupling the supplied power to the plasma through a dielectric window were devised and implemented in electron cyclotron resonance (ECR), helicon and helical resonator discharges [11]. The first two of these three kind of plasma sources need the presence of a dc magnetic field, while the last one does not.

Plasmas for fusion magnetically confined in toroidal geometry may be produced by the energy deposited through ohmic heating, caused mainly by a strong toroidal current produced by induction in the plasma, being the secondary circuit of a transformer. The plasma is confined by a strong toroidal magnetic field produced by permanent magnets and a poloidal magnetic field produced by the toroidal plasma current. Beyond a certain temperature ohmic heating becomes less effective because of the decreasing resistivity of the plasma with increasing temperature and therefore some other heating method must be used for reaching the temperatures above 10 keV needed for obtaining thermonuclear fusion in a tokamak plasma. The two additional plasma heating methods most used in current large tokamak experiments are the radio-frequency and the Neutral Beam Injection (NBI) methods [2, p. 391].

In the radio-frequency heating method a high power electromagnetic wave is directed at the plasma. Part of the wave energy may be absorbed by the plasma through collisions, but to have an effective absorption the wave has to be tuned at some resonant frequency at which collisionless absorption can also take place [12].

In the NBI method a beam of energetic neutral particles are directed at the fusion plasma and deposit their energy on it through collisions. The particles of the beam need to be neutrals when they enter the region where the confining magnetic field is present, because charged particles trajectories may be strongly modified by the magnetic field. To make the plasma reach the temperature

needed for fusion the beam must have a high energy, which can be obtained by acceleration of charged particles moving in a region where there is a high electric potential difference. Therefore, a sufficient number of ion particles must be produced in ion sources, then accelerated and neutralized before they reach the confining magnetic field.

1.4 Ion sources for NBI systems for fusion

Significant advances have been made in recent years in the development of high power ion sources to be used in NBI systems for plasma heating in the largest tokamak experiments worldwide. Currently NBI systems have been developed which can deliver several tens of MW through neutral beams with energies of the order of 100 keV [13].

The NBI system for the next generation magnetic fusion device, International Thermonuclear Experimental Reactor (ITER) [14], is planned to have two injectors, each delivering a deuterium beam of 16.5 MW (total 33 MW), with energy of 1 MeV. This is one order of magnitude higher than the positive ion based NBI capabilities [13]. It has been verified that at such a high beam energy only a small fraction of the positive ions can be neutralized and therefore positive ion based NBI systems are not a viable choice. That leaves negative ions as the only possible kind of particle to be used in the NBI for ITER before neutralisation, because negative ions have a neutralisation efficiency as high as 60 % at the required beam energy [13, 15].

Study of negative ion sources started in the 1960's, but only several years ago a negative ion source, which can produce a beam with the current of more than 10 A required for the NBI system, has been developed [13]. A lot of research has been done on H^- in hydrogen plasma discharges, because hydrogen can be found in nature more easily than deuterium, although the

negative ion species of the particles to be produced in the NBI system for ITER is D^-.

Towards the end of the 1970's, following measurements of unexpectedly high negative ion densities in low pressure hydrogen and deuterium plasmas [16], it was shown that such negative ions may be produced in large quantities by dissociative attachment of vibrationally excited molecules. That observation led to the development of the so called tandem negative ion sources [17], which are optimized for negative ion production through that mechanism. In that kind of source a magnetic filter was introduced to prevent energetic electrons, useful for creating the vibrationally excited molecules, from entering the region where negative ions are produced (by less energetic electrons), because it had been already noticed that negative ions may be effectively lost through collisions with energetic electrons. Early prototypes of tandem sources produced encouraging current densities of negative ions, but in larger tandem sources the current densities obtained were much smaller [18].

In the early 1970's it was shown that adding cesium on a metal surface in a chamber where a hydrogen discharge is created increases the H^- production. The explanation for this is that the work function on the surface is reduced and consequently the electron transfer from the metal to the gas improves [18]. Because of this effect the injection of cesium vapor in a discharge created in a tandem source increases the negative ion production [18, 19]. Major drawbacks for cesium injection are the high energy of the negative ions produced and the possible effects of cesium impurities in the discharge region where ions are extracted [18].

A kind of negative ion source often used is the filament driven discharge. In sources of that kind tungsten filaments are heated and negatively biased with respect to the walls of the chamber. The electrons emitted by thermionic

emission are accelerated from the filaments acting as a cathode to the walls, acting as anode. If these type of sources were to be used in NBI systems for ITER, a big operational problem would be the lifetime of the filaments, which would be too short in the conditions required. Since frequent replacement of components of the system would not be acceptable, radio-frequency heated plasma discharges have become the natural choice for the negative ion source for NBI systems for ITER. To increase the amount of negative ions produced, rf inductively coupled discharges are preferred, because the electron density and therefore the negative ion production rate are much bigger than in capacitively coupled discharges.

1.5 Computational methods for rf plasmas

Experiment, analytical theory and computer modelling are the three complementary tools available to perform studies in plasma physics, as well as in other research areas in physics. Plasma modelling through numerical methods used in calculations performed by computers is becoming more and more important and effective, because of the unceasingly increasing calculation speed of computers since their introduction in the past century. In the last few decades several numerical methods have been used to model the behaviour of rf plasma discharges at different time scales and at different levels of detail.

1.5.1 Global models

In global models [20, 21, 22, 23, 24] the species particle balance equations, the power balance equation and the quasi-neutrality condition are to be solved simultaneously. This approach allows the study of the gas-phase kinetics of rf plasma discharges having complex chemistry, with many particle species and

collision processes included in the model. The values of the averaged densities of the various species and of the electron temperature in the steady-state of the discharge are obtained by solving the set of non-linear equations for fixed values of the control parameters and of the dimensions of the discharge. Although the solution can be calculated very fast even if many species and many collision processes are included in the model, dynamic effects in rf plasma discharges can not be modelled in this way.

1.5.2 Fluid models

Fluid models [25, 26, 27] require the solution of the field equation(s) and of some of the first three moments of the Boltzmann equation for the relevant species, the continuity equation and the momentum and energy balance equations. The simplest way to truncate the otherwise infinite set of equations is to assume that the particles are in local thermodynamic equilibrium, and therefore that their velocity distribution is Maxwellian. When that assumption is not good enough it is necessary to make a different approximation about the velocity distribution function to obtain reliable results from fluid models. The physical quantities obtained from the solution of the fluid equations are the densities and the drift velocities of the simulated species, the electron temperature and the field(s) as functions of space and time. The assumption regarding the electron velocity distribution function, necessary for the truncation of the system of equations, makes the model non self-consistent. However, if kinetic effects, like the effects of stochastic heating or of secondary emission, are not very important in the rf plasma discharge modelled for the selected values of the operating conditions, fluid models can model the rf plasma discharge sufficiently well. Fluid models are not computationally very expensive.

1.5.3 Particle simulations

Particle-In-Cell (PIC) simulations [28, 29, 30, 31, 32] can provide a very detailed picture of the behaviour of the rf plasma discharge, because no assumption is made about the velocity distribution of the simulated species. In PIC simulations a certain number of computer particles, each of them representing a large number of real particles, are used to simulate the plasma. The position and the velocities of the computer particles are obtained by integration of their equations of motion and by solving at the same time the field equation(s). The price to pay for obtaining such a detailed model of the rf plasma discharge with a conventional PIC simulation is a much longer computational time, particularly for simulations performed in more than one spatial dimension. Collisions in PIC simulations may be considered only as instantaneous events and are allowed to happen only at a discrete number of points of the time axis. They are modelled with a Monte Carlo Collisions (MCC) technique [33] compatible with the PIC scheme. In this way collision-affected and collisionless particle motion are decoupled.

Another particle simulation method, generally used in the study of rarefied gas flow in aerodynamics is the Direct Simulation Monte Carlo (DSMC) technique and was also used in rf plasma discharge simulation for studying the neutral and ion flows in a high density plasma reactor [34].

1.5.4 Explicit solutions of Boltzmann's equation

The Generalized Monte Carlo Flux (GMCF) method can be used to solve Boltzmann's equation to obtain the electron distribution function in 2D simulations of capacitively coupled plasma discharges [35]. In such method the transition probabilities for electrons among velocity-space cells are calculated for different values of the ratio E/N, with E being the electric field magnitude

and N being the gas density and are then used to describe the collision and acceleration effects in the simulation.

Convective schemes [36, 37] based on propagators (Green's functions) can be used to model rf plasma discharges having simple chemistry, in the regime where convection dominates over diffusion for the simulated particles. They allow the Courant-Friedrichs-Levy (CFL) criterion on the time step not to be satisfied, as it must be in conventional PIC simulations, but the time step must be still small enough to resolve electron plasma oscillations. The CFL criterion requires that the time step used to advance the system has to be less than the time generally needed by a computational particle of the PIC to cross one of the spatial cells dividing the spatial domain.

Another approach for obtaining the electron energy distribution function, used to model the discharge region of a microwave generated plasma, requires the iterative solution of the Boltzmann's equation coupled with the species, energy and power balances [38].

1.5.5 Hybrid models

Hybrid models [39, 40, 41, 42] can be used to take into account the non-equilibrium characteristic of electron transport in fluid models of rf plasma discharges. In those models a Monte Carlo simulation is used to determine the electron energy distribution and then its transport coefficients and the electron collision rate constants in the fluid equations, but fluid models are used for the simulated species. Extra calculation modules may be used to obtain the electromagnetic field and the chemistry in the discharge [41]. In hybrid models the electron energy distribution function may also be obtained as a solution of the spatially averaged Boltzmann's equation, if the electron energy relaxation length exceeds the dimension of the chamber. The only variable of the equation

is the total electron energy. This method is the so-called Non-Local Approach (NLA) [43, 44].

1.6 Motivation and outline of the thesis

Obtaining a complete numerical modelling of the behaviour of rf plasma discharges is a very challenging task, because of the plethora of phenomena evolving on very different time scales in the complex physical system considered. The higher the level of detail of the system and the accuracy required from the numerical model, the higher the computational cost, therefore the available computational power generally limits the modelling capabilities.

Among the computational methods described in the previous section, PIC simulations are particularly attractive to model self-consistently rf plasmas, but usually neutrals are not simulated in this method, because the spatial distribution of neutrals changes and reaches a steady configuration on a much longer time scale than the charged species distribution. So, generally in PIC methods, the neutral species densities are input parameters, that do not vary with time and that are used only to include in the model the effect of simulated particle collisions with background neutral particles. By changing some of the discharge control parameters (e.g. input power, input gas concentrations in mixtures, etc.), the steady-state densities of the neutral species may change as well and in a way to affect significantly some of the physical quantities to be modelled (e.g. the electron energy distribution function, the ion flux to the wall, etc.). Effects of that kind, that may be particularly important if the plasma discharge has a complex chemistry, can not be modelled by PIC simulations where the neutral densities are assumed constant.

Finding a way to include the effects of the chemistry in the rf plasma discharge on the physical quantities of interest in a sufficiently accurate model of

the plasma itself is not an easy task and different approaches may be viable, depending on what one is interested in modelling and what is the computational power available. The simplest way would be to use just a simple global model. Another possibility is the approach suggested by Chen et al. [38], who proposed a steady-state model able to deliver the electron energy distribution function, the species densities and the gas temperature. The main problem with both of those approaches is that no information on the dynamics of the system can be obtained by using them. Another option is to couple iteratively the PIC method used for simulating charged particles and the DSMC method used for simulating the neutrals, but although this approach [45] is self-consistent and able to simulate the dynamics of neutrals on their own time scale, something that can not be done with a conventional PIC, this method is at least as computationally intensive as the corresponding PIC method simulating only the charged particles.

In this thesis a different approach for the inclusion of the chemistry effects in the model of an rf plasma discharge is defined and tested. The main idea is to couple a PIC simulation of an rf plasma, that gives a sufficiently detailed model of the system, with a suitably modified version of a global model of the simulated plasma itself, that gives a reasonably good picture of the chemistry. The two numerical codes interact iteratively by delivering information to each other until convergence to the steady state is reached. This approach not only allows to include the effects of the chemistry in a detailed model of an rf plasma discharge, but it can accelerate significantly the convergence of the simulation towards its steady-state. The focus of this thesis is the negative ion chemistry in rf hydrogen plasma discharges. The numerical scheme coupling PIC simulation and a suitably modified version of the global model has been used to model the negative ion production by dissociative attachment in a

capacitively coupled rf hydrogen plasma discharge.

In chapter 2, global models developed for studying the chemistry of rf inductively coupled hydrogen plasma discharges in the DENISE [23, 24] negative ion source are presented. The results obtained are presented, discussed and, when possible, compared with experimental measurements. In chapter 3 the PIC method and its implementation used to perform the work presented in this thesis are explained in detail. In chapter 4 the numerical scheme coupling global model and PIC simulation is explained in detail and a short demonstration of how the scheme works is given. In chapter 5 the results of several applications of the coupling scheme are presented, including the self-consistent modelling of the negative ion production by dissociative attachment of $H_2(0 \leq v \leq 9)$ in a capacitively coupled rf hydrogen plasma discharge.

Chapter 2

Global models

In this chapter the global model method for modelling rf plasma discharges will be explained thoroughly and the numerical results obtained from global models of rf hydrogen plasmas produced in the DEuterium Negative Ion Source Experiment (DENISE) [46] are presented, with particular regard to the negative ion kinetics. Comparisons of the obtained numerical results with the available experimental measurements are made when possible. The results presented are obtained from the Global Model Solver (GMS) code, created to construct and solve the set of non-linear algebraic equations characterizing the method. The content of this chapter was presented in [23, 24].

In section 2.1 the equations used in the global model method are discussed and it is mentioned how to solve them. In section 2.2 the changes made to the method in order to model an rf plasma produced in DENISE are explained. In section 2.3 the results of a first model of a plasma discharge produced in DENISE are presented together with a comparison to the available experimental data. In section 2.4 the results of a more complete model, including H^- particle species, are presented. The reasons for differences in the values of the H^- density from the results of other models are discussed.

2.1 The set of equations in a global model and their solution

Global models have been used for analysing high density discharges, such as rf driven transformer-coupled plasma sources operating in oxygen [20, 21, 47]; argon, chlorine, and argon/chlorine mixtures [21]; and for studying high pressure capacitive electronegative rf discharges [22].

The basic characteristics of the global model method [20] are that results obtained are spatial averages of physical quantities of the system in the steady state. Selected the relevant external parameter values and the collision processes involving the particles of the species modelled in the discharge, the model permits one to determine their average densities and the average electron temperature, by solving a system of non linear algebraic equations. If the global model of the discharge includes $N-1$ different particle species, then a system of N non-linear algebraic equations must be solved. This system is composed of the $N-2$ particle balance equations for all species except electrons, the power balance equation and the electrical quasi-neutrality condition. The N unknowns are the $N-1$ averaged species densities and the average electron temperature T_e.

A global model permits one to investigate the gas-phase and surface chemical kinetics for the species present in the discharge, to study the sensitivity of the results to variations of external parameters and to evaluate the importance of the various collision processes included in the model in the kinetics of the various modelled particles species of the discharge. The advantages of a global model analysis are as follows. Firstly, a large number of species and processes can be included in the model without increasing excessively the required computational cost. Secondly, cause and effect relationships can be

established between the external parameters and the averaged physical quantities obtained as the result. Its main disadvantage is that it can not be used to study the discharge structure and the plasma dynamics.

2.1.1 The particle balance equation

In the steady state, total production and loss rates averaged over a sufficiently long period of time (in our case a multiple of the rf period) must balance for all particle species present in the discharge. Therefore the most general form of the particle balance equation for the steady state of the discharge is

$$\frac{dn_i}{dt} = s_{in} + \sum_{j=1}^{N_p} a_j^p \, k_j^p \prod_{m=1}^{N_j^p} n_{jm}^p - \sum_{j=1}^{N_l} a_j^l \, k_j^l \prod_{m=1}^{N_j^l} n_{jm}^l - k_r \, n_i = 0, \qquad (2.1)$$

whose physical meaning is that production and loss rates of particles of the i-th species balance and therefore the average density of that species does not change in time. The two sums in equation 2.1 are performed over the collision processes giving respectively net production and loss of particles of the i-th species. The various terms of equation 2.1 are explained in the following of this subsection.

The effect of the particles entering the chamber has to be taken into account only in the particle balance equation of the species contained in the feedstock gas (in our case H_2). The corresponding term is proportional to the inlet flow rate S_{in}, which is usually expressed in sccm (i.e.; cm^3 per minute at standard pressure and temperature). The term is given by

$$s_{in} = 4.1025 \times 10^{23} \frac{S_{in}}{V} \qquad (2.2)$$

where V is the volume of the chamber containing the plasma expressed in cm^3.

Particles of all species included in the model are created or lost in collision processes of two general kinds: *surface processes*, which occur at the walls of

Table 2.1: Rate constants for surface processes.

Surface process	Rate constant
Ion neutralisation	$u_{B,i} \frac{A_{eff}}{V}$
Neutral de-excitation	$w \frac{D_{eff}}{\Lambda^2}$
Neutral recombination	$\gamma_{rec} \frac{D_{eff}}{\Lambda^2}$

the chamber, and *volume processes* which occur inside the chamber. The term associated with a generic collision process in the particle balance equation of a generic species is

$$\pm a\, k \prod_{m=1}^{N} n_m \tag{2.3}$$

where a is the number of particles of such species produced or lost in a single collision process, k is the rate constant of the same process, N is the number of the reactants involved, and n_m is the density of the m-th reactant. The term is positive if that process gives a net production of particles of the generic species chosen, while is negative if instead such process gives a net loss.

The pressure regime used in our modelling makes 3-body collisions unlikely. Hence, volume processes involving more than two colliding particles will not be included in the model. The rate constant, k, of volume processes is calculated by averaging the cross section $\sigma(v)$ multiplied by the scalar relative velocity v of the two colliding particles over the velocity distribution function of the respective species; i.e., $k = \langle \sigma(v)\, v \rangle$. For electron collision processes with slow neutrals or ions the electron velocity closely approximates v, so the heavy particles can be considered at rest. Therefore the average can be calculated by using the Electron Energy Distribution Function (EEDF), which for plasmas created in rf inductively coupled plasma discharges is close to Maxwellian.

The formulae for the rate constants of different kinds of surface processes are shown in table 2.1 [20, 21]. V is the chamber volume, w is the transition probability from the reactant to the product for the neutral de-excitation process in a single wall collision, u_B is the Bohm velocity of the relevant positive ion and A_{eff} is an effective area; these last two quantities are defined in subsection 2.1.2. D_{eff} is the effective diffusion coefficient describing the superposition of free Knudsen diffusion and collisional diffusion processes and it is defined by

$$\frac{1}{D_{eff}} = \frac{1}{D_{Kn}} + \frac{1}{D_{AA^*}}. \tag{2.4}$$

The Knudsen free diffusion coefficient is defined by

$$D_{Kn} = \frac{\overline{v}\Lambda}{3}; \quad \overline{v} = \left(\frac{8k_BT}{\pi M}\right)^{\frac{1}{2}} \tag{2.5}$$

where $\overline{v}$ is the average scalar velocity of particles species having mass M and temperature T, with k_B the Boltzmann constant. Λ is the effective diffusion length approximated by V/S_T [20], with S_T the area of the chamber wall surface. The diffusion coefficient D_{AA^*}, expressing the effect of collisions of the generic neutral species A with the neutral background gas species A^*, is calculated using the Chapman-Enskog equation for gas diffusivity [48]. The term γ_{rec} is the recombination coefficient at the wall and is equal to the probability that a particle of the considered neutral species is subject to a recombination process when colliding with the chamber wall.

For some species the loss term $-k_r\, n_i$, with n_i being the species density and k_r a loss rate constant, has to be included in the equation. This term is associated to the particles flowing out of the chamber and can be expressed as $k_r = S/V$. Under the hypothesis of molecular flow for particles freely exiting an orifice having cross section area A_{or} we have [49]

$$S = \frac{\overline{v}A_{or}}{4}, \tag{2.6}$$

with S being equal to the conductance of the orifice. When $A_{or}/S_T \ll 1$, a particle on average collides with the wall many times before exiting the chamber, so it is more likely that an excited neutral or a charged particle becomes a particle of a neutral ground-state species before exiting the chamber through the orifice. Therefore, this loss term is included only in the particle balance equation of a ground-state neutral species. If the gas is forced to exit the chamber by a vacuum pump, S is equal to its pumping speed.

2.1.2 The power balance equation

In the model all energy supplied to the discharge is assumed to be absorbed by the plasma. Part of the absorbed energy is used in creating electron-ion pairs through ionisation and is lost both in inelastic and elastic electron collision processes. The remaining part is lost as kinetic energy both of ions and electrons as they leave the plasma. If negative ions are included in the model some power will also be lost through volume recombination processes of positive ions. The total energy loss for a single electron-ion pair lost at the wall $\mathcal{E}_{T,i}$ is defined by

$$\mathcal{E}_{T,i} = \mathcal{E}_{i,w} + \mathcal{E}_{e,w} + \mathcal{E}_{L,i} \tag{2.7}$$

where the ion kinetic energy $\mathcal{E}_{i,w}$ and electron kinetic energy $\mathcal{E}_{e,w}$ at the wall are assumed to be [20, 21]

$$\mathcal{E}_{i,w} = e\left(V_s + \frac{T_e}{2}\right); \qquad \mathcal{E}_{e,w} = 2eT_e. \tag{2.8}$$

Here e is the elementary charge, T_e is the electron temperature expressed in eV, and V_s is the value of the average sheath voltage. For inductive discharges V_s can be obtained by equating the positive ion flux and the electron flux at the wall

$$\sum_{i=1}^{N_{pi}} n_i\, u_{B,i} = \frac{1}{4}\, n_e \left(\frac{8eT_e}{\pi m_e}\right)^{\frac{1}{2}} e^{-V_s/T_e}, \tag{2.9}$$

where N_{pi} is the number of positive ion species included in the model and m_e is the electron mass. $u_{B,i}$ is the Bohm velocity defined as

$$u_{B,i} = (eT_e/M_i)^{\frac{1}{2}}\,, \tag{2.10}$$

with M_i being the mass of the i-th positive ion. The Bohm velocity is the minimum allowed value of the positive ion velocity component directed towards the wall at the sheath edge [11, p. 158]. The value obtained for V_s in inductive discharges is a few times T_e (in capacitive discharges V_s would be significantly higher and would be calculated in a different way). The last term in the equation 2.7 is the collisional energy loss per electron-ion pair created $\mathcal{E}_{L,i}$ defined by

$$\mathcal{E}_{L,i} = \frac{\sum_{j=1}^{N_s^i} n_j^i\, k_{ij}^{pr} \left[\mathcal{E}_{ij}^{pr} + \sum_{l=1}^{N_{ij}^{inel}} \left(\frac{k_{ijl}^{inel}}{k_{ij}^{pr}}\, \mathcal{E}_{ijl}^{inel}\right) + \frac{k_{ij}^{el}}{k_{ij}^{pr}}\, \mathcal{E}_{ij}^{el}\right]}{\sum_{j=1}^{N_s^i} n_j^i\, k_{ij}^{pr}}. \tag{2.11}$$

As defined here, $\mathcal{E}_{L,i}$ includes the energy losses due to ionisation as well as all other inelastic and elastic electron collision processes. The i-th positive ion-electron pair can be created either by electron ionisation of a neutral species or by electron dissociation of a molecular ion or neutral. A process of this kind is a positive ion production process. N_s^i is the number of such processes producing a net creation of particles of the i-th positive ion species, n_j^i is the density of the species of the collision partner of the electron in the j-th positive ion production process for the i-th positive ion, k_{ij}^{pr} is the rate constant of that process and $\mathcal{E}_{ij}^{pr}$ is the average energy (expressed in Joule) lost by the colliding electron in that process. N_{ij}^{inel} is the number of other inelastic processes associated with the creation of the i-th positive ion through its j-th positive ion production process and $\mathcal{E}_{ijl}^{inel}$ and k_{ijl}^{inel} are the average electron energy lost and the rate constant of the l-th of these inelastic processes, respectively. The average energy lost by an electron in an elastic collision process with its collision partner in the

j-th positive ion production process is

$$\mathcal{E}_{ij}^{el} = \frac{2m_e}{M_j}\left(\frac{3}{2}\,e\,T_e\right), \tag{2.12}$$

where M_j the mass of the j-th species and k_{ij}^{el} is the rate constant of the elastic collision process. It has to be stressed that the individual contributions of each of the N_s^i species to $\mathcal{E}_{L,i}$ depend on their own density n_j^i.

In the steady-state, absorbed and lost power must balance, so the most general expression of the power balance equation is [20, 21]

$$P - \sum_{i=1}^{N_{pi}} n_i \left[A_{eff}\, u_{B,i}\, \mathcal{E}_{T,i} + \nu_{R,i}\, V\, \mathcal{E}_{L,i}\right] = 0. \tag{2.13}$$

P is the power absorbed by the plasma, and n_i is the density of the i-th of the N_{pi} positive ion species considered in the model. The two products in the square brackets are the power loss due to the charged particles striking the wall surface and to the ion recombination processes, that can take place only if at least one negative ion species is included in the model.

For a cylindrical plasma chamber having radius R and length L, the expression for the effective area is

$$A_{eff} = 2\,\pi\,R\,(L\,h_R + R\,h_L), \tag{2.14}$$

where

$$h_L = 0.86\left(3.0 + \frac{L}{2\lambda_i}\right)^{-\frac{1}{2}} \qquad h_R = 0.8\left(4.0 + \frac{R}{\lambda_i}\right)^{-\frac{1}{2}} \tag{2.15}$$

are the sheath to bulk density ratios of the positive ion species as calculated by Godyak [50] for an electropositive plasma in a low pressure regime, for parallel plate (h_L) and infinite cylinder (h_R) geometries, respectively. The positive ion mean free path is taken to be

$$\lambda_i = \frac{1}{n_{neu}\sigma_i} \tag{2.16}$$

with σ_i being the ion-neutral cross section in weakly ionized plasmas and n_{neu} being the total neutral density. In the model σ_i is estimated to be equal to $5.0 \times 10^{-19}\,\mathrm{m}^2$ [51], somewhat crudely as done in [20].

Finally, the term $\nu_{R,i}$ in equation 2.13 is the recombination frequency of the i-th positive ion with a possible negative ion.

2.1.3 The electrical quasi-neutrality condition

The last equation to be included in the system of non-linear algebraic equations of the global model is the electrical quasi-neutrality condition

$$\sum_{i=1}^{N-1} q_i\, n_i = 0, \tag{2.17}$$

expressing the macroscopic neutrality of the plasma, where q_i is the electric charge of a particle of the i-th species and n_i is its average density. This condition would be strictly satisfied only if the positively charged sheath regions of the discharge were not included in the global model. However, if the sheath volume is much less than the total chamber volume, as it happens in the rf discharges considered in this chapter, the averaged charge density is so low that assuming the condition 2.17 to be satisfied in the whole chamber volume is a good approximation.

2.1.4 The GMS code

The numerical code GMS, has been created in order to solve the system of equations described at the beginning of this section. Taking as input the list of processes included in the model and the related collision data, GMS constructs the corresponding set of non-linear algebraic equations to be solved. Then it calculates its solution iteratively for the selected values of the external parameters of the discharge by using the Newton-Raphson algorithm [52].

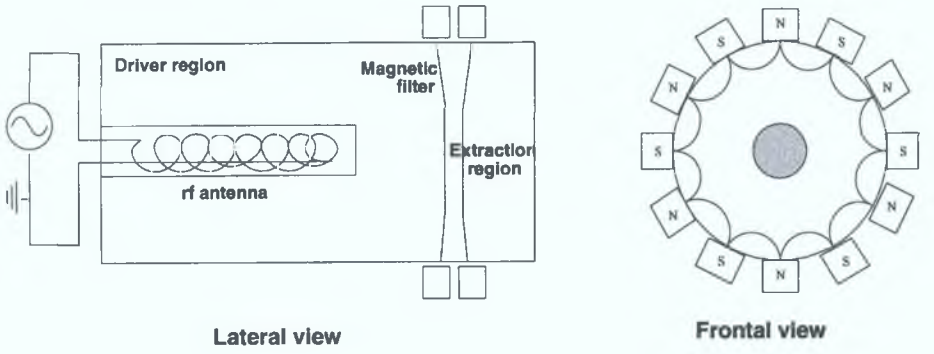

Figure 2.1: DENISE chamber.

2.2 Adapting the model to the DENISE ion source

The DENISE chamber is schematically represented in figure 2.1. It is a cylinder of radius $R = 10$ cm and length $L = 31.2$ cm having on one side a reentrant cavity on the axis of the cylindrical chamber. An antenna is placed in the cavity surrounded by a dielectric of radius $R_c = 2.5$ cm and length $L_c = 20$ cm. In the continuous wave (cw) rf mode of the negative ion source an inductively coupled rf plasma is created with the rf power delivered via the antenna, which is driven by a 3 kW rf power supply, operating at the fixed frequency of 13.56 MHz.

Some of the permanent magnets placed externally to the chamber produce a magnetic filter between the driver and extraction regions, as shown in the lateral view of the chamber in figure 2.1. The magnetic filter prevents energetic electrons, created in the driver region, from entering the extraction region, where they would increase the H^- loss rate and thus its density. As a consequence, the H^- densities in the two regions separated by the magnetic filter are different, but they can be both calculated under certain assumptions. If the volume of the extraction region is much smaller than the volume of the driver region, the inhomogeneity in T_e will not significantly influence the

production and loss rates, and hence also the densities, of all species except H^- Therefore, in order to obtain an estimate of the H^- density, n_{H^-}, in the extraction chamber, the particle balance equation for H^- can be solved with the values of the other species densities obtained from the calculations in the global model, but with a lower value of T_e, to take into account the effect of the magnetic filter The EEDF in the extraction region is always assumed to be Maxwellian

The other permanent magnets placed around the chamber produce a multicusp magnetic field, as shown in the front view of the chamber in figure 2 1 The multicusp magnetic field improves the electron confinement in the radial direction and therefore increases the electron density The presence of both the reentrant cavity for the antenna, and the multicusp magnetic field compel us to modify some of the terms in the equations described in subsection 2 1 2 The addition of the cavity decreases the volume of the chamber and increases its surface area As a consequence, the effective diffusion length Λ, defined as the ratio of volume to surface of the chamber, decreases as well Moreover, the equations 2 15 were calculated for parallel plate and infinite cylinder geometries They could be still assumed approximately valid for a cylindrical chamber of finite size, but the presence of the reentrant cavity in the DENISE chamber complicates the geometry

The addition of the cavity obviously decreases the average distance between the sheaths both in the radial and in the axial directions so its effect on equations 2 15 is to effectively reduce the values of R and L and then increase h_L and h_R Therefore A_{eff}, defined by the expression 2 14, increases as well Since the DENISE chamber geometry is not very simple, it is difficult to get more precise formulae for h_L and h_R, replacing the equations 2 15 Therefore, in our model we modify only the value of Λ with respect to the case of cylin-

drical symmetry, but we do not replace equations 2 15 with any other formula, even though we realize that in this way h_L and h_R are underestimated and so is A_{eff} Consequently, from the power balance equation and the quasi-neutrality condition, the electron density is overestimated

The extra charged particle loss resulting from the presence of the dielectric antenna tube is included by adding its area to equation 2 14 As expected, this results in an increase in T_e and a decrease in n_e However, the changes are of the order of a few percent throughout the entire pressure range investigated

The multicusp confinement is included in the model by using the following alternative definition of the effective area used in the equation 2 13

$$A_{eff} = 2\,\pi\,R\,(a_c\,L\,h_R + R\,h_L) + 2\,\pi\,R_c\,L_c\,h_R, \qquad (2\ 18)$$

where the last term on the r h s is the contribution to the effective area of the cavity lateral surface The value of the quantity a_c depends on the plasma confinement obtained on the external wall of the chamber It is equal to 1 in absence of the multicusp magnetic field and equal to 0 if there is no radial plasma loss at all on the external wall of the chamber, i e if the effective leak width of a line cusp is equal to zero By comparing the results obtained for different values of the parameter a_c, it is possible to carry out a sensitivity study of the effect of the multicusp magnetic field on the discharge A self-consistent model would require both relating the value of a_c to the structure and intensity of the magnetic field and a derivation of an expression for the positive ion density ratio in the various areas of the sheath valid for this asymmetric geometry

2.3 A global model for DENISE without H^-

To validate our model the results obtained were compared with the available experimental measurements of the electron density and temperature [23] The absence of negative ions from the model does not affect significantly the results for the species included in the model, as the inclusion of negative ions would produce a weakly electronegative plasma discharge This can be seen in the results of section 2 4

2.3.1 Collision processes included in the model

The collision processes included in this first model are listed in table 2 2 Previous models [65, 63, 54] of filament driven H_2 discharges were considered for our modelling The cross section data for the processes included in the model are the most reliable and up to date found in the literature Rate constants of the electron collision processes are obtained from the cross section data, given both the shape of the EEDF, assumed to be Maxwellian, and the value of the electron temperature When the inverse collision processes were included, their cross sections were calculated from the direct processes cross section data by using the principle of detailed balance [11, p 248]

Examining the collision processes listed in table 2 2, it can be seen that H_3^+ particles can be created only by the interchange reaction $H_2^+ + H_2 \rightarrow H_3^+ + H$, not by any electron collision process Thus, only for H_3^+, the formula 2 11 for the collisional energy loss per electron-ion pair created does not make sense Therefore, we have to assume that $\mathcal{E}_{L,H_3^+} = \mathcal{E}_{L,H_2^+}$, as H_3^+ particles can originate only from an H_2^+ loss collision process H_3^+ loss by dissociative recombination happens not only by the channel $e + H_3^+ \rightarrow H_2 + H$, listed in table 2 3 1, but also by the other channel $e + H_3^+ \rightarrow e + H^+ + H + H$ Since we could not find

Table 2.2: Collision processes used for modelling the discharge without H^-.

Process	Data references and/or rate constant formula
$e + H_2 \longrightarrow e + e + H_2^+$;	[53]
$e + H_2(v) \longrightarrow e + e + H_2^+$; (v=1-2)	[54]
$e + H_2 \longrightarrow e + H_2^*(b\,^3\Sigma_u^+) \longrightarrow e + H + H$;	[55, 56]
$e + H_2 \longrightarrow e + H_2(v)$ and inverse; (v=1-2)	[57, 58]
$e + H_2(v=1) \longrightarrow e + H_2(v=2)$ and inverse	[59]
$e + H_2 \longrightarrow e + H_2^* \longrightarrow e + H_2(v) + h\nu$; (v=1-2)	[60]
$e + H_2 \longrightarrow e + e + H^+ + H$;	[61]
$e + H \longrightarrow e + e + H^+$	[57]
$e + H_2^+ \longrightarrow e + H^+ + H$	[57]
$H_2^+ + H_2 \longrightarrow H_3^+ + H$	[62]
$e + H_3^+ \longrightarrow H_2 + H$	[57]
$e + H_3^+ \longrightarrow e + H^+ + H + H$	[57]
$e + H_2 \longrightarrow e + H + H^*(2s)$	[61]
$e + H \longrightarrow e + H^*(2s)$	[61]
$e + H^*(2s) \longrightarrow e + e + H^+$	[61]
$H + H_2(v') \longrightarrow H + H_2(v'')$; (v'=1-2, v'' < v')	[63]
$H + H_2(v') \longrightarrow H_2(v'') + H$; (v'=1-2, v'' < v')	[63]
$H \stackrel{(wall)}{\longrightarrow} \frac{1}{2}H_2$	$\gamma_{rec} D_{eff}/\Lambda^2$
$H^+ \stackrel{(wall)}{\longrightarrow} H$	$u_{B,H^+} A_{eff}/V$
$H_2^+ \stackrel{(wall)}{\longrightarrow} H_2$	$u_{B,H_2^+} A_{eff}/V$
$H_3^+ \stackrel{(wall)}{\longrightarrow} H + H_2$	$u_{B,H_3^+} A_{eff}/V$
$H^*(2s) \stackrel{(wall)}{\longrightarrow} H$	D_{eff}/Λ^2
$H_2(v') \stackrel{(wall)}{\longrightarrow} H_2(v'')$; (v'=1-2, v'' < v')	$w_{v',v''} D_{eff}/\Lambda^2$; [64]

any cross section data for each of these two channels, we assumed the dissociative recombination total cross section data is connected only to the former channel. The first channel is the most likely one for H_3^+ loss at the values of the electron temperature we obtained. These are always greater than 2 eV (see figure 2.2) [61]. Both channels are important for H_3^+ loss, but this is not the case for H or H_2 production. Therefore including in the model only the channel $e + H_3^+ \rightarrow H_2 + H$ instead of both for dissociative recombination is a very good approximation.

For $H_2(v)$ de-excitation by collisions with H, both the non-reactive and the reactive processes are included in the model. For the relevant constants to be set in the global model, in the absence of experimental measurements of ion and neutral temperatures at this stage of the investigation, the ion, atomic neutral and molecular neutral temperatures are all assumed equal to 0.05 eV. The recombination coefficient γ_{rec} of atomic hydrogen H at the wall is assumed to be equal to 0.1, a typical value for a stainless steel wall [63]. In DENISE the gas exits freely through an orifice of area $A_{or} = 50.26$ mm^2.

2.3.2 Results and discussion

In figures 2.2-2.3 the values of the electron temperature T_e and the electron density n_e obtained by using GMS for two different values of the input power P are plotted versus the pressure p, defined as the sum of the partial pressures of the neutral species. These data are compared with the experimental measurements performed by Deirdre Boilson with a Scientific Systems Langmuir probe 2 cm away from the antenna tube.

T_e is determined by the particle balance equations of the positive ions included in the model [11, p. 306]. As expected, T_e decreases with increasing p at fixed P, and this decrease is clearly apparent in figure 2.2. Moreover, the

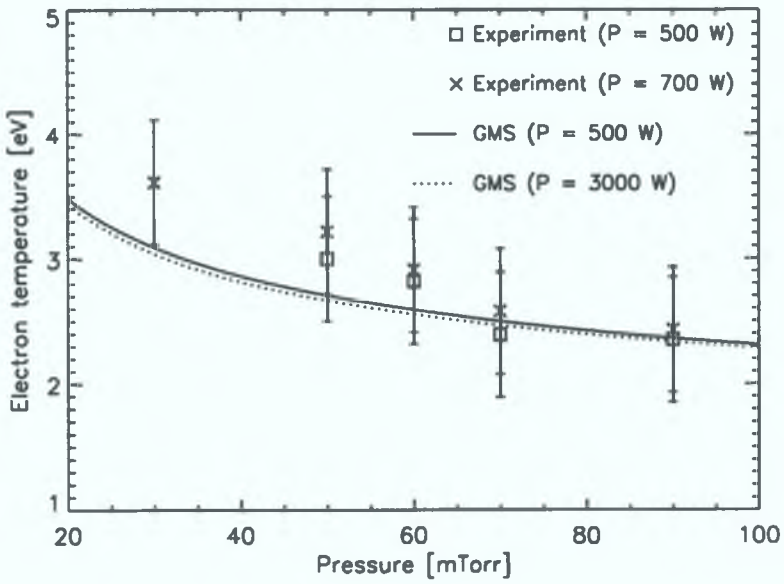

Figure 2.2: Electron temperature vs. pressure without multicusp magnetic field.

numerical data show that T_e decreases very little with increasing P at fixed p. The error bars shown on the experimental points in figure 2.2 are a conservative estimate of the actual uncertainty due to both the reproducibility of successive measurements and the differences in T_e resulting from choosing different methods of analysing the probe traces. There is good agreement between the results of our model and the experimental measurements, although at 30 mTorr, the measured T_e is somewhat higher than the value calculated by the global model. A contributing factor in this is likely to be the rf modulation of the plasma potential. The probe contains filter elements to reduce interference from rf modulation of the sheath around the tip, but residual rf voltage across this sheath can cause a slight apparent increase in T_e. This is consistent with the values taken at 700 W, being higher than the ones taken at 500 W, in contradiction to the GMS results. However, the actual errors in the probe data are too large for a definite conclusion to be reached on this point.

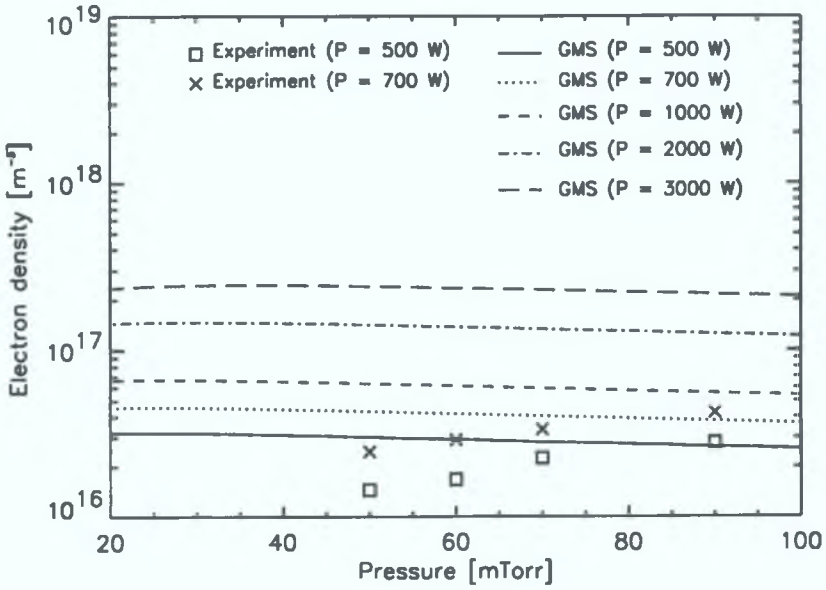

Figure 2.3: Electron density vs. pressure without multicusp magnetic field.

Since the sheath voltage in the global model is calculated from the equation 2.9, assuming inductive coupling to the plasma, only experimental data at pressures above the threshold of the transition from the capacitively coupled mode to the inductively coupled mode are considered. For the capacitive coupling regime of the discharge, the sheath voltage should be calculated in a different way, assuming a suitable model for the rf sheath dynamics, for example see [22]. Capacitive coupling will be present in the inductive mode, as no Faraday shield was used in the experiments to surround the antenna. Low pressure measurements with a Faraday shield in place were attempted on another experiment with the same antenna configuration, but ignition problems led to arcing and component damage. The lack of shielding is an important factor in producing differences between the experimental and the numerical results for the electron density. This is due to the fact that as the pressure is lowered, the antenna voltage increases and the effect of the capacitive coupling

becomes more significant The main consequence is that more power is used in accelerating the ions through the sheaths and for pressures below 80 mTorr the measured electron density is less than that predicted by the global model

The measured values of n_e are presented in figure 2 3 without error bars because the main cause of discrepancy between such values and the global model results is due to the effect of the capacitive coupling not included in the global model, and not due to the uncertainty of the measurement technique or reproducibility (uncertainties of approximately 20%) We believe that this is also the reason for the different pressure dependencies of n_e seen in the experiment and in the model, but, as expected, n_e increases with increasing P at fixed p, approximately in the same way in both the experiment and the model

The calculated n_e decreases slightly with increasing p at fixed P This is due to how the quantities A_{eff}, $u_{B,i}$ and $\mathcal{E}_{T,i}$, all being part of equation 2 13, vary with increasing p A_{eff} decreases with increasing p, as can be deduced by examining equations 2 14-2 16, because the total neutral density n_{neu}, by definition, increases and the volume occupied by the gas is constant T_e decreases and so does $u_{B,i}$, with increasing pressure For all positive ion species included in the model, $\mathcal{E}_{T,i}$ increases with increasing p, because T_e decreases The second and third terms in the square brackets in the expression 2 11, associated respectively with the inelastic and the elastic collision processes, increase with decreasing T_e (increasing p), because the positive ion production process rate constant decreases more rapidly than the rate constant of any of its associated inelastic and elastic collision processes That is true because T_e is always much lower than the threshold energies of the production processes of H^+ and H_2^+ Therefore, $\mathcal{E}_{L,i}$ increases with increasing p and so does $\mathcal{E}_{T,i}$, defined in 2 7, because the decrease of $\mathcal{E}_{i,w} + \mathcal{E}_{e,w}$ with decreasing T_e (increasing p) is slower

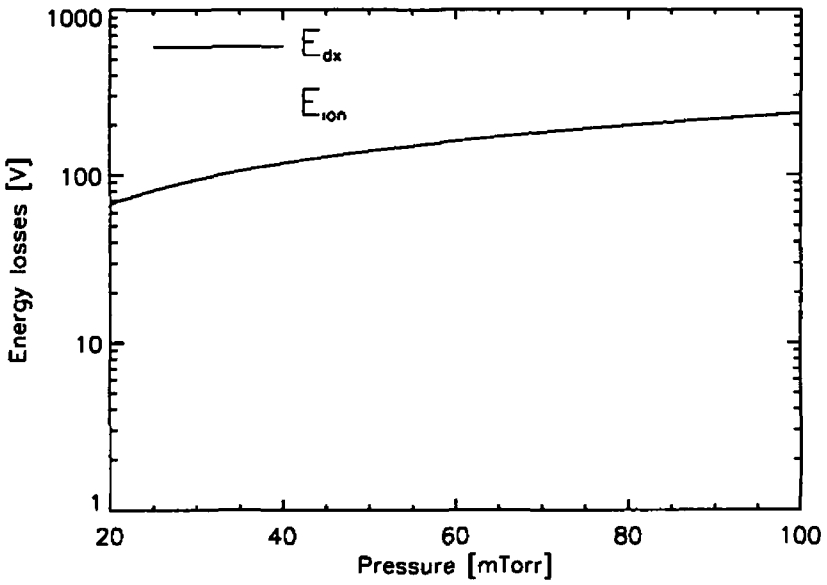

Figure 2 4 Contributions of the H_2 dissociation and ionisation processes to the collisional energy loss per electron-H_2^+ ion pair created vs pressure

than the increase of $\mathcal{E}_{L,i}$ with decreasing T_e

Let us take H_2^+ as an example E_{dx}, the contribution of the electron dissociation process of H_2 to $\mathcal{E}_{L,H_2^+}$, the collisional energy loss per electron-H_2^+ ion pair created, is plotted in figure 2 4 as a function of p, along with $E_{ion} = \mathcal{E}^{pr}_{H_2^+ H_2}$, the contribution of the H_2 ionisation process to $\mathcal{E}_{L,H_2^+}$ As expected, E_{dx} increases with increasing p (decreasing T_e) and is always much bigger than E_{ion}, which is a few tenths of an eV less than 15 4 eV, the threshold energy of the H_2 electron ionisation process If some vibrationally excited states of H_2 were not considered in the model along with their ionisation processes, then the only collision process producing H_2^+ would be electron ionisation of H_2 In that case its contribution $\mathcal{E}^{pr}_{H_2^+ H_2}$ would be exactly equal to the threshold energy of the H_2 electron ionisation process, following the definition 2 11 of $\mathcal{E}_{L,H_2^+}$ Therefore for all positive ions considered in the model $\mathcal{E}_{T,i}$ increases with increasing p

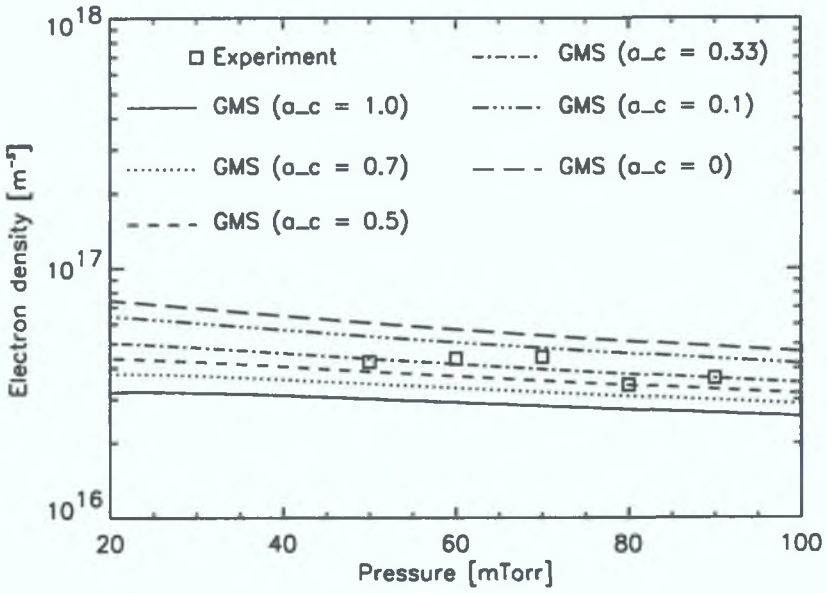

Figure 2.5: Electron density vs. pressure with multicusp magnetic field; $P = 500$ W.

to such an extent that the electron density (which is equal to the sum of all the positive ion densities) must decrease with increasing p to satisfy the power balance equation.

When the multicusp magnetic field is used, the experimental values of n_e fit much better the numerical results of the global model than when the magnetic field is off, as can be seen in figure 2.5. The main reason for this is likely to be the increase in the electron density after the activation of the multicusp magnetic field and the consequent decrease in capacitive coupling. As explained in section 2.2, the effect of the multicusp magnetic field on the discharge is taken into account by the constant a_c in the equation 2.18. Its value is equal to the fraction of the remaining plasma radial loss on the external lateral wall of the chamber after the activation of the multicusp magnetic field. Values for n_e were calculated for several values of a_c between 1 (magnetic field not activated) and 0 (complete radial plasma confinement on the external

lateral wall of the chamber) and the results are compared with the experimental values in figure 2 5 For $a_c = 0\ 33$ the numerical results fit reasonably well the experimental data

In spite of the intrinsic limitations of a global model and of all the simplifying assumptions that had to be made so that this kind of analysis could be carried out, the results presented in this section show that a good agreement has been found between the global model results and the experimental measurements performed in DENISE The model can be made more complex by including more particle species and collision processes In the next section that will be done in order to study the H^- kinetics and the effect of the activation of the magnetic filter on the H^- density in the extraction region

2.4 A global model for DENISE with H^-

Validation of our global model was obtained in section 2 3 by comparing some of its results with the available experimental data for DENISE In this section a more complex model of the plasma discharge is used to study the H^- kinetics and to calculate the H^- density in the extraction chamber [24] under certain assumptions when the magnetic filter is used The causes of the differences between our results and those obtained by using other models of plasma discharges in other negative ion sources are also discussed [24]

2.4.1 Collision processes included in the model

The collision processes added to those of table 2 2 to model the H^- kinetics are listed in table 2 3 The inclusion of H^- in the model compels us to include further vibrationally excited states of H_2, as their electron Dissociative Attachment (DA) is thought to be the most effective known H^- production

Table 2 3 Collision processes added for modelling the discharge with H^-

Process	Reference and/or rate constant formula
$e + H_2(v) \longrightarrow e + e + H_2^+$, (v=3-4)	[54]
$e + H_2 \longrightarrow e + H_2(v)$ and inverse, (v=3-6)	[57, 58, 68]
$e + H_2(v) \longrightarrow e + H_2(v+1)$ and inverse, (v=2-8)	[59]
$e + H_2(v) \longrightarrow H + H^-$, (v=0-9)	[69, 70]
$e + H_2 \longrightarrow e + H_2^* \longrightarrow e + H_2(v) + h\nu$, (v=3-9)	[60]
$e + H_3^+ \longrightarrow H_2^+ + H^-$	[57]
$e + H^- \longrightarrow e + e + H$	[61]
$H + H^- \longrightarrow e + H_2$	[61]
$H^+ + H^- \longrightarrow H + H$	[62]
$H_2^+ + H^- \longrightarrow H_2 + H$	[71]
$H_3^+ + H^- \longrightarrow H_2 + H + H$	[71]
$H + H_2(v') \longrightarrow H + H_2(v'')$, (v'=3-9, v'' < v')	[63]
$H + H_2(v') \longrightarrow H_2(v'') + H$, (v'=3-9, v'' < v')	[63]
$H_2(v') \overset{(wall)}{\longrightarrow} H_2(v'')$, (v'=3-9, v'' < v')	$k = w_{v',v''} D_{eff}/\Lambda^2$, [64]

mechanism and the rate constant of the process dramatically increases with the vibrational level v of H_2 The available literature data allow us to consider only the H_2 vibrational levels up to $v = 9$ It was proposed and debated also that DA of H_2 Rydberg states might be an effective mechanism in H^- production [66, 67], but there is no general agreement on this point, and this mechanism is not included

For including certain collision processes in the model some approximations had to be made The cross section data of $e + H_2(v) \rightarrow e + H_2(v+1)$ were available only for $0 \leq v \leq 3$, so for $v > 3$ we used the same cross section data

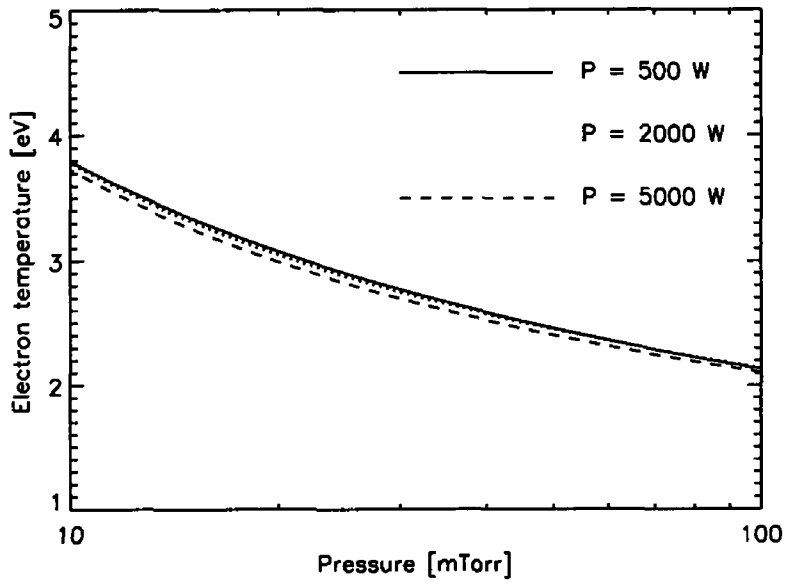

Figure 2 6 Electron temperature vs pressure

as for v = 3, even though the rate constant of these processes were underestimated in this way, as the energy difference between the two vibrational levels becomes smaller as v increases Moreover, no cross section data for $H_3^+ + H^- \rightarrow H_2 + H + H$ were available, so the same theoretical data calculated for $H_2^+ + H^- \rightarrow H + H_2$ had to be assumed for this collision process The values of all the quantities assumed constant in the model are the same as in section 2 3 and the constant a_c is set equal to 0 33

2.4.2 Effect of pressure variation on results

The electron temperature T_e is mainly determined by the particle balance equations of the positive ions included in the model [11, p 306] and, as shown in figure 2 6, it decreases with increasing pressure p at fixed power Moreover, it does not change significantly if the power changes and p is constant

In figure 2 7 it can be seen that H_2 is the dominant neutral species through-

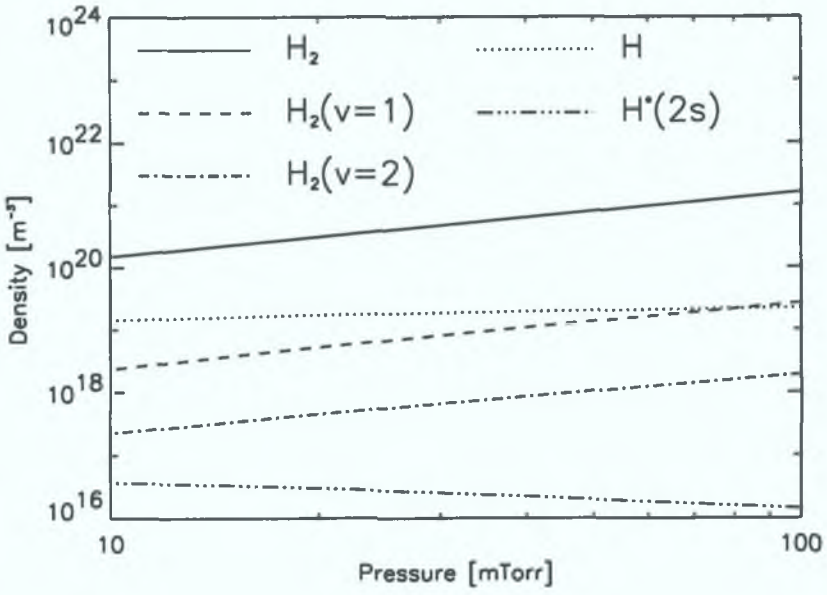

Figure 2.7: H_2(v=0-2), H and H*(2s) density vs. pressure; $P = 500$ W.

out the pressure range examined, so the practically linear increase of n_{H_2} with pressure, defined as the sum of the partial pressures of all the neutral species included in the model, is what expected. At 10 mTorr, n_H is approximately 10% of the total neutral density, but at higher pressures this percentage decreases, as n_H increases more slowly than n_{H_2}. The rate constants of the processes where H particles are mainly produced (electron dissociation of H_2), and lost (H neutral recombination), decrease with increasing pressure. The density of the metastable species H*(2s) in the pressure range considered is of the order of $10^{16}\,m^{-3}$. H*(2s) is produced by H excitation and H_2 dissociative excitation and mainly lost by wall de-excitation. The vibrationally excited species $H_2(v = 1, 2)$ have a lower density than H_2 by at least two orders of magnitude. They are mainly produced by H_2 direct electron excitation and lost by H_2(v) wall de-excitation.

The densities of all the vibrationally excited states of H_2 included in the

model decrease as the vibrational level v increases, for a fixed value of pressure, as can be seen in figure 2 8 The main production mechanism of $H_2(v)$ at pressures around 100 mTorr (if included in the model for the considered value of v) is the electron excitation from a lower vibrational state, the so-called e-V process At pressures around 10 mTorr the main production mechanism for $H_2(v \geq 3)$ is the two-step collision process composed by electronic excitation and radiative cascade over the H_2 ground-state vibrational levels $e + H_2 \rightarrow H_2^* \rightarrow e + H_2(v') + h\nu$ This is called the E-V process, because this kind of vibrational excitation process necessarily involves an energetic electron, in contrast to the e-V process According to the experimental measurements, the electron temperature is approximately equal to 2 eV at 100 mTorr, and since the EEDF is Maxwellian, primarily the cold electrons produce vibrational excitation In contrast, at pressures around 10 mTorr, the E-V process is effective in producing vibrational excitation, because the electron temperature should be approximately equal to 4 eV At a fixed value of pressure, the importance of the E-V mechanism in the production of $H_2(v)$ increases with the vibrational level v Actually, the E-V process is the only production mechanism of $H_2(v=7-9)$ from H_2 included m the model, as we could not find in the literature any cross section data for the e-V process producing $H_2(v=7-9)$ from H_2

The $H_2(v)$ de-excitation processes considered in the model are the aforementioned wall de-excitation, generally the main de-excitation mechanism, V-T de-excitation by collisions with H, becoming more effective with increasing power, and finally electron de-excitation The de-excitation probabilities $w_{i,j}$ used for the wall de-excitation processes are those calculated by Hyskes and Karo [64] For the V-T processes we used the rate constants calculated by Gorse et al [63] and the rate constants of the electron de-excitation processes

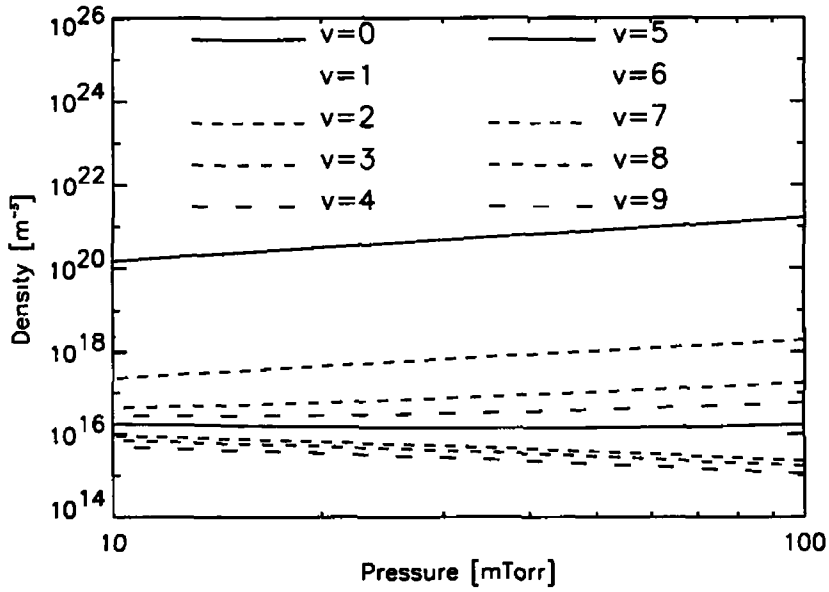

Figure 2 8 H_2(v=0-9) density vs pressure, $P = 500$ W With an increase in the value of v the H_2(v) density decreases

were calculated from the cross section data of the inverse electron excitation processes by using the detailed balance principle Considering the importance of the e-V process in the production of H_2(v=6) from H_2, we deduce that the e-V processes producing H_2(v=7–9), which we could not include in the model, would give an important contribution to H_2(v=7–9) production rates as well Therefore their calculated densities would be increased The gap between the densities of the H_2(v = 6) and H_2(v = 7), which becomes larger with increasing pressure, can be partially explained by the absence from the model of the e-V processes producing H_2(v=7–9) Therefore the calculated H_2(v=7–9) densities are underestimated at the highest considered values of the pressure in this model

H_3^+ is the dominant positive ion species in the pressure range considered at a power of 500 W, as can be seen in figure 2 9 H_3^+ particles are produced

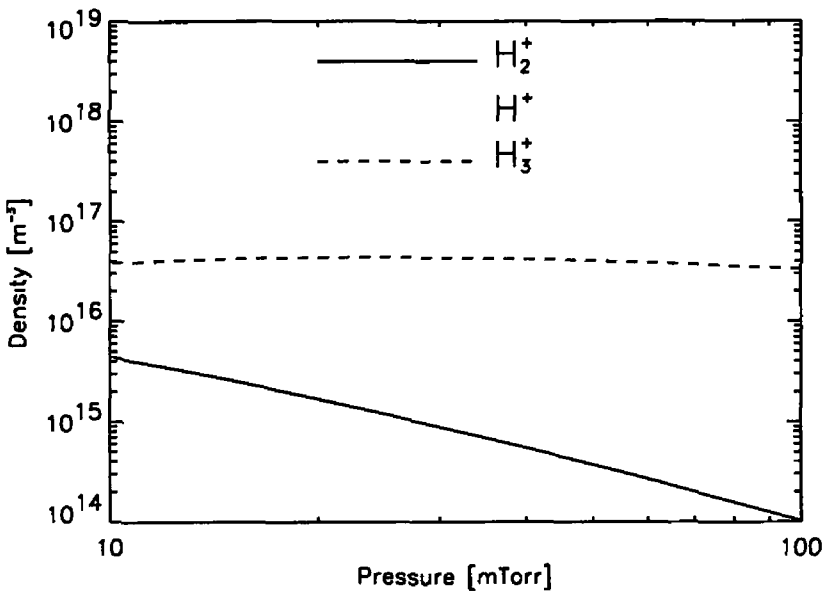

Figure 2 9 Positive ion densities vs pressure, $P = 500$ W

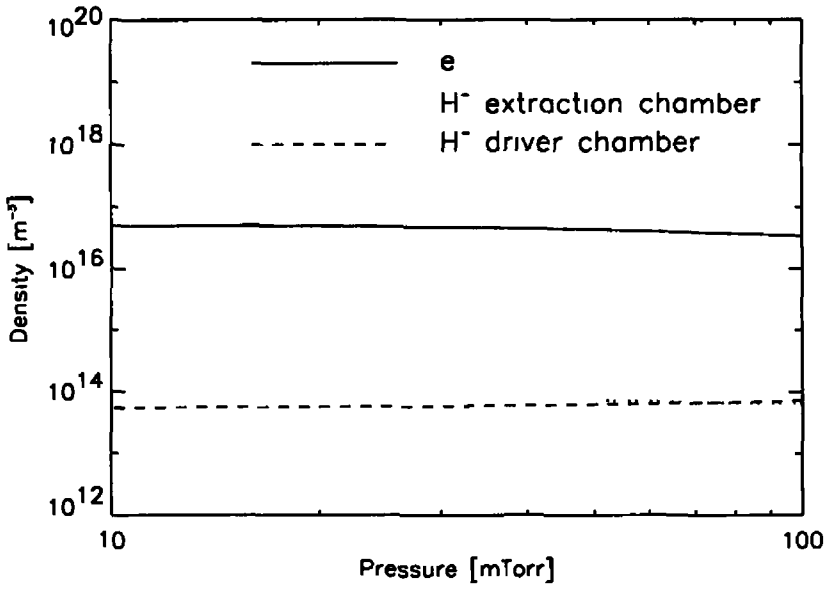

Figure 2 10 n_e and n_{H^-} vs pressure, ($P = 500$ W)

by the interchange reaction (IR) $H_2^+ + H_2 \longrightarrow H_3^+ + H$, while H_2^+ particles are produced by H_2 electron ionisation. The H_2^+ conversion into H_3^+ becomes more effective as the pressure increases, because the H_2^+ ionisation rate constant k_{iz} decreases with decreasing T_e (increasing pressure), while k_{ir}, the rate constant of IR, the dominant H_2^+ destruction process, is assumed to remain constant if the pressure changes. So the approximate H_2^+ rate equation at higher pressures

$$n_e\, n_{H_2}\, k_{iz} = n_{H_2^+}\, n_{H_2}\, k_{ir} \tag{2.19}$$

requires that $n_{H_2^+}$ decreases with increasing pressure, while the value of the r.h.s. of the equation 2.19, being equal to the H_3^+ production rate, increases and so does $n_{H_3^+}$. H^+ is mainly produced by electron ionisation of H and $H^*(2s)$. At a power of 500 W the H^+ density decreases with increasing pressure, since the rate constants of all its production mechanisms decrease with T_e. At the same time the rate constant of the main H^+ loss process, H^+ wall neutralisation, does not decrease to the same extent with increasing pressure.

The H^- density, n_{H^-}, is always far less than 10% of n_e, as can be seen in figure 2.10. The sheath is not significantly affected by the electronegativity for the values of α (the negative ion to electron density ratio) and γ (the negative ion to electron temperature ratio) considered here. This can be seen from the analytical solution shown in figure 6.4 in [11, p. 169]. Therefore, the formulae 2.15 calculated by Godyak [50] for an electropositive plasma, can still be considered valid for the weakly electronegative plasma resulting from our model. The inclusion of H^- in the model does not significantly change the averaged densities of all the other particle species. That would still be true even if the calculated H^- density was of the order of 10 % of the electron density. The electron density n_e is of the order of $10^{16}\,m^{-3}$ in the pressure range considered, and is approximately equal to the total positive ion density. Above 13 mTorr, n_e decreases with increasing pressure, because of the

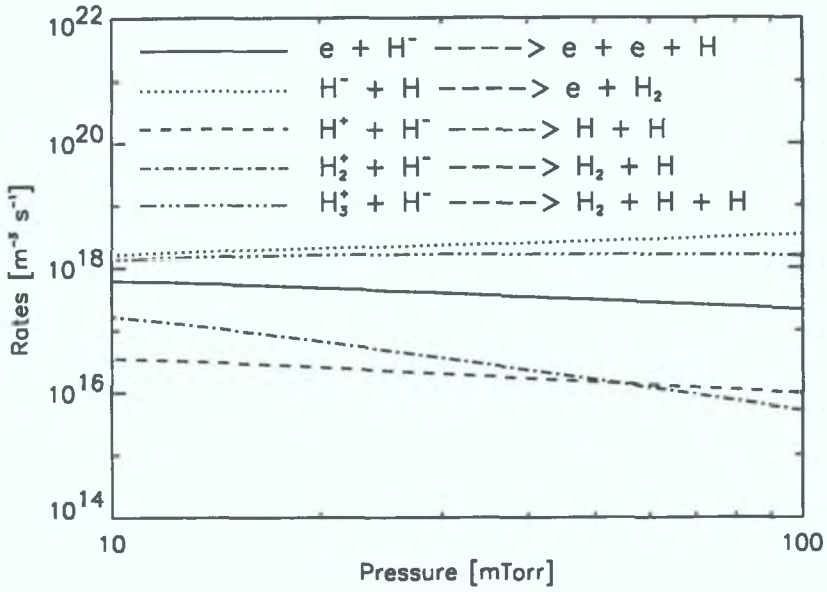

Figure 2.11: H^- loss rates vs. pressure; $P = 500$ W, driver chamber.

increasing contribution of the H_2 dissociation process to $\mathcal{E}_{L,H_2^+}$ in the power balance equation.

As already explained in section 2.2, in the driver chamber the densities of all species included in the model and T_e are all calculated by GMS by solving the corresponding set of equations. To calculate n_{H^-} in the extraction chamber only the H^- particle balance equation is solved by setting the values of all other densities equal to the values calculated for the driver region and the electron temperature to 1 eV. This is near the optimum value for H^- production, as the cross section data of the dissociative attachment of the considered high vibrationally excited states of H_2 are peaked around this value of the energy. The increasing difference between the temperatures in the two regions, with decreasing pressure, widens the gap between the values of n_{H^-} calculated for the two regions.

In figure 2.11 the H^- loss rates of the electron detachment, associative de-

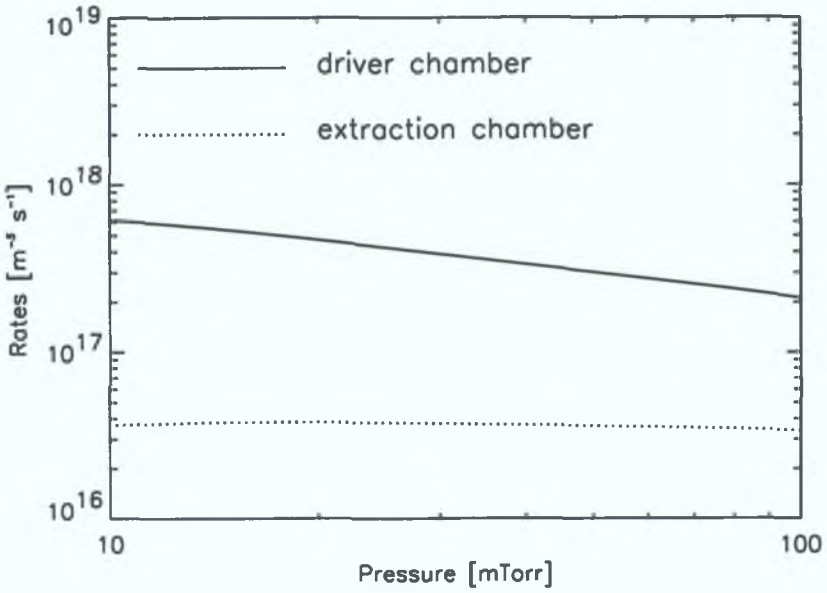

Figure 2.12: H^- loss rates of electron detachment vs. pressure; $P = 500$ W.

tachment and mutual neutralisation processes, are plotted as a function of the pressure at $P = 500$ W. No cross section data for the H_3^+ mutual neutralisation were found in the literature, so the data used for H_2^+ mutual neutralisation [71] were used also for H_3^+ mutual neutralisation. The rate of the electron detachment process $e + H^- \longrightarrow e + e + H$, an effective H^- loss process in the driver chamber, especially at the lowest considered values of the pressure, is much lower in the extraction chamber than in the driver chamber, as can be seen in figure 2.12. The difference in the H^- loss rates of this process is caused by the different values of T_e in the two regions.

At the lowest considered values of the pressure dissociative attachment of the ground-state and the first excited vibrational levels of H_2 give the smallest contributions to the H^- production rate, as can be seen in figure 2.13. This is despite those species having significantly higher densities than $H_2(v > 2)$. The dramatic increase of the DA rate constant with increasing vibrational level v

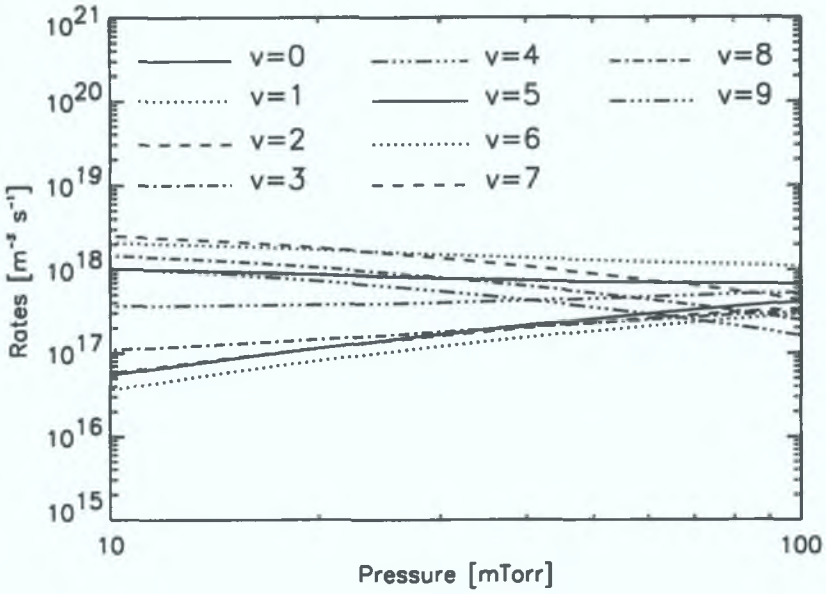

Figure 2.13: H^- production rates vs. pressure; $P = 500$ W, extraction chamber.

causes the highest H^- production rate to occur at levels v $= 6, 7$ throughout the pressure range considered here. The H^- production rate of the vibrationally excited states of lowest level of H_2 through DA process is important only at the highest pressures considered, because the density of the higher vibrational levels of H_2 does not increase with increasing pressure as much (or even decreases) as the density of the lower levels. Over a large pressure range the H^- production rates associated with $H_2(v > 4)$ are all approximately of the same order of magnitude and are much higher than the rates associated to the lower vibrationally excited states. The previously discussed underestimation of the $H_2(v = 7, 9)$ densities present in our model underestimates also their contribution to H^- production by DA, and therefore the resulting n_{H^-} at the highest considered values of the pressure.

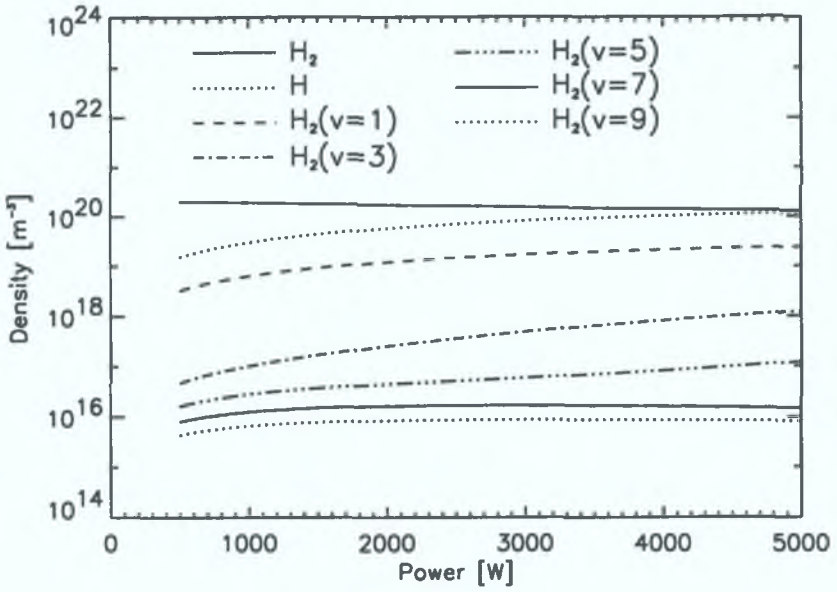

Figure 2.14: Neutral densities vs. power; S_{in} = constant.

2.4.3 Effect of input power variation on results

In figures 2.14-2.16 the densities of many species included in the model are plotted as a function of the input power. Although the inlet flow rate S_{in} is kept constant, the pressure increases slightly, from 13 to 16 mTorr, with increasing power, because the H_2 fractional dissociation increases as well.

In figure 2.14 it can be seen that n_H is almost equal to n_{H_2} at a power of 5000 W. The densities of $H_2(0 < v \leq 6)$ also increase significantly with increasing power. An increase in the value of the input power obviously modifies only the power balance equation making the total positive ion density increase (as can be deduced from figure 2.15) and subsequently also the electron density, but does not appear to increase the densities of $H_2(v=7-9)$ beyond a certain level of power, as can be seen in figure 2.14. However, if the densities of those species were plotted at fixed pressure (and not at a fixed S_{in} and consequently at increasing pressure), then they would increase with increasing power. At

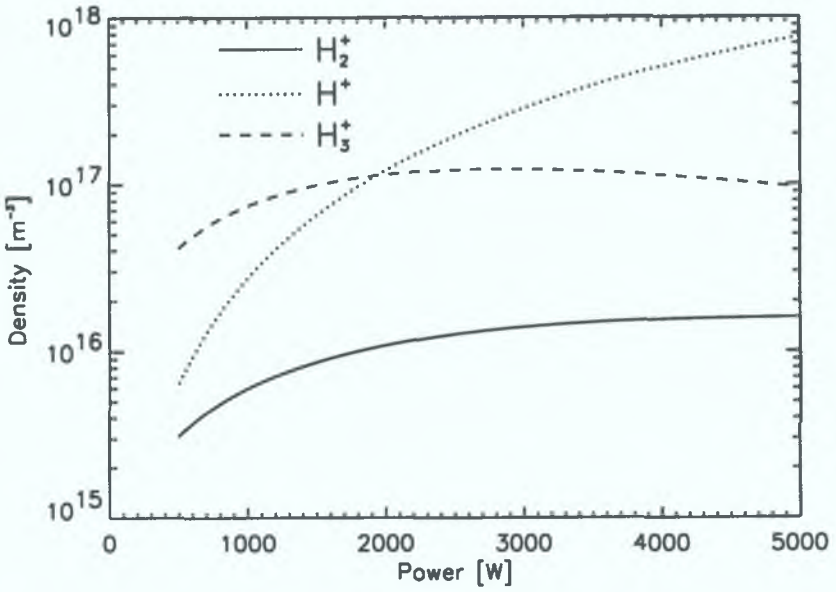

Figure 2.15: Positive ion densities vs. power; S_{in} = constant.

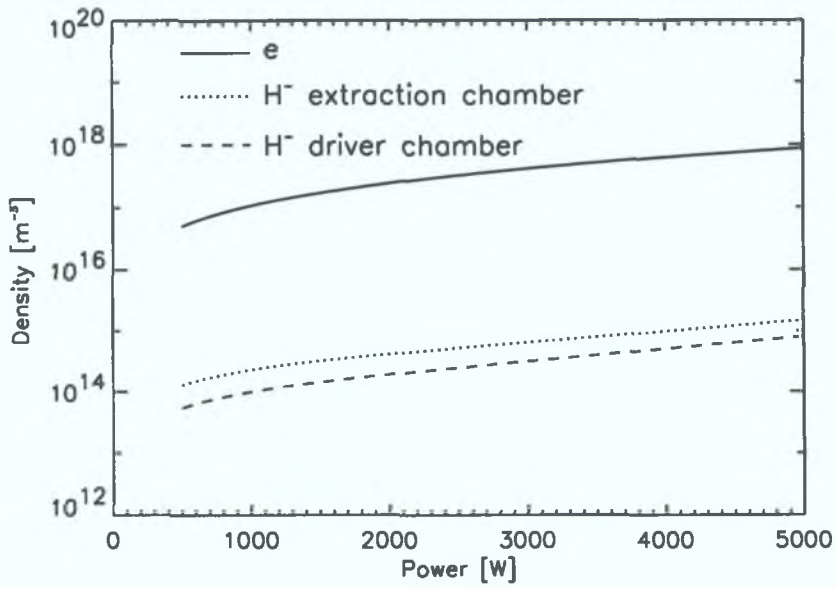

Figure 2.16: n_e and n_{H^-} vs. power; S_{in} = constant.

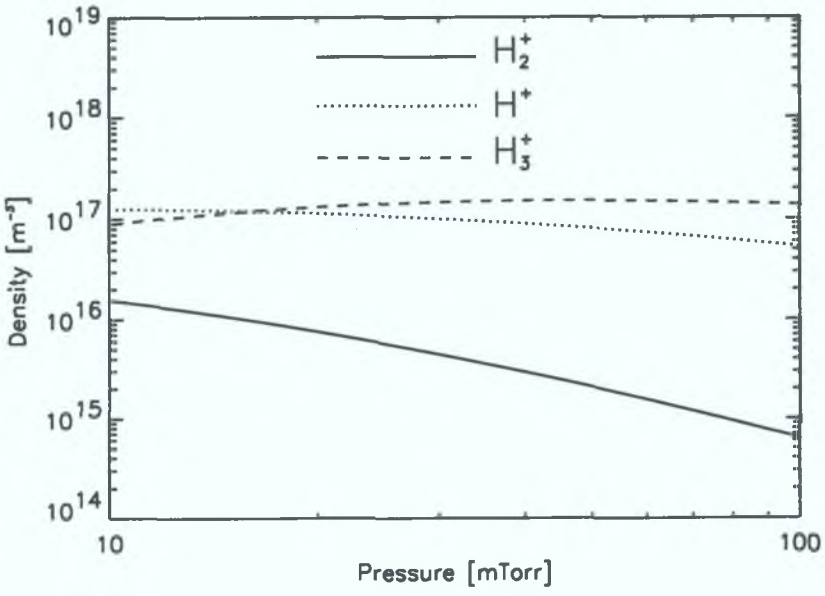

Figure 2.17: Positive ion densities vs. pressure; $P = 2000$ W.

the highest values of power, the high dissociation level reached in the discharge makes H^+ become the dominant positive ion species, as can be seen in figure 2.15. For all values of power $n_{H^-}/n_e \sim 10^{-3}$ in both the driver and the extraction chamber, as seen in figure 2.16. For a better understanding of the effects of increasing the input power, the plots of the charged species densities as a function of pressure at a power of 2000 W are shown in figures 2.17-2.18. They can then be compared with the corresponding plots at 500 W shown in figures 2.9-2.10. It can be seen that the H^+ density is higher than the H_3^+ density at around 10 mTorr and is of the same order of magnitude as the H_3^+ density in the whole pressure range. The higher the power, the higher the H^+ fraction of the positive ion density.

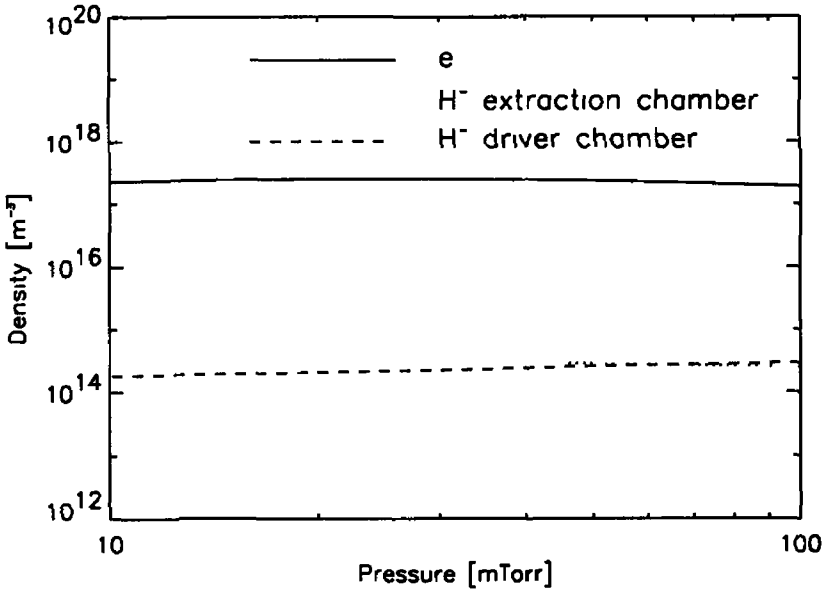

Figure 2 18 n_e and n_{H^-} vs pressure, $P = 2000$ W

2.4.4 Comparison of H^- results with other work

In figure 2 18 it can be seen that $n_{H^-} \simeq 5\,0 \times 10^{14}$ m^{-3} in the extraction chamber for a power of 2000 W and a pressure of 10 mTorr By further decreasing the pressure, the calculated n_{H^-} in the extraction chamber would increase, but its maximum value would be less than 10^{15} m^{-3} This value is at least one order of magnitude lower than the values detected experimentally and calculated numerically by other groups [65, 72, 73] for hydrogen discharges produced by negative ion sources operating in filament driven mode The same difference is observed between the corresponding values of the ratio n_{H^-}/n_e as well An important factor in the differences between our results and those obtained by other groups is the different cross section data used for some of the collision processes included in our model

Some differences are due to the fact that the present model assumes a Maxwellian EEDF, appropriate for rf inductive plasmas, whereas filament

driven sources have typically bi-Maxwellian distributions in the driver region. In order to check the importance of this, global model calculations were performed by assuming a bi-Maxwellian EEDF with both the temperature ratio of the 'hot' and 'cold' components as well as their density ratio as parameters. The resulting changes can not explain the very different values of n_{H^-} obtained.

Of greatest consequence are the rates for H_2 dissociation and ionisation, and for mutual neutralisation between negative and positive ions. With the cross section data used in GMS calculations, k_{ds}, the H_2 dissociation rate constant, is greater than k_{iz}, the H_2 ionisation rate constant for all relevant values of the electron temperature T_e, while the opposite is true for example in [65]. Moreover, for $T_e \geq 3$ eV we have $k_{ds} \geq 10^{-15}\,\mathrm{m^3\,s^{-1}}$, which is almost one order of magnitude higher than $k_{ds} \simeq 3.0 \times 10^{-16}\,\mathrm{m^3\,s^{-1}}$, the value reported in [65] without the corresponding value of T_e. Therefore, higher values of n_H are obtained by using the cross section data employed in GMS calculations, than by using the data used in [65] for the same values of the control parameters and conversely lower values of n_{H^-} should be obtained, since the associative detachment process is the most effective in H^- loss, according to our results. In [65] the same rate constant value, $k_{mn} = 5.0 \times 10^{-14}\,\mathrm{m^3\,s^{-1}}$, was used for the different mutual neutralisation processes of H^- with H^+, H_2^+ and H_3^+, while the 3 rate constants k_{H^+}, $k_{H_2^+}$ and $k_{H_3^+}$, employed in the GMS calculations, that are obtained from theoretical cross section data [71], are all higher than k_{mn}. Consequently, the different values of the mutual neutralisation rate constants used are a factor in making the value of n_{H^-} obtained in our modelling significantly less than those obtained in [65, 72, 73].

In figure 2.19 the values of n_{H^-} in the extraction chamber, calculated under different assumptions for the mutual neutralisation rate constants and with

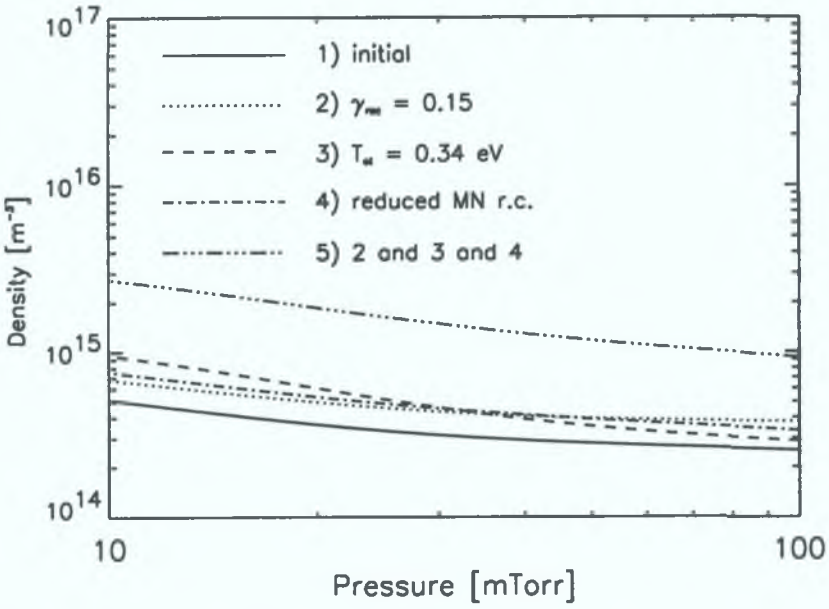

Figure 2.19: n_{H^-} (extraction chamber) vs. pressure; $P = 2000$ W.

different values of certain constants used in the global model, are plotted as a function of the pressure at the power of 2000 W. The first curve, labelled 'initial', is the same as displayed in figure 2.18. The second curve shows n_{H^-} calculated under the same hypotheses, except that γ_{rec} is assumed to be equal to 0.15. That makes n_H, and consequently also the H^- loss rate due to the associative detachment reaction, decrease, therefore, a higher n_{H^-} is obtained. The value of γ_{rec} depends on many factors, including the previous interaction of the plasma with the wall, so γ_{rec} can be quite different from 0.1.

Experimental measurements in H_2 discharges operating in filament driven mode [74] indicate that the temperature of the atomic neutral species, T_{at}, can be about one order of magnitude higher than the value we assumed, 0.05 eV. The third curve represents n_{H^-} obtained assuming $T_{at} = 0.34$ eV. That sets higher values for the H temperature value, the H thermal velocity and consequently the neutral recombination rate constant, which makes n_H decrease.

Therefore n_{H^-} increase, with respect to the values of the first curve. Another effect of the higher H temperature is a higher value of the pressure corresponding to the chosen value of the inlet flow rate, due to the higher contribution of the H partial pressure to the total pressure.

The fourth curve labelled 'reduced MN r.c.' represents the negative ion density obtained by assuming the same mutual neutralisation rate constant for H_2^+ and H_3^+ as for H^+, as done in the other papers [65]. Also, in this case, n_{H^-} is higher than the density values of the first curve, but not to such an extent as to explain the difference in n_{H^-} between the results calculated by using GMS and those obtained in the other works. Even by setting at the same time $\gamma_{rec} = 0.15$, $T_{at} = 0.34$ eV, and reduced values for the H_2^+ and H_3^+ mutual neutralisation rate constants, the maximum value obtained at 10 mTorr for n_{H^-} is only $2.0 \times 10^{15}\,m^{-3}$, as can be seen from the last and fifth curve labelled '2 and 3 and 4'. Actually, a further reason for the lower value obtained for n_{H^-} is the difference in the assumed values of k_{ds}, determining n_H and consequently n_{H^-}, along with possible differences in the value of γ_{rec}. However, a closer comparison between the numerical results for n_{H^-} obtained using the different models is difficult to justify since they reproduce plasmas in different multicusp ion sources geometries and working in different modes.

This analysis shows that the value of the ratio n_{H^-}/n_e obtained by GMS calculated for an H_2 plasma produced in DENISE working in the cw rf mode, with the negative ion production mechanisms considered in our model, is always significantly less than 0.1, for whatever optimistic (and realistic) assumptions affecting the value of n_{H^-} that can be put forward.

2.5 Summary

A global model of an rf inductively coupled H_2 plasma discharge in DENISE has been developed and implemented by using the numerical code GMS. The method has been explained and also validated by comparing its results with the available experimental measurements in the negative ion source. The effect of the reentrant cavity containing the rf antenna and of the multicusp magnetic field on the discharge have been taken into account in the model.

A more detailed global model of the plasma discharge is used to study the H^- kinetics and to calculate the H^- density both in the driver and in the extraction chamber under certain assumptions when the magnetic filter is activated. The H^- main production mechanism assumed in the model is DA of $H_2(v \leq 9)$. The differences in the cross section data assumed for some processes between this and previous work are pointed out, along with their consequences for the H^- density. The value of the ratio n_{H^-}/n_e obtained using GMS for the negative ion production mechanism considered is always significantly less than 0.1, even under the most optimistic assumptions for H^- production that can be put forward.

The kinetics of other species included in the model and how their concentration changes when one of the control parameters of the discharge varies has been studied. H_3^+ is the dominant positive ion species in the pressure range considered for input power values less than 1000 Watt, while the H^+ density reaches the same order of magnitude or becomes higher than the H_3^+ density if the power is a few thousand Watt.

Chapter 3

Particle-In-Cell simulations

PIC simulations have been used to model plasmas since the 1950's [29, 75, 76] The development of new algorithms, allowing to model the physical system of interest in more detail, for example by including the effect of collisions, and the increasing computer calculation speed generally available have been improving PIC simulation effectiveness since their introduction In PIC simulations the plasma behaviour can be reproduced in detail by evolving a relatively small number ($10^4 - 10^6$) of computer particles, each of them representing $10^6 - 10^{10}$ real plasma particles, if certain numerical constraints are satisfied The new positions and velocities of computer particle are calculated by solving their motion equations and the field equations expressed in finite difference form PIC simulations are the subject of this chapter

In section 3 1 the features and basics of the generally used PIC method is explained In section 3 2 the different steps of the calculation cycle generally used in PIC codes are described The Electrostatic Particle-in-Cell Interfaceable Code (EPIC) is the implementation of the PIC method developed and used to perform the work presented in the following chapters In section 3 3 the main features and capabilities of EPIC are described In sections 3 4-3 9

details of the implementation of the various steps of the calculation cycle in EPIC are explained.

3.1 Basics and main features of the method

The main assumptions made in PIC models are here presented. Each of the computer particles, called also superparticles, whose dynamics is followed in the model, represents many more real plasma particles. Computer particles have size of the order of the step Δx of the mathematical mesh, whose points are the only positions where the values of the field are calculated by solving the field equations.

By knowing the position and velocity of all computer particles at a certain time, the same quantities can be advanced a time later by the time step Δt by integration of their motion equations, so the position and velocity of the plasma computer particles are known only on a discrete number of points on the time axis. To guarantee the stability of the solution and to avoid the occurrence of undesired non-physical effects in the simulation, some stability and accuracy conditions must be satisfied by the time step Δt and the step of the mathematical mesh Δx used in the motion and field equation in finite differences form. The first condition

$$\frac{\Delta x}{\lambda_{De}} < 1 \tag{3.1}$$

requires Δx to resolve the electron Debye length λ_{De}, the characteristic scale length of the plasma. The second one

$$\omega_{pe}\Delta t < 0.2 \tag{3.2}$$

requires Δt to resolve the inverse of the electron plasma frequency ω_{pe}, which is the fastest time scale characterizing the system if the magnitude B of the

static magnetic field possibly present in the system is such as $\omega_{ce} \ll \omega_{pe}$, with

$$\omega_{ce} = \frac{eB}{m_e} \tag{3.3}$$

being the electron cyclotron frequency. The condition on the time step may be significantly less strict if an implicit method [32] is used to solve the equations. The number of superparticles in the simulation should be high enough to reduce the numerical noise and associated self-heating [32].

Apart from their finite size, computer particles used in this model differ from point particles because they are allowed to cross each other in their motion, but the effect of collisions is taken into account by a Monte Carlo algorithm. Collisions are modelled as instantaneous events and are allowed to happen only at a discrete number of points of the time axis, therefore collisional and collisionless motion of the computer particles are decoupled. Usually, in PIC methods the particle positions can be evolved in less than 3 space coordinates, if the system has certain symmetry properties. That allows the simulation to run much faster, but the particle velocity can still be evolved on all 3 components, to keep the full 3-dimensional character of the collision [33] in the model, at no particularly high extra computational cost.

3.2 The calculation cycle

The calculation cycle in PIC codes is as follows. By knowing the generic superparticle position and velocity values at the current time and the force acting on the superparticle, its equation of motion can be integrated to find its position and velocity at the next allowed time. The motion equation used are the same that would be used for real particles, because computer and real particles have the same charge-mass ratio. After that it is checked whether each particle pushed is still in the spatial domain of the simulation. Any particle

out of the domain is removed, while the remaining pushed particles are allowed to be subject to instantaneous collisions at this stage. The possible effect of collisions are: change of colliding particle velocity, colliding particle loss and new particles production. A Monte Carlo algorithm [33] is used to determine whether particles suffer collisions and which kind of collision. Necessary input data are the cross sections of all collisions to be included in the model in the energy range of interest. A particle that has gone out of the spatial domain may cause emission of particles from the boundary, as it happens in secondary emission. The emitted particles are added to the simulation after the field equations are solved. After that stage the particles created by collisions are added too, and the particles lost through collisions are removed. By assigning the computer particles to the points of the mathematical mesh with a suitable weighting procedure, the source terms of the field equations (for example, charge density and current density for Maxwell's equations) in the points of the mesh can be obtained. After particle weighting, the field equation, expressed in finite difference form, can be solved with the necessary boundary conditions set, to obtain the values of the field(s) in the mesh points. Finally the force acting on each computer particle can be obtained by interpolating the field from the mesh to the particle position, generally by using the inverse of the weighting procedure used for obtaining the source terms of the field equations from the particle states. This procedure is much faster than calculating the field produced in the position of a generic particle by all other particles.

3.3 The EPIC code

For the purposes of this thesis, but not only, a PIC code modelling a plasma discharge in 2D cylindrical geometry was needed. Numerical results obtained from such code could be directly compared to experimental measurements

obtained in an experiment developed in parallel to the numerical model and described in some detail in subsection 5.3.1. Moreover, the PIC code had to be developed in a way to facilitate its planned interaction with the GMS code, that was already up and running. Therefore a reasonably simple interface between the two codes had to be implemented in both of them, allowing the codes to either do their calculation independently from each other, or to use results obtained by the other code as input data to be suitably processed, before starting, or restarting, the calculation. After some consideration it was concluded that the best way to progress in the project was to make the effort to design and write entirely the PIC code needed, as already done with GMS, instead of starting to work from an existing PIC code and probably make a similar effort to make the radical changes needed to obtain the desired results. The references in this chapter and the implementation of the PIC method developed by Miles Turner were useful starting points for the development of EPIC.

Initially, EPIC was intended to be a 2D PIC code working only in cylindrical geometry with a rectangle on the rz plane as spatial domain, but for testing reasons it became necessary to implement also the 2D Cartesian geometry and the 1D ones. EPIC can perform electrostatic bounded plasma simulations of rf capacitive plasmas. EPIC is an electrostatic code because the Poisson equation is the only field equation to be solved. For our modelling purposes this is a sufficient approximation because electromagnetic effects would become important only if the driving frequency was much bigger than the 13.56 MHz, generally used in the rf capacitive coupled plasma discharges subject of this investigation. For a discussion of electromagnetic effects in large area capacitive discharges read [77].

In the following sections of this chapter the features of EPIC are described,

along with a more detailed explanation of various parts of the calculation cycle of the PIC method.

3.4 Integration of the motion equations

At the beginning of the simulation the computer particles are loaded with uniform density and a Maxwellian velocity distribution at the selected species temperature. Mixed-radix digit-reversed number sets [75, p. 390] are used to perform this loading in the computational phase space. The motion equations actually solved in the simulation in 1D or in 2D Cartesian geometry are

$$\frac{d\tilde{r}_i}{d\tilde{t}} = \tilde{v}_i; \qquad \frac{d\tilde{v}_i}{d\tilde{t}} = \frac{\Delta t^2}{\Delta r_i}\,\frac{q}{m}E_i; \qquad i = 1, N_d, \tag{3.4}$$

which are expressed in the adimensional coordinates defined here below

$$\tilde{r}_i = \frac{r_i}{\Delta r_i}; \qquad \tilde{v}_i = v_i\frac{\Delta t}{\Delta r_i}; \qquad i = 1, N_d, \tag{3.5}$$

where N_d is the number of spatial coordinates advanced in the simulation, Δt is the time step chosen for advancing the state of the particle of the species of interest, Δr_i is the distance between the points of the mesh between the particle position in the i-th coordinate, $\frac{q}{m}$ is the charge to mass ratio for the species of interest and E_i is the i-th component of the electric field calculated at the particle position. In the case of cylindrical geometry, the motion equations to be used are described in appendix A.

Subcycling techniques [32] allow the increase of calculation speed, by advancing the position and velocity of ion particles, that are heavier and generally much slower than electrons, less often. Subcycling is implemented in EPIC.

The algorithm chosen to integrate the equations of motion in EPIC is the simple and widely used leapfrog method [75, p. 13]. By replacing in the equations 3.4 the derivatives with time centred finite difference approximations

and using the result $\Delta\tilde{t} = \frac{\Delta t}{\Delta t} = 1$, easily obtained by the definition $\tilde{t} = \frac{t}{\Delta t}$, the equations

$$\tilde{r}_i^{(new)} = \tilde{r}_i^{(old)} + \tilde{v}_i^{(old)}; \quad \tilde{v}_i^{(new)} = \tilde{v}_i^{(old)} + \frac{\Delta t^2}{\Delta r_i}\frac{q}{m}E_i^{(new)}; \quad i = 1, N_d \tag{3.6}$$

are obtained. In the leapfrog algorithm the position and the velocity of the particle must be known at different times to improve the accuracy of the finite differences approximations used. That means that if

$$\tilde{r}_i^{(old)} = \tilde{r}_i(t) \qquad \tilde{r}_i^{(new)} = \tilde{r}_i(t + \Delta t), \tag{3.7}$$

then it must be

$$\tilde{v}_i^{(old)} = \tilde{r}_i(t + \frac{1}{2}\Delta t) \qquad \tilde{v}_i^{(new)} = \tilde{v}_i(t + \frac{3}{2}\Delta t). \tag{3.8}$$

The leapfrog method guarantees a second order accuracy in time. It is attractive for a numerical implementation, because its simplicity makes it reasonably fast, but it must satisfy the stability condition 3.2 (on the other hand, implicit methods [32] do not have that constraint on the choice of time step, but they require more operations and are more complicated to implement [32]).

3.5 The Monte Carlo collision handler

The Monte Carlo collision handler implemented in EPIC can handle collisions of superparticles of the simulated species with neutrals having a certain constant density and a Maxwellian velocity distribution. At this stage, EPIC can not handle binary collisions between superparticles.

The probability that a particle having constant velocity v and kinetic energy $\mathcal{E} = \frac{m}{2}v^2$ suffers a collision moving during a time step Δt is given by

$$P_1 = 1 - \exp(-\Delta t\, v\, \sigma(\mathcal{E})\, n), \tag{3.9}$$

where $\sigma(\mathcal{E})$ is the total collision cross section for a particle having kinetic energy $\mathcal{E}$ and n is the background neutral density. No more than one collision per calculation cycle per particle is allowed in this method, therefore Δt should be so small that the probability that a particle suffers two or more collisions during the time range Δt is negligible. The total collision cross section is equal to the sum of the cross sections of each collision process included in the model for the species of interest.

To make the algorithm faster, particularly when particles are not subject to collisions, a fictitious collision process, called null collision process [33] because it has no effect on the colliding particle, can be added to the list. The total collision frequency $\nu = v\,\sigma(\mathcal{E})\,n$ is, typically, velocity dependent; resulting in P_1 to be calculated separately for each particle. The null collision process cross section is suitably chosen to make the total collision frequency ν constant over all the energy range under consideration. In this case P_1 can be calculated more easily with formula 3.9, because P_1 depends only on ν and Δt. Moreover, with the addition of the null collision process, formula 3.9 is true also in the more general case where v is not constant over the time range Δt. After a particle is pushed, a pseudorandom number $R_1 \in [0, 1]$ is generated and that particle can be subject to collision only if $R_1 < P_1$. If that is the case, then the ratio P_2 of the total cross section without null collision process to the total cross section with null collision process at the energy $\mathcal{E}$ will be defined. After that another pseudorandom number $R_2 \in [0, 1]$ is generated. If $R_2 > P_2$ the particle is subject to a null collision, namely to no collision, otherwise the particle is subject to a collision, whose kind is determined by the value of R_2 and the value of the cross section of each of the collision process included in the model for that species with the neutral background at the energy $\mathcal{E}$.

3.6 Calculating the mesh points coordinates

The selection of the mathematical mesh points depends on the geometry of the simulation. In 1D geometry the spatial domain is a segment, while in 2D is a rectangle. The mathematical mesh to be used in 1D and 2D Cartesian geometry is uniform. So if a mesh of $N+1$ points has to be set on the spatial domain $[x_{min}, x_{max}]$, then the coordinates of the mesh points are defined as

$$x_i = x_{min} + \frac{i}{N}(x_{max} - x_{min}); \quad i = 0, N. \tag{3.10}$$

Instead, in the radial coordinate of the 2D cylindrical geometry the mesh points can be chosen so that the volumes between consecutive mesh points is constant. For example if a mesh of $N+1$ points has to be set on the spatial domain $[r_{min}, r_{max}]$, then the mesh points will be

$$r_i = \sqrt{r_{min}^2 + \frac{i}{N}(r_{max}^2 - r_{min}^2)}; \quad i = 0, N. \tag{3.11}$$

This non uniform mesh is particularly convenient for the radial coordinate of 2D cylindrical geometry, having $r_{min} = 0$, because the volume between adjacent grid points is constant and therefore the average number of superparticles near each grid point depend only on the density of that species. With a uniform mesh, the different volume between grid points would cause fewer computer particles to be near grid points where the volume is small. That could cause undesired noise in the simulation especially in the region on and around the cylindrical axis.

3.7 Calculating the charge density on the mesh

In PIC simulations the source terms of the field equations on the mesh points can be obtained by using different weighting procedure of the superparticles

on the mesh [75, p. 19]. The procedure used in EPIC to calculate the charge density on the points of a uniform mathematical mesh from the superparticle positions is the first-order weighting [75, p. 20]. For example in 1D the charge q of a superparticle having coordinate $x_i \leq x \leq x_{i+1}$ is assigned to the mesh points x_i and x_{i+1} in this way: the fraction wq, with w defined as

$$0 \leq w = \frac{x - x_i}{\Delta x} \leq 1; \quad x_{i+1} - x_i = \Delta x, \quad \forall i = 0, N-1 \tag{3.12}$$

is assigned to the grid point x_{i+1}, while the remaining part $(1-w)q$ is assigned to the grid point x_i. If we assume each mesh point x_i has a corresponding cell Δx long, whose centre is x_i itself, and the superparticle charge is distributed uniformly on a segment, whose centre is in x, then the superparticle charge assigned to either mesh point will be the part that lies in the cell associated to it. After the charge of all particles is assigned to the mesh grid points, the charge density at the i-th grid point, ρ_i, is calculated by dividing the total charge assigned to the i-th grid point, q_i, by the cell volume Δx. The extension of this particle weighting procedure to a 2D uniform (Cartesian) mesh is straightforward and can be found in [75, p. 311].

For the nonuniform mesh used in 2D cylindrical geometry, the fraction w needs to be calculated in a different way. Let us examine for simplicity only the particle weighting on the radial coordinate. A superparticle has coordinate r such as $r_i \leq r \leq r_{i+1}$ and the mesh points r_i and r_{i+1} are defined by 3.11. The charge of the superparticle is uniformly distributed in a region of area $S = \pi(r_1^2 - r_{min}^2)$, whose centre is in r. The boundary point of the generic adjacent cells, whose centre is in the mesh points r_i and r_{i+1}, is

$$r_{i+\frac{1}{2}} = \sqrt{r_{min}^2 + \frac{i+\frac{1}{2}}{N}(r_{max}^2 - r_{min}^2)}. \tag{3.13}$$

If we assume, as in the case of the uniform mesh, that the charge of the superparticle assigned to either mesh point is the charge lying on the associated

cell, after some calculations it is obtained that the value of w to be used is

$$w = a(a + 2\sqrt{i + \frac{\pi r_{min}^2}{S}}); \quad a = \sqrt{\frac{\pi}{S}}(r - r_i). \tag{3.14}$$

The rest of the particle weighting procedure is the same already described for a uniform mesh, except that the cell volumes are obviously different.

3.8 Integration of the field equation

The electrostatic field generated by a certain charge distribution can be obtained by solving the Poisson equation

$$\nabla^2 \Phi(\mathbf{r}) = -\frac{\rho(\mathbf{r})}{\varepsilon}, \tag{3.15}$$

with Φ being the electric potential, ρ the charge density and ε the dielectric constant, which inside the plasma is equal to ε_0. The Gauss law

$$\oint_S \mathbf{E}(\mathbf{r}) \cdot d\mathbf{S} = \int_V \frac{\rho(\mathbf{r})}{\varepsilon}\, dV + \oint_S \frac{\sigma(\mathbf{r})}{\varepsilon}\, dS, \tag{3.16}$$

is equivalent to the Poisson equation. $\mathbf{E}$ is the electric field, S a certain closed surface, V the volume surrounded by S, and σ the possible surface charge density on S. Both equations can be a starting point to obtain a numerical solution of the field equation to be used in EPIC. In 2D cylindrical geometry it is convenient to choose the Gauss law [75], instead for all other cases the Poisson equation can be chosen.

3.8.1 One dimension

In all 1D geometries a uniform mesh is used. The Laplace operator in 1D Cartesian geometry expressed by finite differences between the points of the mesh is

$$\nabla^2 = \frac{\partial^2}{\partial x^2} \longrightarrow (\nabla^2 \Phi)_i = \frac{\Phi_{i-1} - 2\Phi_i + \Phi_{i+1}}{(\Delta x)^2} \tag{3.17}$$

where $\Phi_i = \Phi(x_i)$. The equation 3.15 in the mesh points becomes

$$\frac{\Phi_{i-1} - 2\Phi_i + \Phi_{i+1}}{(\Delta x)^2} = -\frac{\rho_i}{\varepsilon}, \quad \forall i = 1, N-1. \tag{3.18}$$

Instead in radial geometry it results

$$\nabla^2 = \frac{1}{r}\frac{\partial}{\partial r}(r\frac{\partial}{\partial r}) = \frac{\partial^2}{\partial r^2} + \frac{1}{r}\frac{\partial}{\partial r} \longrightarrow (\nabla^2\Phi)_i = \frac{(1 - \frac{\Delta r}{2r_i})\Phi_{i-1} - 2\Phi_i + (1 + \frac{\Delta r}{2r_i})\Phi_{i+1}}{(\Delta r)^2} \tag{3.19}$$

and the equation 3.15 in the mesh points becomes

$$\frac{(1 - \frac{\Delta r}{2r_i})\Phi_{i-1} - 2\Phi_i + (1 + \frac{\Delta r}{2r_i})\Phi_{i+1}}{(\Delta r)^2} = -\frac{\rho_i}{\varepsilon}, \quad \forall i = 1, N-1 \tag{3.20}$$

In the model two electrodes lie at the ends of the spatial domain. One is grounded while the other one is driven by either a voltage or a current source. The boundary conditions for equations 3.18 and 3.20 are satisfied by suitably setting the values of the electric potential at both ends of the spatial domain, where the two electrodes are. In the grounded electrode position it always results $\Phi_N = 0$, while the electric potential at the driven electrode position, $\Phi_{de} = \Phi_0$, can be set in different ways depending on which kind of power source is chosen.

Both set of equations 3.18 and 3.20 are made of $N-1$ algebraic linear equations having as unknowns $\Phi_i; i = 1, N-1$. They can be expressed in matrix form by tridiagonal matrices, so called because they have non-zero elements only in the main diagonal and in the two adjacent diagonals. In EPIC these tridiagonal set of equations can be solved with the algorithm described in appendix B.

To solve the field equations at every time step in EPIC the following procedure is used [31]. First, the finite differences form of the Laplace equation

$$\nabla^2\Phi(\mathbf{r}) = 0 \tag{3.21}$$

with $\Phi_0 = 1$ is solved at the beginning of the simulation to obtain Φ^L. Then at every computational step the Poisson equation with $\Phi = 0$ in all boundary mesh points is solved to obtain Φ^P. After that, the electric potential at the driven electrode $\Phi_{de} = \Phi_0$ is calculated. Finally, the electric potential in the points of the mesh, satisfying the boundary conditions set, is

$$\Phi = \Phi^P + \Phi_{de}\Phi^L, \tag{3.22}$$

because from the superposition principle [31], it follows that the solution of equation 3.15, with arbitrary boundary conditions, is equal to the sum of the solution of the equation 3.15, with $\Phi = 0$ in the whole boundary, and of the solution of the Laplace equation, with the original boundary conditions.

In the voltage source case Φ_{de} is set as

$$\Phi_{de} = V(t) = \tilde{V}_{rf}\sin(\omega t). \tag{3.23}$$

In the current source case the Gauss law 3.16 is used to obtain its value [78]. In Cartesian geometry let us define a box having bases of area A parallel to the driven electrode surface, in this case perpendicular to the x axis, of height $h = \frac{\Delta x}{2} + \delta$ and situated in the range $[x_0 - \delta, x_0 + \frac{\Delta x}{2}]$, with $\delta \ll \Delta x$ and $\delta < d_{de}$, being d_{de} the electrode thickness. By applying the Gauss law on that box it results

$$E_{\frac{1}{2}}A = \frac{1}{\varepsilon}(\sigma A + \rho_0 A\frac{\Delta x}{2}), \tag{3.24}$$

with $E_{\frac{1}{2}} = E(x_0 + \frac{\Delta x}{2})$ and σ is the surface charge density on the driven electrode. The only contribution to the electric flux comes from $E_{\frac{1}{2}}$, because the electric field component parallel to the electrode must be zero for the symmetry of the system and the electric field $E(x_0 - \delta)$ must be zero, because $x_0 - \delta$ is in the interior of the electrode, which is a conductor. By using a finite difference approximation of the electric field and using the explicit expressions

of Φ_1 and Φ_0 we obtain

$$E_{\frac{1}{2}} = -\frac{\Phi_1 - \Phi_0}{\Delta x} = -\frac{(\Phi_1^P + \Phi_{de}\Phi_1^L) - \Phi_{de}}{\Delta x} \tag{3.25}$$

which inserted in 3.24 gives

$$\Phi_{de} = \frac{\sigma + \rho_0 \frac{\Delta x}{2} + \frac{\varepsilon}{\Delta x}\Phi_1^P}{\frac{\varepsilon}{\Delta x}(1 - \Phi_1^L)}. \tag{3.26}$$

Defining

$$\Delta\sigma = \sigma(t + \Delta t) - \sigma(t) \tag{3.27}$$

by charge conservation [78] we obtain

$$A\Delta\sigma = \Delta Q_P + A\int_t^{t+\Delta t} dt' J(t'), \tag{3.28}$$

with ΔQ_P being the charge of the plasma particles deposited on the electrode between t and $t + \Delta t$ and

$$J(t) = \tilde{J}_{rf}\sin(\omega t). \tag{3.29}$$

is the current density delivered by the external source. From equations 3.27 and 3.28

$$\sigma(t + \Delta t) = \sigma(t) + \frac{\Delta Q_P}{A} + \int_t^{t+\Delta t} dt' J(t') \tag{3.30}$$

is obtained. The formula 3.30 is used in EPIC to calculate the charge density after the system has advanced by one time step Δt.

3.8.2 Two dimensions

The Laplace operator in 2D Cartesian geometry expressed by finite differences between the points of the uniform mesh having $M + 1$ points in any row and $N + 1$ points in any column in the rectangular domain of the plane xy is

$$\nabla^2 = \frac{\partial^2}{\partial x^2} + \frac{\partial^2}{\partial y^2} \longrightarrow (\nabla^2\Phi)_{i,j} = \frac{\Phi_{i-1,j} - 2\Phi_{i,j} + \Phi_{i+1,j}}{(\Delta x)^2} + \frac{\Phi_{i,j-1} - 2\Phi_{i,j} + \Phi_{i,j+1}}{(\Delta y)^2} \tag{3.31}$$

where $\Phi_{i,j} = \Phi(x_i, y_j)$. The equation 3.15 in the mesh points becomes

$$\frac{\Phi_{i-1,j} - 2\Phi_{i,j} + \Phi_{i+1,j}}{(\Delta x)^2} + \frac{\Phi_{i,j-1} - 2\Phi_{i,j} + \Phi_{i,j+1}}{(\Delta y)^2} = -\frac{\rho_{i,j}}{\varepsilon}$$
$$\forall i = 1, M-1; \quad \forall j = 1, N-1 \tag{3.32}$$

which is a system of $N_{tot} = (M-1)(N-1)$ linear equations. By setting

$$\Phi_k = \Phi_{i,j}; \quad k = (M-1)(j-1) + (i-1), \tag{3.33}$$

the unknowns are $\Phi_k; k = 0, N_{tot}-1$. The system of N_{tot} linear equations can be expressed in matrix form by a sparse matrix which can have non zero elements in the main diagonal and the two adjacent ones, as a tridiagonal matrix, and the two diagonals starting from the elements at the first row and the M-th column and the first column and the M-th row, and going downwards.

To calculate the electric potential at the mesh points on the 2D spatial domain, the procedure already described in subsection 3.8.1 is used: firstly solving the Laplace equation with $\Phi = 1$ on the driven electrode mesh points and $\Phi = 0$ on the grounded electrode mesh points to calculate Φ^L, secondly solving the Poisson equation with $\Phi = 0$ on the whole boundary to calculate Φ^P, thirdly by calculating the electric potential on the driven electrode Φ_{de} and finally by using 3.22.

The methods used in EPIC to calculate Φ^L and Φ^P in 2D geometries are necessarily more complex than the one used in 1D, because of the more complex structure of the matrix associated with the system of equations above described. To calculate Φ^L the Dynamic Alternate Direction Implicit (DADI) method [79] [76, p. 182], explained in appendix C, is used. To calculate Φ^P the Buneman variant [80, 81] of the cyclic reduction method [76, p. 201], explained in appendix D, is used. A cyclic reduction method was chosen because it proved to be very fast and can solve the field equation on the non-uniform

mesh used in 2D cylindrical geometry Moreover, the simple boundary condition, $\Phi = 0$ on the whole boundary, allows using this fast method [76, p 201], which instead can not be used to calculate Φ^L, because in that case the boundary condition is too complex That is why the slower DADI technique is used to solve the Laplace equation and calculate Φ^L, this does not affect the calculation time severely, because Φ^L has to be calculated only once, at the beginning of the simulation

It has to be observed that other algorithms, for example successive over relaxation [76, p 179], are more suitable to increase the calculation speed if parallel computing is used [82] Moreover, cyclic reduction can be used only when the equation is separable, therefore it could not be used if an implicit method was used in EPIC to solve the field equation [82]

To calculate Φ_{de} in 2D the fact that the driven electrode lies on more than one mesh point has to be taken into account Let us consider the case where the driven electrode occupies the cells associated with the grid points (x_i, y_0), $i = 1, M-1$ For the case where the electrode is driven by a current source, if Gauss' law is applied to a box defined in a similar way as in the 1D case, with the area A of its bases being equal to the driven electrode area, we obtain

$$\Phi_{de} = \frac{\sigma A + \sum_{i=1}^{M-1} \rho_{i,0} \frac{\Delta y}{2} \Delta S_i + \frac{\varepsilon}{\Delta y} \sum_{i=1}^{M-1} \Phi_{i,1}^P \Delta S_i}{\frac{\varepsilon}{\Delta y} \sum_{i=1}^{M-1} (1 - \Phi_{i,1}^L) \Delta S_i} \tag{3 34}$$

The difference between this formula and 3 26 is that the area A of the driven electrode and the area ΔS_i of the cells of the driven electrode mesh points enter in 3 34 but not in 3 26 In the case of a voltage source, the effect of the blocking capacitor, inserted in the circuit to prevent dc currents, has been included The voltage between the capacitor plates is

$$V_c = \Phi_{de} - V_{rf} \tag{3 35}$$

and the current in the circuit is

$$I(t) = -\frac{dQ_c}{dt} = -C_b\frac{dV_c}{dt} = -C_b\frac{d(\Phi_{de} - V_{rf})}{dt} \tag{3.36}$$

with Q_c the charge on the capacitor and C_b its capacitance. The contribution of the circuit current to σ, namely the last term on the r.h.s of equation 3.30, calculated from the equation 3.36 is

$$\int_t^{t+\Delta t} dt' J(t') = \frac{C_b}{A}[V_{rf}(t+\Delta t) - \Phi_{de}(t+\Delta t) - V_{rf}(t) + \Phi_{de}(t)]. \tag{3.37}$$

and therefore

$$\sigma(t+\Delta t) = \sigma(t) + \frac{\Delta Q_P}{A} + \frac{C_b}{A}[V_{rf}(t+\Delta t) - \Phi_{de}(t+\Delta t) - V_{rf}(t) + \Phi_{de}(t)]. \tag{3.38}$$

By inserting 3.38 in 3.34, after defining

$$\Delta\sigma = \frac{C_b}{A}[V_{rf}(t+\Delta t) - V_{rf}(t) + \Phi_{de}(t)], \tag{3.39}$$

we obtain

$$\Phi_{de}(t+\Delta t) = \frac{[\sigma(t) + \frac{\Delta Q_P}{\Delta t} + \Delta\sigma]A + \sum_{i=1}^{M-1}\rho_{i,0}\frac{\Delta y}{2}\Delta S_i + \frac{\varepsilon}{\Delta y}\sum_{i=1}^{M-1}\Phi_{i,1}^P\Delta S_i}{\frac{\varepsilon}{\Delta y}\sum_{i=1}^{M-1}(1-\Phi_{i,1}^L)\Delta S_i + C_b}. \tag{3.40}$$

To solve the the field equation in cylindrical geometry the same procedure just described can be used, but the system of linear equations to be solved has to be obtained starting from the Gauss law [75, p. 333], not from the Poisson equation. The resulting equations are:

$$\frac{-4\Phi_{0,j} + 4\Phi_{1,j}}{(r_1 - r_0)^2} + \frac{\Phi_{0,j-1} - 2\Phi_{0,j} + \Phi_{0,j+1}}{(\Delta z)^2} = -\frac{\rho_{0,j}}{\varepsilon}; \quad \forall\, j = 1, N-1 \tag{3.41}$$

which is obtained by applying the Gauss law on the cylindrical spatial region, whose axis is $r_0 = 0$, defined by

$$r \in [r_0 = 0, \frac{r_0 + r_1}{2}], \quad z \in [\frac{z_{j-1} + z_j}{2}, \frac{z_j + z_{j+1}}{2}],$$

and

$$\frac{1}{\Delta r_{i-1}\Delta r_i}[\frac{\Delta r_i(2r_i-\Delta r_{i-1})}{r_i(\Delta r_{i-1}+\Delta r_i)}\Phi_{i-1,j}-2\Phi_{i,j}+\frac{\Delta r_{i-1}(2r_i+\Delta r_i)}{r_i(\Delta r_{i-1}+\Delta r_i)}\Phi_{i+1,j}]+$$

$$\frac{\Phi_{i,j-1}-2\Phi_{i,j}+\Phi_{i,j+1}}{(\Delta z)^2}=-\frac{\rho_{i,j}}{\varepsilon}$$

$$\forall\, i=1,M-1;\quad \forall\, j=1,N-1 \tag{3.42}$$

with

$$\Delta r_i = r_{i+1}-r_i \quad i=1,M-1 \tag{3.43}$$

which is obtained by applying the Gauss law on the spatial region defined by

$$r\in[\frac{r_{i-1}+r_i}{2},\frac{r_i+r_{i+1}}{2}],\quad z\in[\frac{z_{j-1}+z_j}{2},\frac{z_j+z_{j+1}}{2}].$$

It has to be remarked that the values of $\rho_{i,j}$ to be used in these equation must be calculated in cells having boundaries midway through two adjacent mesh points also in the radial direction. But, as explained in section 3.6, the charge density in cylindrical geometry in EPIC is calculated in cells having the same volume and boundary points defined by the formula 3.13. For this reason the charge densities $\rho_{i,j}$ to be used in the equations 3.41 and 3.42 have to be calculated by interpolation of the charge densities $\rho'_{i,j}$, obtained in the way described in section 3.7, by using these formulae

$$\rho_{0,j}=\rho'_{0,j}$$

$$\rho_{i,j}=(t-\frac{1}{4})\rho'_{i-1,j}+(\frac{5}{4}-t)\rho'_{i,j}$$

$$t=[\frac{\sqrt{i}}{2}(\sqrt{i}-\sqrt{i-1})],\quad i=1,M-1 \tag{3.44}$$

3.9 Field calculation at the particle position

To calculate the force acting on each particle from the electric potential calculated in the mesh points, it is necessary first to calculate the electric field

in the mesh points and then to make an interpolation to the particle position. The electric field in 1D calculated by

$$E_i = -\frac{\Phi_{i+1} - \Phi_{i-1}}{2\Delta x} \tag{3.45}$$

and the two components of the electric field in 2D are calculated in a similar way. From these values we calculate

$$E(x) = (1 - w)E_i + wE_{i+1}, \tag{3.46}$$

the electric field on the particle position $x_i \leq x \leq x_{i+1}$ by using the same fractions w and $1 - w$ defined in 3.12, as suggested in [75, p. 162].

3.10 Summary

In this chapter first the basics and the general features of the PIC method have been described. Then its implementation in EPIC, the numerical code developed and used to perform the work presented in the following of this thesis, has been explained. EPIC has been tested and validated by modelling rf capacitively coupled argon plasma discharges in 2-D and comparing some of the results obtained with independent numerical results obtained at the same conditions [31]. This comparison is presented in appendix E.

Chapter 4

Coupling global model and particle simulation

In this chapter a numerical scheme coupling global model and PIC/MC simulation, the models presented in chapters 2 and 3, able to model rf capacitively coupled plasma discharges with complex chemistry, is explained in detail, along with its implementation performed in the numerical codes EPIC and GMS. One of the main motivations for developing this scheme was to model self-consistently in rf H_2 capacitive plasma discharges the negative ion volume production by DA of $H_2(0 \leq v \leq 9)$, v being the vibrational excitation level of the hydrogen molecule. With an increase in the value of v, the cross section of this DA collision process increases dramatically [83, 69] and the threshold energy decreases. Both effects increase the rate constant of the collision process. But, as explained in chapter 3, usually in PIC/MC simulations of rf plasmas only charged species particles are simulated, while the neutral densities are set arbitrarily. Therefore, modelling self-consistently the negative ion production by DA in a conventional PIC model is not possible, because the densities of $H_2(v)$ for the values of v of interest are not calculated. In the coupling scheme

presented in this chapter the global model is used to calculate the densities of $H_2(v)$.

The idea behind this numerical scheme is to use the results of a global model of the PIC simulated plasma to obtain an estimation of the densities of both charged and neutral species in the discharge in the steady state. These densities are calculated in the global model, where all volume collision processes included in the PIC and the collision processes needed to model the kinetics of the neutrals have to be included. Then, these data are delivered to the particle simulation code, where they are used to suitably modified the densities of both charged and neutral species before the simulation continues. This coupling scheme was designed to model self-consistently rf plasma discharges with complex chemistry, but it seems also plausible to obtain a significant acceleration of the convergence of the simulated plasma toward its steady-state, with consequent saving of computational time.

To obtain the desired coupling between the two models, it is necessary to modify the global model in such a way that it is able to accept quantities calculated in the particle simulation as input data and to include properly those data in the set of equations to be solved. Using some of those data allows to reduce the number of assumptions made in the global model, as is explained in section 4.1. Consequently more reliable estimations of the average densities of the species included in the model are obtained if the global model is coupled with a particle simulation code.

In section 4.1 the changes to be done to GMS to obtain a global model of the plasma modelled by EPIC are described. In section 4.2 the diagnostics required from EPIC to make the scheme work are listed. In section 4.3 the way EPIC and GMS interact in the coupling scheme is explained. In section 4.4 a short demonstration of how the coupling scheme works is given.

4.1 Changes to be done to GMS

Some important changes need to be made in the structure of the global model, to use GMS to implement the coupling scheme explained in this chapter. The purpose of these changes is making a sensible use of the information that can be obtained from the particle simulation to estimate the average densities of the species included in the model.

Since the global model can use the EEPF obtained from the simulation, it makes sense to eliminate the electron temperature as an unknown in the set of equations. Consequently, the particle balance equation of one of the positive ion species has to be excluded as well from the set of equations of the model.

Another significant change to be made in the global model is the inclusion of an equation setting the ratio between positive and negative charge, q^+ and q^- present in the whole system equal to the value r of this quantity obtained from the PIC. This new equation

$$\frac{q^+}{q^-} = r \tag{4.1}$$

must replace the quasi-neutrality condition 2.17, because the latter is satisfied only in the plasma bulk, not in the whole spatial domain of the simulated system.

The power balance equation 2.13 should also be changed into

$$P - V \sum_{i=1}^{N_{pi}} n_i [\nu_{l,i} \mathcal{E}_{T,i} + \nu_{R,i}\ \mathcal{E}_{L,i}] = 0 \tag{4.2}$$

with n_i the time and space-averaged density of the i-th positive ion species and $\nu_{l,i}$ its loss frequency at the wall, which is obtained from the particle simulation. It has to be remarked that by using the equation 4.2 as the power balance equation of the model, the Bohm criterion and the formulae 2.15 need not to be used anymore to calculate approximately the ion flux, because that

can be obtained from the particle simulation diagnostics without making any assumption. The total energy loss per electron-i-th positive ion pair created, $\mathcal{E}_{T,i}$, is defined as

$$\mathcal{E}_{T,i} = \mathcal{E}_C + \mathcal{E}_{i,w} + \mathcal{E}_{e,w} + \mathcal{E}_{L,i}, \tag{4.3}$$

with $\mathcal{E}_C$ being the energy lost by positive ions through collisions per positive ion lost at the wall. $\mathcal{E}_C$ was not included in the formula 2.7, which is the one typically used in global models. But this energy loss can be obtained from the particle simulation and has to be included in the global model used in this numerical scheme, to model properly the energy balance in the simulated plasma. The remaining terms of equation 4.3 are the same as in equation 2.7, but the values of $\mathcal{E}_{i,w}$ and $\mathcal{E}_{e,w}$ come from the particle simulation, as well as the rate constants and the energy losses used in the definition 2.11 of $\mathcal{E}_{L,i}$.

The expression of the particle balance equations 2.1 needs not to be changed, but the rate constants k of the heavy-particles collision processes to be included are calculated in the particle simulation code from the number of events happened for the collision process of interest over a certain time range. The rate constant of the electron collision process can be calculated either with the procedure above described or by using the formula

$$k = \langle \sigma(v)\, v \rangle \tag{4.4}$$

as described in subsection 2.1.1. The latter method is very much preferable to the former one if the number of collision events counted is not big enough to make negligible the uncertainty on the rate constant due the probabilistic nature of collision events in the simulation. But the average in formula 4.4 has to be done over the EEPF obtained from the particle simulation, not by using a Maxwellian EEDF as done in chapter 2. The rate constants used in the definition 2.11 of $\mathcal{E}_{L,i}$ are calculated in the same way.

4.2 EPIC diagnostics needed by GMS

As previously explained, the global model of the plasma simulated by a particle simulation can be obtained only if certain particle simulation diagnostics results are delivered to the global model as input data Most of those data are not needed by the particle simulation to work, but, along with other diagnostics that can be implemented, they give us further insight in the behaviour of the modelled plasma In this section all data the global model needs to receive from the particle simulation code to allow the coupling scheme to work are listed

The particle balance equations needs the following data the values of the time and space-averaged density of each simulated species, the density of the neutral species, the rate constants of the volume collision processes included in the particle simulation, calculated as explained in section 4 1, the average EEPF if the rate constants of the electron collision processes are set to be calculated by using the formula 4 4, and the surface loss rates for each simulated species having a corresponding particle balance equation

The power balance equation 4 2 needs P, the power lost by the plasma, $\nu_{l,i}$, the loss frequency at the wall of the i-th positive ion species and $\mathcal{E}_{T,i}$ To calculate $\mathcal{E}_{T,i}$ by using its definition 4 3, the particle simulation code has to calculate the energy lost by positive ions through collisions per positive ion lost at the wall, $\mathcal{E}_C$, the average kinetic energy of the i-th positive ions hitting the wall, $\mathcal{E}_{i,w}$, the average kinetic energy of the electrons hitting the wall, $\mathcal{E}_{e,w}$ and $\mathcal{E}_{L,i}$ To calculate $\mathcal{E}_{L,i}$ by using its definition 2 11, the average energy losses of the relevant collision processes obtained from the particle simulation diagnostics should be used, along with their rate constant, to be calculated as explained in section 4 1

The equation 4 1, replacing the quasi-neutrality condition, needs from the

particle simulation the averaged densities of the charged species in the simulation, the average charge on the driven electrode and the ratio r of positive to negative charge present in the simulated system.

It has to be remarked that the average densities of the simulated species and the neutral densities obtained from the particle simulation will be used just as initial guess of the unknowns in the global model.

4.3 The interaction between EPIC and GMS in the coupling scheme

In the coupling scheme presented in this chapter EPIC and GMS are made to interact in the following way. Initially, EPIC starts and the simulated plasma evolves for a user chosen number of rf periods. All data needed by GMS and listed in section 4.2 are calculated in EPIC. Some of those data can be both time and space-averaged quantities, like for example the simulated species densities, only time-averaged quantities, like for example P, the power dissipated in the plasma, or rates calculated as the ratio of the number of times that a certain event happened to the time interval when those events took place. In this scheme the time range for calculating these ratios and for performing the averages over time is set as half of the time the simulation is made to evolve without interruption. The data needed by GMS and calculated in EPIC are stored into a file just before EPIC stops. After that, GMS starts to run and read the data stored by EPIC in that file. GMS uses those data to produce the set of equations to be solved in the global model. The values of the densities of the various species included in the global model are the results of the global model and they have to be interpreted as the values those densities would have in the discharge at the steady-state, if all data previously

delivered by EPIC remained constant. In fact those data can vary during the simulation, but the global model results can nevertheless be used fruitfully by EPIC. Before stopping, GMS stores in another file, r_d, the ratio of the average total positive ion density calculated by the global model to the one obtained by the data delivered by EPIC and the average densities of all species included in the model. Those data will be used to make the densities in the simulation closer to the values they will have at the steady state of the discharge.

Afterwards, EPIC starts again and reads the file containing the GMS data. The densities of the neutral species, used in EPIC only in the part of the code handling collisions, are set equal to their densities calculated by GMS. The particle weight in the simulation, i.e. the number of real particles represented by each superparticle, is multiplied by

$$r_w = 1 + (r_d - 1) f(r_d - 1) \tag{4.5}$$

with $f(r_d - 1)$ a certain function of $r_d - 1$ selected empirically. The value of r_d calculated by the global model suggests what is the future trend in the variation of the average positive ion density in the simulation. Therefore the particle weight in the simulation has to be modified accordingly. In order to do that, a possible choice of $f(r_d - 1)$ used to calculate r_w with formula 4.5 is given in appendix F.

There is another change that can be made in the simulation after GMS data are read and before the simulated plasma is allowed to evolve again. Some of the superparticles can be converted from one species into another one having the same charge so that the ratio between the averaged densities of all positively charged species and between the averaged densities of all negatively charged species is not too different from the ratios calculated using the averaged densities calculated by GMS. The position of the superparticles changing species remains the same, but their new velocity is chosen by using a

Maxwellian distribution at a certain temperature. The superparticles changing species are selected in a way to change as less as possible the shape of the density profile of the species having superparticles to be added. With this change the conversion of particles of certain species into particles of certain other species is accelerated. That is particularly useful if the production and loss rates of some of the simulated particle species are much lower than the rates of the other ones, as is the case for H^- in the rf capacitively coupled hydrogen discharges modelled in section 5.4.

After all these changes the plasma superparticles in EPIC are allowed to evolve again and thus the interaction cycle between particle simulation and global model restarts and has to be repeated until the densities of the various species reach stable values. If all densities remain nearly constant in the last few interaction cycles, then the simulated plasma has reached steady-state.

4.4 A demonstration of the coupling scheme

In this section a little demonstration is given of how the coupling scheme explained in this chapter works. In figure 4.1 the space-averaged electron density is plotted versus time. The curve with the discontinuities has been obtained by using the coupling scheme, while the smoother curve has been obtained by using only EPIC and by setting at the beginning of the particle simulation the neutral densities equal to the values obtained from the coupling scheme. The discontinuities in the first curve are at the times when EPIC stops and GMS performs its calculation. They are caused by the increase in the particle weight due to the global model results. In both cases the simulation starts with an average electron density value lower than the value it would have at the steady-state and converges toward the same value. But in the coupling scheme the convergence is significantly faster because the estimation of the

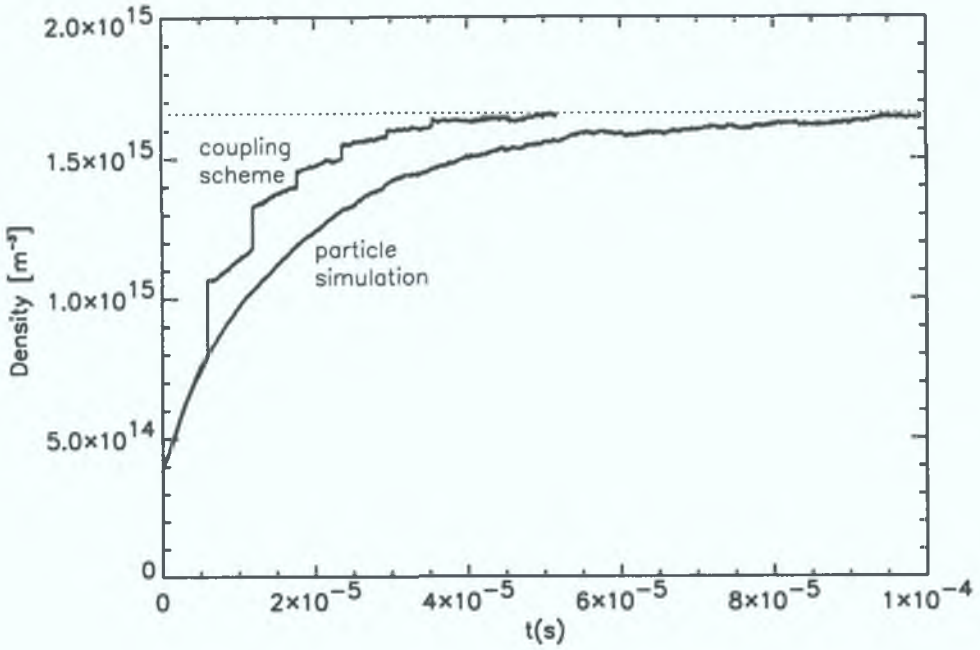

Figure 4.1: Space-averaged electron density vs. time.

densities done by the global model is used to increase by a certain fraction the particle weight and consequently the averaged electron density, causing the discontinuities in the first curve.

In figures 4.2 and 4.3 the time-averaged electron density profiles obtained at the different times with the coupling scheme and by using only EPIC are plotted. It can be noticed that the profile shown in figure 4.2, obtained with the coupling scheme, after 680 rf periods is nearly the same as that shown in figure 4.3, obtained only with EPIC, after 1360 rf periods. Both are the electron density profile in the plasma at the steady state. By comparing the curves taken after the same number of rf periods in the two cases, it can be seen that with the coupling scheme, the electron density converges faster to its steady-state profile than by using only EPIC.

In figure 4.4 we can see that the EEPFs at the steady state in the two cases can be hardly distinguished. These results clearly show that by using

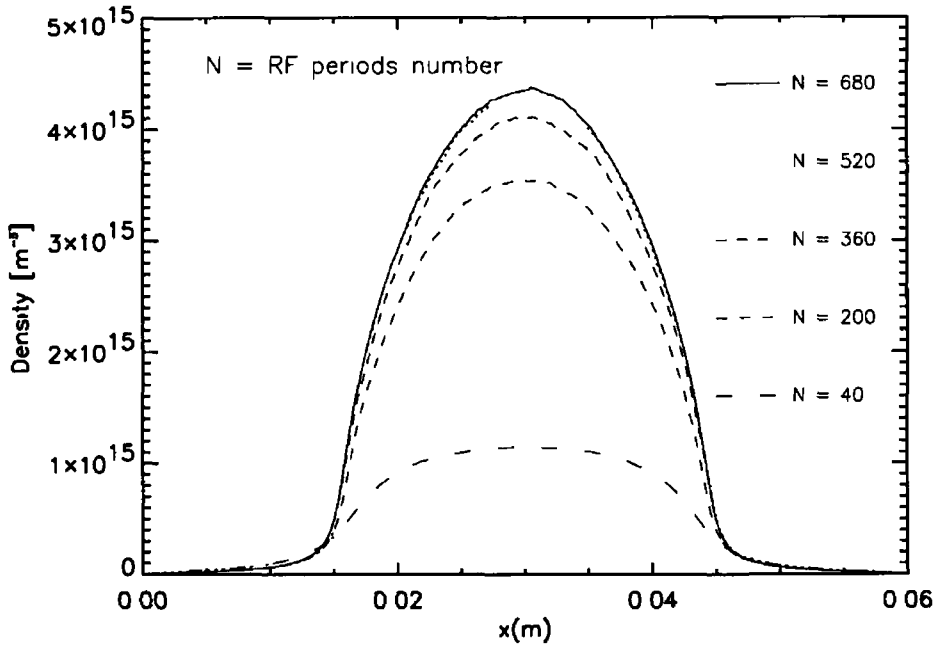

Figure 4 2 Time-averaged electron densities at different times vs space obtained with the coupling scheme

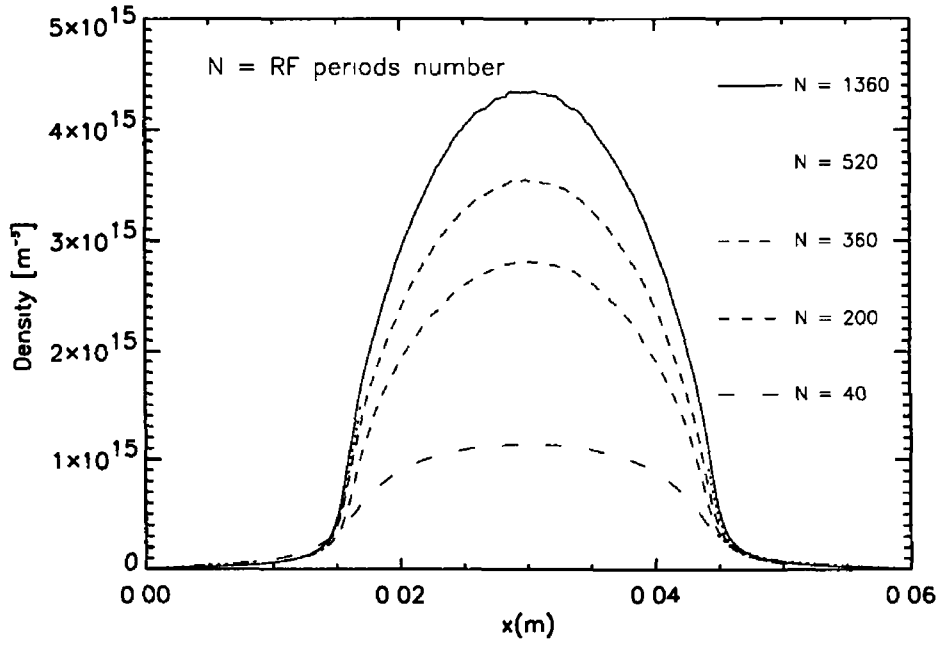

Figure 4 3 Time-averaged electron densities at different times vs space obtained by using only EPIC

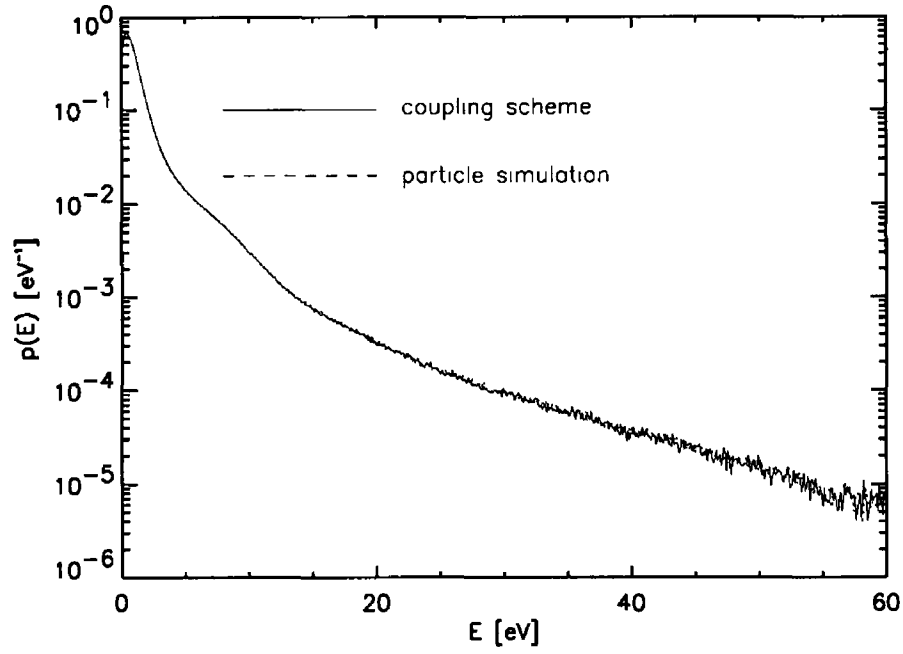

Figure 4 4 EEPF at the steady state obtained with the coupling scheme and by using only EPIC

the coupling scheme the simulated system reaches its steady-state significantly faster than by using only EPIC, with the neutral density values set equal to the values obtained from the coupling scheme The data plotted in figures 4 2- 4 4 also prove that the coupling scheme delivers the same steady-state results that are obtained under the same conditions by using only EPIC

In figure 4 5 the neutral densities used by EPIC at the times when the simulation starts or restarts are plotted versus time In this example 5 different neutral species are included in the model H_2(v=0-2), H and H*(2s) The density of H_2, the dominant neutral species, remains nearly constant from the beginning, while the other ones need a few interactions between EPIC and GMS to reach stable values It has to be noticed that in the PIC the neutral pressure is set by the neutral densities values and by the arbitrarily chosen values of the temperatures, that are assumed constant In GMS the neutral

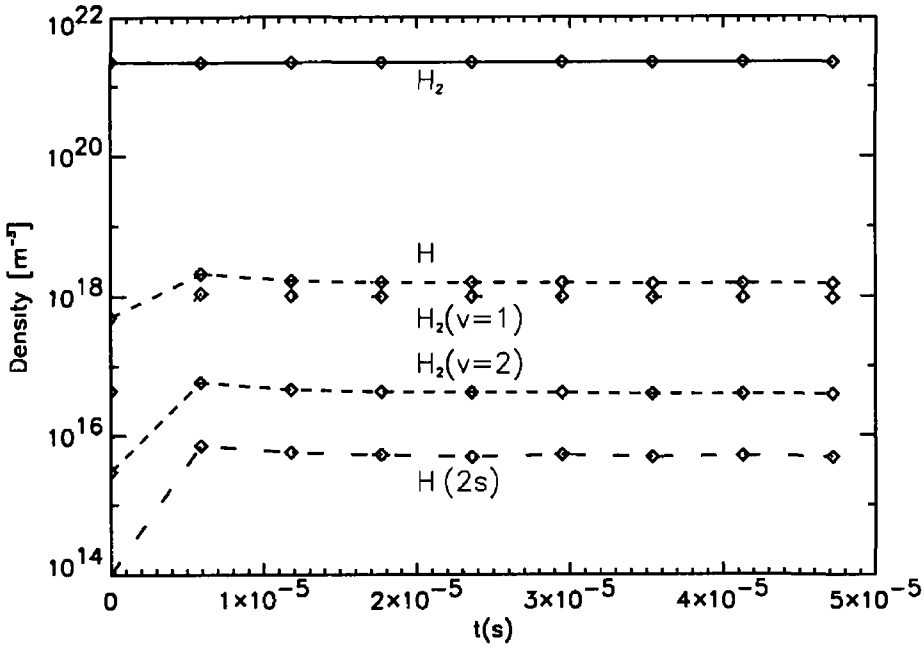

Figure 4 5 Neutral densities vs time

densities are not constants but unknowns, therefore in GMS, as well as in the coupling scheme, the pressure is controlled by the inlet flow rate and the loss terms in the particle balance equations 2 1

4.5 Summary

In this chapter the coupling scheme devised to make particle simulation and global model interact with each other in order to model self-consistently rf plasma discharges with complex chemistry has been explained The changes to be done in GMS to make it interact with the particle simulation code have been explained and the information exchanged by the two models is specified A demonstration of how the scheme works has been given, showing that if the coupling scheme is used the simulated system reaches its steady-state significantly faster than by using only EPIC

Chapter 5

Applications of the coupling scheme

The results obtained from several applications of the coupling scheme, explained in chapter 4 and here used to model rf capacitive H_2 plasma discharges, are presented in this chapter

Firstly, in section 5 1 the scheme is used to study the effects of the inclusion of further collision processes and simulated particle species on some of the physical quantities characterizing an rf capacitively coupled plasma, having the molecular gas H_2 as feedstock gas Secondly, in section 5 2 the average energy needed to create an electron-positive ion pair in the simulated plasma, is calculated at various pressures in the global model by using the non-Maxwellian EEDF obtained from the PIC and a comparison is made with the energies calculated assuming a Maxwellian EEDF instead Thirdly, in section 5 3 a plasma discharge created between two parallel-plate electrodes of the same area and radially confined by a cylindrical quartz is modelled More particularly, the energy distributions of the particles arriving at the grounded electrode of the different positive ion species included in the model are considered Some of

the results are compared with some measurements performed with a two stage differentially pumped Hiden EQP system installed in the Capacitive Radio frequency Ion Source (CIRIS) experiment, below the grounded electrode Lastly, in section 5 4 the coupling scheme is used for modelling the H^- production by DA of H_2(v=0-9) and determine the H^- density in rf capacitive H_2 plasma discharges

5.1 Effect of inclusion of further reactions and simulated species in the plasma model

In this section the effects of the inclusion of further collision processes and simulated particle species at fixed values of the control parameters on the densities, the power deposition and the EEDF in an rf capacitively coupled plasma, having the molecular gas H_2 as feedstock gas, are studied Initially, a very basic model of the plasma will be examined, then made more complex in order to study how some of the physical quantities more important to characterize the discharge are affected by the inclusion in the model of new collision processes and particle species The study is performed with the coupling scheme, described in chapter 4, in a 1D simulation of the discharge in Cartesian geometry with the control parameters having the following constant values the electrode separation is 6 cm, the neutral pressure is approximately 80 mTorr and the power is delivered by a sinusoidal voltage source having peak voltage of 500 V and drive frequency of 13 56 MHz The difference between the various models to be examined are the set of collision processes and in certain cases the simulated species included The collision processes included in the various models considered are listed in table 5 1 Model 1 has the simplest possible reaction set, listed in the set 1 of table 5 1, with only electron ionisation and

Table 5.1: Collision processes included in the models 1-4.

Description	Collision process	Reference
Set 1	$e + H_2 \longrightarrow e + H_2$	[57]
Basic model	$e + H_2 \longrightarrow e + e + H_2^+$	[57]
with e and H_2^+	$H_2^+ + H_2 \longrightarrow H_2 + H_2^+$	[84]
Set 2	$H_2^+ + H_2 \longrightarrow H_3^+ + H$	[85]
H_3^+ processes	$H_3^+ + H_2 \longrightarrow H_3^+ + H_2$	[84]
	$H_3^+ + H_2 \longrightarrow H_2^+(\text{slow}) + H_2 + H;$ (ACT)	[84]
	$H_3^+ + H_2 \longrightarrow H_2^+(\text{fast}) + H_2 + H;$ (CID)	[84]
Set 3	$e + H_2 \longrightarrow e + H_2(J=2)$	[57]
Rotational and	$e + H_2(v) \longrightarrow e + H_2(\ v');\ (v, v'=0\text{-}2;\ v \neq v')$	[57, 58, 59]
vibrational	$e + H_2(v) \longrightarrow e + e + H_2^+;\ (v=1,2)$	[54]
excitations		
Set 4	$e + H_2 \longrightarrow e + H_2^*(b^3\Sigma_u^+) \longrightarrow e + H + H$	[57]
Electronic	$e + H_2 \longrightarrow e + H + H^*(2s)$	[61]
excitations	$e + H_2 \longrightarrow e + H_2^*(a^3\Sigma_g^+ 2s\sigma)$	[57]
and	$e + H_2 \longrightarrow e + H_2^*(B^1\Sigma_u^+ 2p\sigma)$	[61]
H^+ processes	$e + H_2 \longrightarrow e + H_2^*(c^3\Pi_u 2p\pi)$	[86]
	$e + H_2 \longrightarrow e + H_2^*(C^1\Pi_u 2p\pi)$	[57]
	$e + H \rightarrow e + e + H^+$	[57]
	$e + H_2 \rightarrow e + e + H^+ + H$	[61]
	$e + H \rightarrow e + H^*(2s)$	[61]
	$e + H^*(2s) \rightarrow e + e + H^+$	[61]
	$e + H \rightarrow e + H$	[87]
	$H^+ + H_2 \rightarrow H^+ + H_2$	[84]
	$H^+ + H_2 \longrightarrow H^+ + H_2$	[84]
	$H^+ + H_2 \longrightarrow H_2^+ + H$	[84]
	$H_3^+ + H_2 \longrightarrow H^+(\text{slow}) + H_2 + H_2;$ (ACT)	[84]
	$H_3^+ + H_2 \longrightarrow H^+(\text{fast}) + H_2 + H_2;$ (CID)	[84]
	$H^+ + H_2 \longrightarrow H^+ + H_2(J = 2)$	[84]
	$H^+ + H_2 \longrightarrow H^+ + H_2(v = 1\text{-}2)$	[84]
	$H_2^+ + H_2 \longrightarrow H^+ + H + H_2$	[84]

elastic scattering and H_2^+ charge exchange included H_2^+ and e are the only particle species simulated whose time-averaged density versus space is plotted in Figure 5 1(a) Model 1 is very unrealistic In particular the H_2^+ charge exchange reaction cross sections are much lower than the cross sections of the interchange reaction, efficiently converting H_2^+ into H_3^+, and not included in model 1 The dominant ion under these conditions is expected to be H_3^+, so model 2 includes also this ion species and the collision processes listed in the set 2 of table 5 1, including the already mentioned interchange reaction, and other collision processes with H_3^+ as colliding particle Figure 5 1(b) shows the densities of the species included in model 2 H_3^+ has replaced H_2^+ as the dominant positive ion species H_3^+ and electron density behave as expected, their densities drop monotonically moving from the centre of the chamber to either of the electrodes In contrast, the H_2^+ density is flattened in the plasma bulk, because the interchange reaction cross section is very high at energies less than 1 eV, but monotonically decreases very strongly if the energy increases Therefore, slow H_2^+ particles in the plasma bulk are lost more efficiently through this reaction than fast H_2^+ particles already accelerated in the sheath

The ion transport changes significantly, particularly because the H_3^+ collision frequency in model 2 is much higher than the H_2^+ collision frequency in model 1 A rise in the central ion density as well as a steepening of its profile are observed, but in figure 5 2 it can be seen that also the EEDF results significantly affected, because the electrons in model 2 are significantly cooler than in model 1 This may be explained by comparing the time-averaged heating rates, $\mathbf{J}\,\mathbf{E}$, plotted in figure 5 3(a) and (b) in model 1 and 2, respectively, for the electron species The electron heating rate has negative values in the plasma bulk in model 2, while is nearly zero in model 1, therefore electrons are slowed down by the electric field in the plasma bulk in model 2 and that

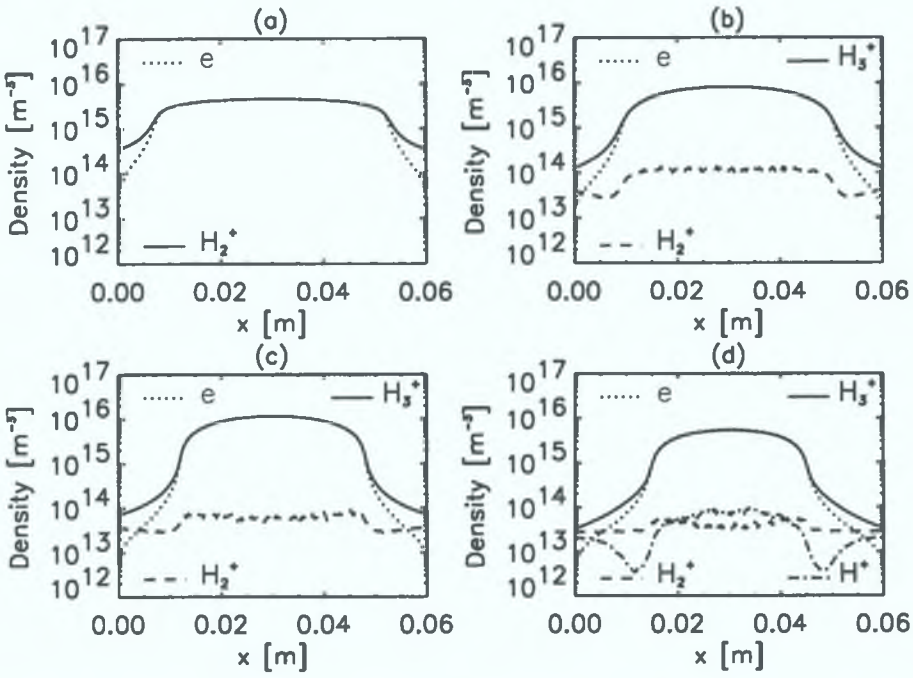

Figure 5.1: Charged particle species time-averaged densities vs. space in the models 1-4.

affects the EEDF. The electron heating rate profiles obtained in all models of this section, with positive maxima in the sheaths and much lower values in the plasma bulk, are typical of a regime where stochastic heating [11][p. 303] is the main heating mechanism in the discharge, as expected for the pressure considered. The positive ion heating rate profiles in figure 5.3, having positive values in the sheath, confirm that positive ions are accelerated by the time-averaged electric field in the sheath.

To obtain model 3, the collision processes listed in set 3 of table 5.1, including rotational and vibrational excitations, are added to the ones included in model 2. Contrary to naive expectation, the central density increases again, with an even steeper profile and larger sheaths evident in figure 5.1(c). But in figure 5.2 it can be seen that a very important effect of the inclusion of these excitation processes is a drastic change of the EEDF from model 2 to model 3. While in model 2 the EEDF is Maxwellian in the energy range considered,

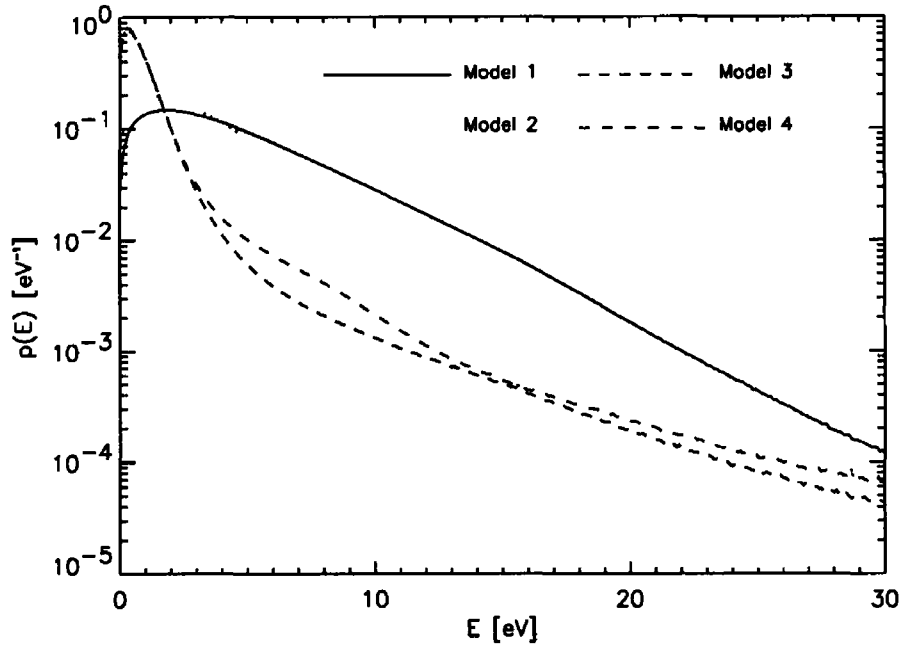

Figure 5 2 Space- and time-averaged EEPFs in the models 1-4

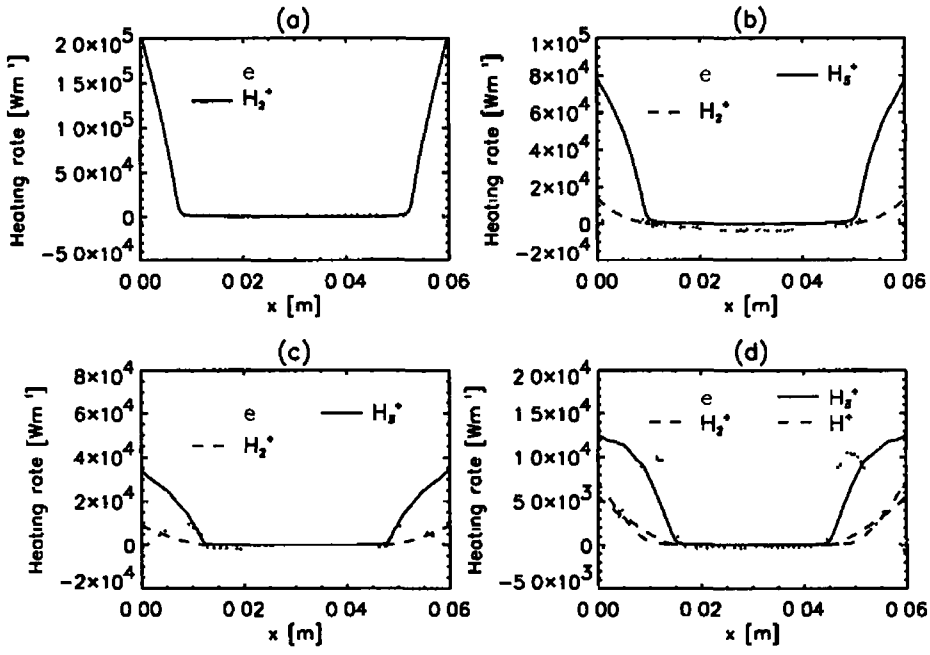

Figure 5 3 Time-averaged heating rate $\mathbf{J} \cdot \mathbf{E}$ vs space of charged particle species in the models 1-4

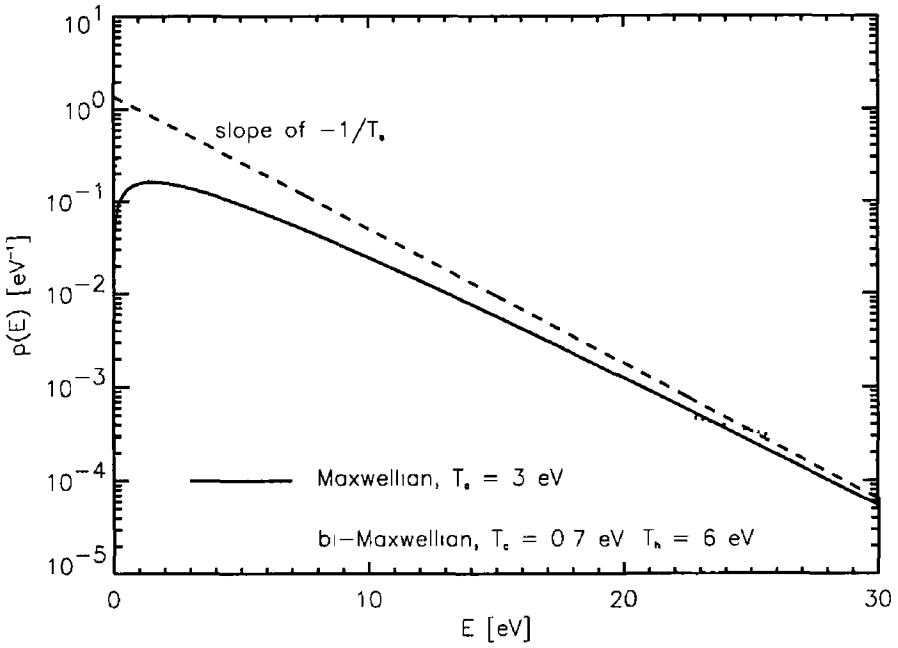

Figure 5.4 Graph of a Maxwellian and a bi-Maxwellian EEPF

adding vibrational and rotational excitations causes the EEDF in model 3 to become bi-Maxwellian. That change is due to the fact that electrons can efficiently lose energy through the processes of set 3, because of their low threshold energy and high cross sections at low energies, so most electrons reach thermal equilibrium at a lower temperature than in model 2, but the remaining fraction reach thermal equilibrium at a higher temperature.

In figure 5.4 a Maxwellian EEPF with $T_e = 3$ eV and of a bi-Maxwellian produced by two particle groups of different population and having different temperature are plotted. The fraction $n_c = 0.9$ of the bi-Maxwellian particles have temperature $T_h = 0.7$ eV, while the particles of the remaining fraction $n_h = 0.1$ have temperature $T_h = 6$ eV. In the units chosen to represent the EEPFs obtained from the simulation, whose plots in semi-logarithmic scale are shown in this thesis, the trend of of a Maxwellian distribution having temperature T_e approaches the trend of a straight line of slope $-\frac{1}{T_e}$ only at

energies higher than a few times T_e That happens because the analytical formula of the EEPF $p(E)$, such as $\int_0^\infty dE\, p(E) = 1$, is

$$p(E) = \frac{2}{\pi^{\frac{1}{2}}} (\frac{1}{T_e})^{\frac{3}{2}} E^{\frac{1}{2}} \exp(-\frac{E}{T_e}) \qquad (5\ 1)$$

and the term $\exp(-\frac{E}{T_e})$ prevails over $E^{\frac{1}{2}}$ only at energies sufficiently high

To obtain model 4, which is a reasonably complete model if H^- is not considered, the electronic excitation processes and other collision processes involving H^+, all listed in set 4 of table 5 1, are added The ion transport has changed significantly once again, with a decrease of the central ion density H^+ density increases by moving from the plasma bulk to the electrodes This happens because H^+ particles are mainly produced through the Collision Induced Dissociation (CID) reaction listed in set 4 of table 5 1 This process has higher cross section values at the energies positive ions are more likely to have in the sheath than in the bulk, therefore a fraction of the H_3^+ particles is converted to H^+ particles and this happens more often in the sheath than in the bulk Although several collision processes have been added to obtain model 4, the EEDF is not strongly affected by that Essentially, the temperature of the electrons at high energy tail of the distribution decreases, as expected, for the inclusion of the inelastic processes of set 4 listed in table 5 1, but the EEDF shape becomes also more complex than a simple bi-Maxwellian

In the analysis performed in this section the effect of the inclusion of various collision processes in the model at certain fixed values of the control parameters in an rf capacitively coupled H_2 plasma discharge, have been considered The inclusion in the model of rotational and vibrational excitations had the biggest effect on the EEDF The inclusion in the model of these energy loss channels virtually changed the EEDF from a Maxwellian to a bi-Maxwellian in the case considered The density profiles of the different positive ion species simulated exhibit significant differences, due to the different mechanisms for

their production and loss and to their different efficiency in the different regions of the discharge In all models the total positive ion density is significantly different, because all the set of processes added to obtain a more complex model contained reactions either increasing the collision frequency of the dominant positive ion species or drastically changing the EEDF and consequently the rates of the ionisation processes, which positive ions are produced through In all models the electron heating rate has two maxima of nearly the same positive values and the rate is positive only in the sheath region, confirming that in these conditions the stochastic heating is the main heating mechanism So apart from the negative values in the plasma bulk of the electron heating rate in models 2 and 3, not present in model 1 and 4, the electron power deposition does not seem to be affected by the inclusion of more collision processes and particle species in the model

5.2 Energy cost of charged particle production

The simplest discharge models are given by the particle balance equation for the positive ion species and the equation of power balance in the discharge [11, p 306-9] Estimates of plasma density and electron temperature averaged in both space and time can be obtained by solving these equations The average collision energy loss of plasma particles in charged particle production, $\mathcal{E}_L$, is an important parameter in models of low pressure capacitive plasmas [11, p 81], because is one of the terms in the power balance equation, as seen in subsection 2 1 2, where is defined in formula 2 11, and in section 4 1 $\mathcal{E}_L$ includes both elastic and inelastic collision energy loss A good estimate of the plasma density requires the inclusion in the model of all the elastic and inelastic collision processes giving a significant contribution to $\mathcal{E}_L$ The averaged electron energy loss for any of these collision processes is given by the

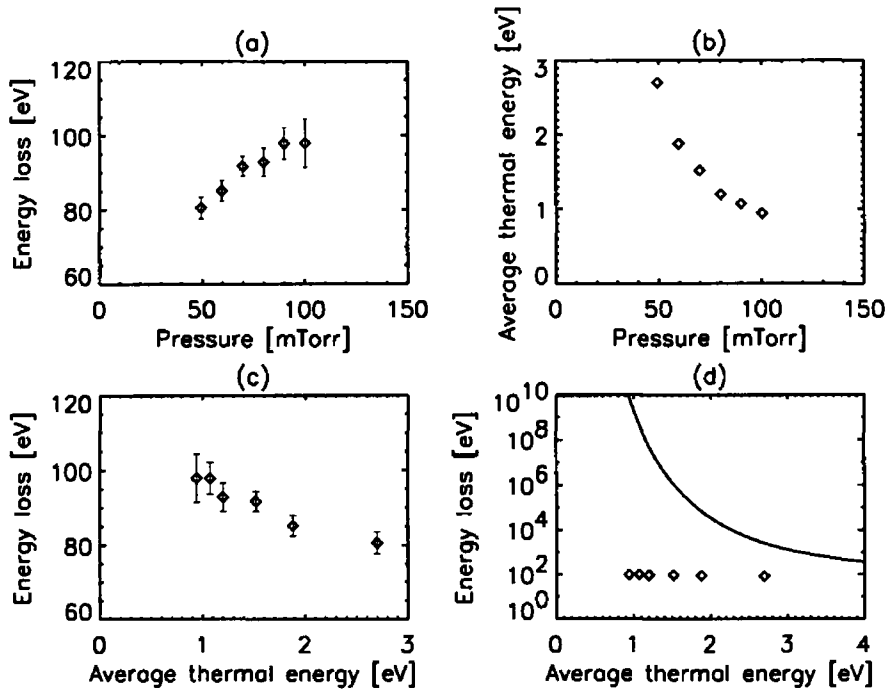

Figure 5 5 (a) $\mathcal{E}_L$ vs pressure, (b) the average electron thermal energy, E_{th}, vs pressure, (c) $\mathcal{E}_L$ vs E_{th} and (d) comparison of $\mathcal{E}_L$ vs E_{th} obtained by using EEDF from PIC simulation and by assuming Maxwellian EEDF having the same value of $E_{th} = \frac{3}{2}T_e$

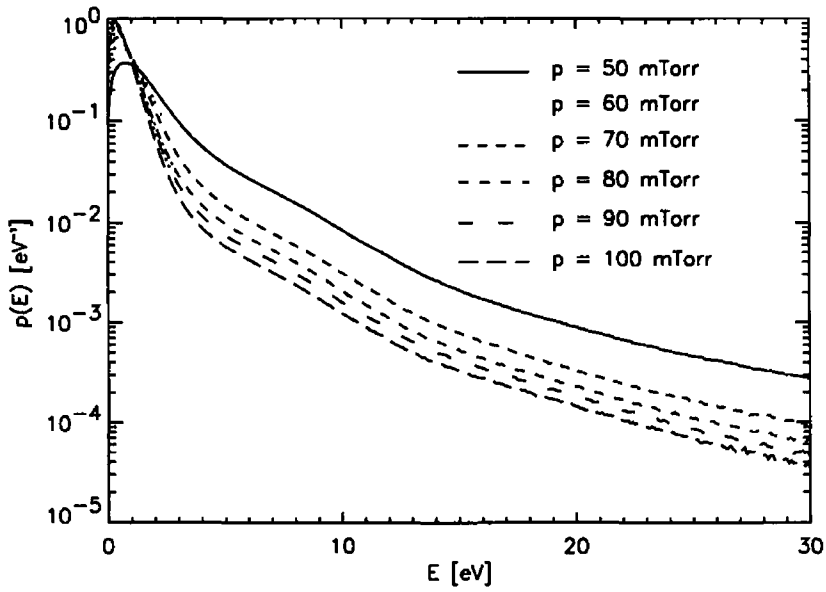

Figure 5 6 Space- and time-averaged EEPFs at different pressures

averaged electron energy loss per collision multiplied by the ratio of its rate constant divided by the ionisation rate constant However, an extra complication arises since the rate constants and therefore the averaged energy loss is sensitive not just to T_e, but also to the electron energy distribution, which is rarely Maxwellian in low pressure, low temperature discharges Departures from thermal distributions are particularly marked in capacitive rf discharges operated at low pressure Measurements reveal [88] regimes with concave bi-Maxwellian or convex Druyvesteyn-like distributions, that have been replicated by using PIC simulations [89] In this section, the importance of the effect on the calculation of $\mathcal{E}_L$ of the assumption of Maxwellian EEDF in capacitive rf discharges is investigated The values of $\mathcal{E}_L$ obtained in 1D simulation of rf capacitively coupled H_2 plasma discharges under certain operating conditions, by using the coupling scheme explained in chapter 4, are compared with the values obtained instead by assuming Maxwellian EEDFs having the same average thermal energy

In the simulation the plasma is driven by a sinusoidal voltage source having peak voltage of 500 V and frequency 13 56 MHz The distance between the electrodes is 6 cm, and the neutral pressure varies between 50 and 100 mTorr The mathematical mesh on the spatial domain of the simulation has 301 points The collision processes included in the model are all those listed in table 5 1 $\mathcal{E}_L$ in the discharge, where H_3^+ is the dominant ion species, is well approximated by $\mathcal{E}_{L,H_2^+}$, as mentioned in subsection 2 3 1 $\mathcal{E}_{L,H_2^+}$ is calculated by using formula 2 11, used by the global model, with all rate constants either obtained directly from the simulation or by averaging the product of cross section and electron velocity over the space- and time-averaged EEPF obtained from the simulation

In figure 5 5(a) the values of the energy loss obtained at different pressures

are plotted versus the pressure The error bars, which in most cases do not correspond to a high percentage error, are present because of the different results obtained by the global model for $\mathcal{E}_{L,H_2^+}$ at different microscopic states of the simulation, but all at the steady-state In figure 5 5(b) the average electron thermal energies E_{th} obtained at different pressures are plotted versus the pressure By increasing the pressure, E_{th} decreases because the electrons are more likely to lose energy through collisions, while $\mathcal{E}_{L,H_2^+}$ increases because the ratio of elastic and inelastic process to ionisation rate constants is expected to increase and so does the contribution to $\mathcal{E}_{L,H_2^+}$ of the elastic and inelastic collision processes This is due to the fact that the ionisation threshold energy is significantly higher than the threshold energy of the other inelastic collision processes

The data of figure 5 5(a)-(b) are plotted again in figure 5 5(c)-(d) to show $\mathcal{E}_{L,H_2^+}$ versus E_{th} Besides, in figure 5 5(d) the same results are compared with the values of $\mathcal{E}_{L,H_2^+}$ obtained from the same set of collision processes used in the simulation, assuming a Maxwellian EEDF instead, and plotted as a function of E_{th}, that for a Maxwellian velocity distribution in three dimensions is equal to $\frac{3}{2}T_e$, with T_e being the electron temperature The difference between the values of $\mathcal{E}_{L,H_2^+}$ calculated by using the EEDF obtained self-consistently from the simulation and the values calculated by using a Maxwellian EEDF and plotted in figure 5 5(d) with a continuous line, is enormous The reason of this difference can be seen in figure 5 6, where the space- and time-averaged EEPFs obtained from the simulation are plotted They are all clearly very much different from Maxwellian distributions and the rate constants of the collision processes of interest in the calculation of $\mathcal{E}_{L,H_2^+}$ by formula 2 11, is affected by that In particular, the ionisation rate constant is much higher with these EEPFs than with EEPFs calculated with Maxwellian distributions

having the same average thermal energy, because with the former distributions the percentage of electrons able to deliver enough energy to produce ionisation is much higher than in the latter ones.

In this section we have shown that the assumption of Maxwellian EEDF in the calculation of $\mathcal{E}_L$ in cases where the EEDF obtained self-consistently in the simulation is clearly non-Maxwellian, as in 1D simulations of rf capacitively coupled H_2 plasma discharge at low-pressure, strongly affects the result, that can differ very much from the real value of $\mathcal{E}_L$, calculated by using the EEDF obtained without making any assumption.

5.3 Ion energy distributions

In processing plasmas the energy distribution of the positive ions arriving at the discharge boundary is an important factor in the effectiveness of processes such as plasma enhanced deposition and etching. Before hitting the surface of the chamber confining the plasma discharge, positive ions are accelerated in the sheath, the positively charged region that forms between the plasma and the chamber wall. In rf plasmas the rf sheath dynamics, the rf modulation of the sheath potential and collisions in the sheath can affect significantly the Ion Energy Distribution (IED) of particles hitting the surface of the chamber wall. To study these effects, approximate analytical models, Monte Carlo and PIC simulations were developed. A review of this topic is given in [90].

In this section the coupling scheme explained in chapter 4 is used to model a capacitively coupled rf hydrogen plasma discharge created in the Capacitive Radio frequency Ion Source (CIRIS) experiment; particular emphasis is put on the IEDs of the three positive ion species included in the model. Results are compared with measurements of the IEDs performed by Deborah O'Connell in the experiment with a Hiden EQP system. This work was presented in [91],

although the results presented here are slightly different because of changes made to improve the modelling after [91] was submitted.

5.3.1 The CIRIS experiment

In the CIRIS experiment a capacitively coupled rf hydrogen plasma discharge is created between two parallel-plate electrodes of equal area of diameter 140 mm and separated by a 50 mm gap. One of the electrodes is driven by an external rf power source while the other one is grounded. The discharge is radially confined between the electrodes by a cylindrical quartz tube, that both shields the discharge from the chamber walls and creates a pressure differential between the inside and the outside of the tube. Gas is introduced into the chamber through a shower-head arrangement in the grounded electrode. A circular orifice having 100 μm radius at the centre of the grounded electrode allows for the sampling of particles impinging on its surface. To measure the energy distribution of the particles arriving at the electrode for the different ion species present in the discharge, a two stage differentially pumped Hiden EQP is installed. This system is composed of an electrostatic ion energy analyser and a quadrupole mass spectrometer.

5.3.2 Numerical model and its results

To model this system a 2D bounded electrostatic PIC/MC simulation in cylindrical geometry (r,z), coupled with a global model as previously described, was used. The electric potential in the mesh points of the boundary occupied by the quartz is calculated by linear interpolation of the electric potential between driven and grounded electrode. The simulated species are electrons and the three positive ions H^+, H_2^+ and H_3^+. The background neutral species included are H_2(v=0-2), H and H^*(2s). The collision processes included in the simula-

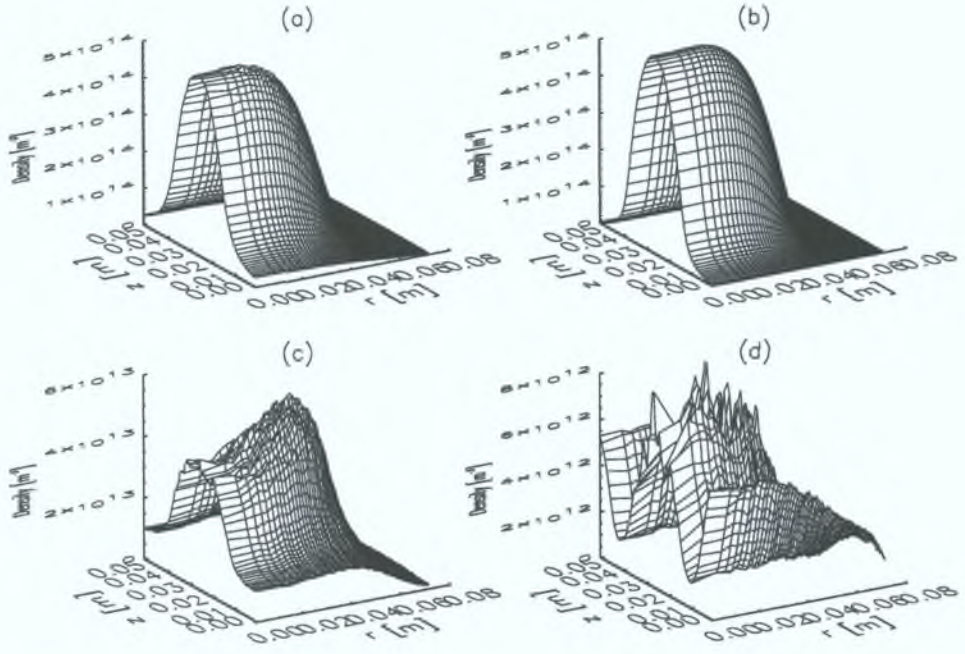

Figure 5.7: Time-averaged density vs. position (r,z) of (a) H_3^+, (b) e, (c) H_2^+ and (d) H^+; p = 49 mTorr, f = 13.56 MHz.

tion are those listed in table 5.1. All numerical results presented in this section are obtained by setting a peak voltage of 200 Volt for the external rf power source in both the experiment and the simulation.

Figure 5.7 shows the density profiles of the electron species and of the positive ions included in the model obtained at p = 49 mTorr and f = 13.56 MHz. In these graphs the x-axis is associated to r, the radial coordinate, while the y-axis is associated to z, the axial coordinate. The latter axis is actually the symmetry axis of the cylindrical chamber. H_3^+ is the dominant positive ion species. On the symmetry axis of the chamber, $r = 0$, H_3^+ and electron density behave as expected; moving from the centre of the chamber to either of the electrodes, $z = 0$ and $z = 0.05$, those densities drop monotonically. In contrast, the H_2^+ density is flattened in the plasma bulk, while H^+ density increases when moving from the plasma bulk to the electrodes. The density

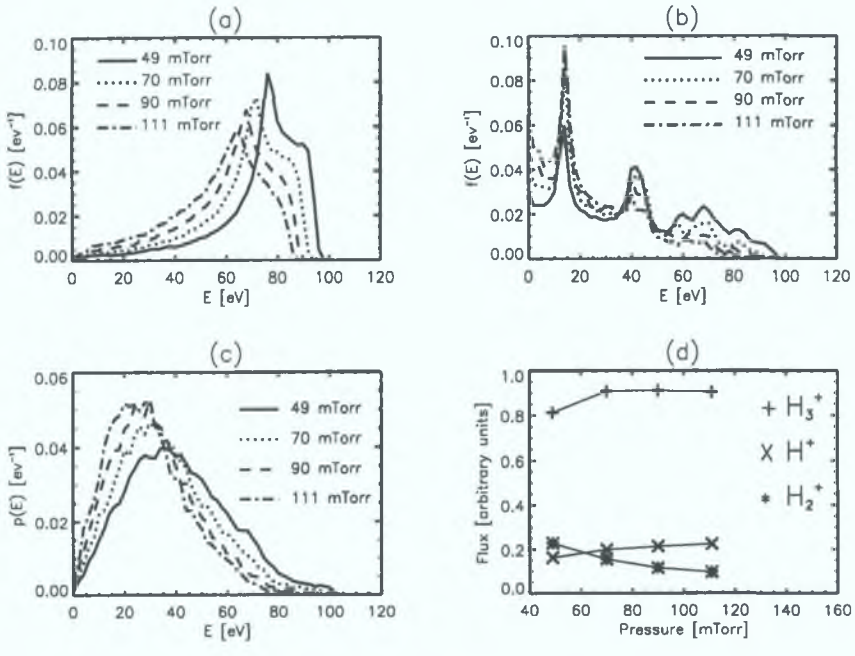

Figure 5.8: Normalized energy distributions of particles arriving at the central region of the grounded electrode at different pressures for (a) H_3^+, (b) H_2^+ , (c) H^+ species and (d) flux vs. pressure for the same species; f = 13.56 MHz.

profiles on the symmetry axis of the chamber are qualitatively the same obtained in 1D simulations in section 5.1 and shown in figure 5.1(d). The collision processes affecting most the density profiles of the simulated species are the same previously discussed in section 5.1.

In rf collisionless sheaths the ratio $\beta = \tau_{ion}/\tau_{rf}$ of the ion transit time in the rf sheath, τ_{ion}, to the rf period, τ_{rf}, is a crucial parameter in determining the shape of the IED [90]. If the ion transit time is a small fraction of the rf period ($\beta \ll 1$), the sheath ion dynamics is in a low-frequency regime and the ions respond to the instantaneous sheath voltage. The resultant IEDF has a double peak structure, with the energy centred between the two peaks being the time-averaged sheath voltage. The higher energy peak is produced by ions entering the sheath when the sheath voltage is near its maximum value during

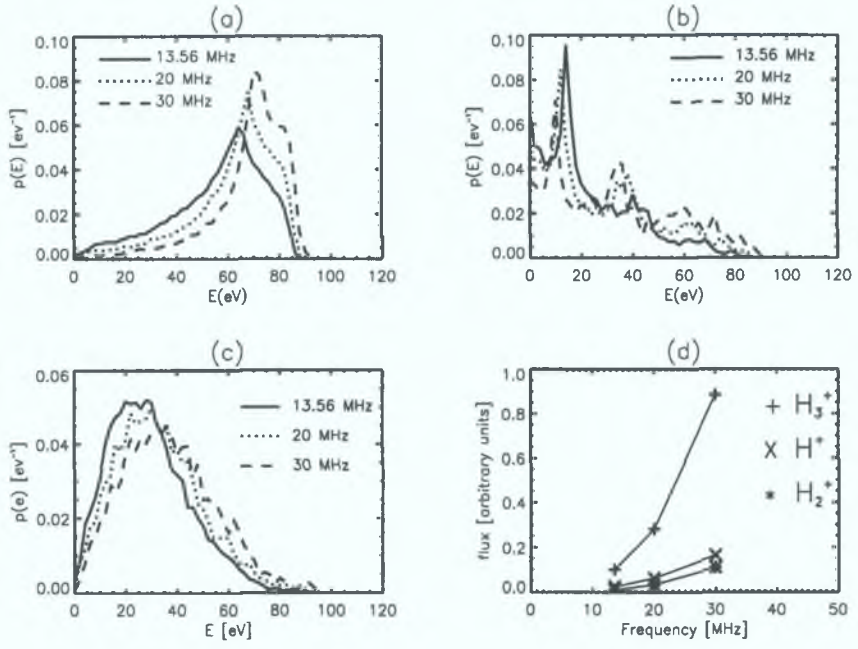

Figure 5.9: Normalized energy distributions of particles arriving at the central region of the grounded electrode at different frequencies at p = 111 mTorr for (a) H_3^+, (b) H_2^+, (c) H^+ species and (d) flux vs. frequency for the same species.

the rf cycle, while the lower energy peak is produced by ions entering the sheath when the sheath voltage is near its minimum value in the rf cycle. In the high frequency regime ($\beta \gg 1$) the ions respond only to the time-averaged sheath voltage, because they need many rf periods to cross the sheath. This makes the two peaks approach each other and if the value of β is high enough they will merge to form a single peak at the time-averaged sheath potential.

The flux of particles arriving at the grounded electrode and the distributions of their energy when they hit the grounded electrode were obtained for each positive ion species simulated. These distributions were obtained for several values of pressure at the driving frequency f = 13.56 MHz. After normalisation, these results are plotted in figure 5.8. All numerical results presented in this section are obtained by sampling only the positive ions hit-

ting the electrode on its central region ($0 < r < 0.035$). In the experiment the collection area in the centre of the grounded electrode is much smaller. But if the same region had been chosen in the simulation it would have taken a much longer computational time to obtain an acceptable sampling of the distributions, especially for the minority species H^+ and H_2^+.

The H_3^+ distributions in figure 5.8(a) have a shape similar to the saddle-shape expected for the low-frequency regime, although the second peak is missing. The remaining low-energy peak is placed at a value of the energy distinctly less than the average sheath potential, as expected. By increasing the pressure the average energy of the particles decreases, due to the decreasing average sheath potential. Moreover, the low energy tail becomes more pronounced. The H_2^+ distributions in figure 5.8(b) have very pronounced peaks at energies much lower than the time-averaged sheath potential. These are produced by H_2^+ charge exchange reaction in the sheath. This process efficiently converts fast H_2^+ into slow H_2^+. The dependence of the energy, of positive ions hitting the electrode, on the position where particles enters the oscillating rf sheath and on the sheath oscillation phase when this happens determines the position of the peaks [92]. The H^+ distributions shown in figure 5.8(c) have a single maximum at energies below 40 eV, indicating that H^+ particles are mainly created in the sheath. Figure 5.8(d) shows the ion fluxes at different pressures at the central region of the grounded electrode. The total flux in this region, being the sum of the 3 fluxes plotted, does not vary very much with increasing pressure. H_3^+ is the main component of the flux. H_2^+ flux significantly decreases with increasing pressure and H^+ flux increases. This is due to the higher efficiency of the interchange reaction converting H_2^+ into H_3^+ and of the CID process converting H_3^+ into H^+.

The flux of particles arriving at the grounded electrode and the distribu-

tions of their energy when they hit the grounded electrode were obtained for each positive ion species simulated. These distributions were obtained for several values of the driving frequency at a pressure of p = 111 mTorr. After normalisation, these results are plotted in figure 5.9(a)-(c). By increasing the frequency the time-averaged sheath potential remains around 80 eV. The H_3^+ distributions shown in figure 5.9(a) have a low energy peak as the ones in figure 5.8(a). This peak is distinctly below the time-averaged sheath potential. The distributions become narrower by increasing the frequency, due to the consequent increase in the value of β. The distributions of H_2^+ are plotted in figure 5.9(b). The secondary peak near 40 eV becomes more pronounced by increasing the frequency and generally the value of the distribution near the average sheath potential increases. The H^+ distributions in figure 5.9(c) have a single maximum at energies below 40 eV. This indicates once again that H^+ particles are efficiently produced in the sheath. The fluxes plotted in figure 5.9(d) show that for all positive ion species the flux increases with increasing frequency, due to the increasing plasma density, and the H_3^+ component of the total flux is the most important at all chosen frequencies.

5.3.3 Comparison with experimental measurements

In figure 5.10 IEDs measured experimentally in an rf capacitively coupled H_2 discharge at V = 200 Volt, p = 111 mTorr and f = 13.56 MHz are compared with the IEDs obtained from the numerical model at the same operating conditions. The H_3^+ distributions shown in figure 5.10(a) are very similar at higher energies. The low energy peaks are positioned nearly at the same energy. The difference at lower energies may be explained by the different particle sampling in the simulation and in the experiment. In the simulation all particles hitting the chosen sampling area give their contribution to the distribution,

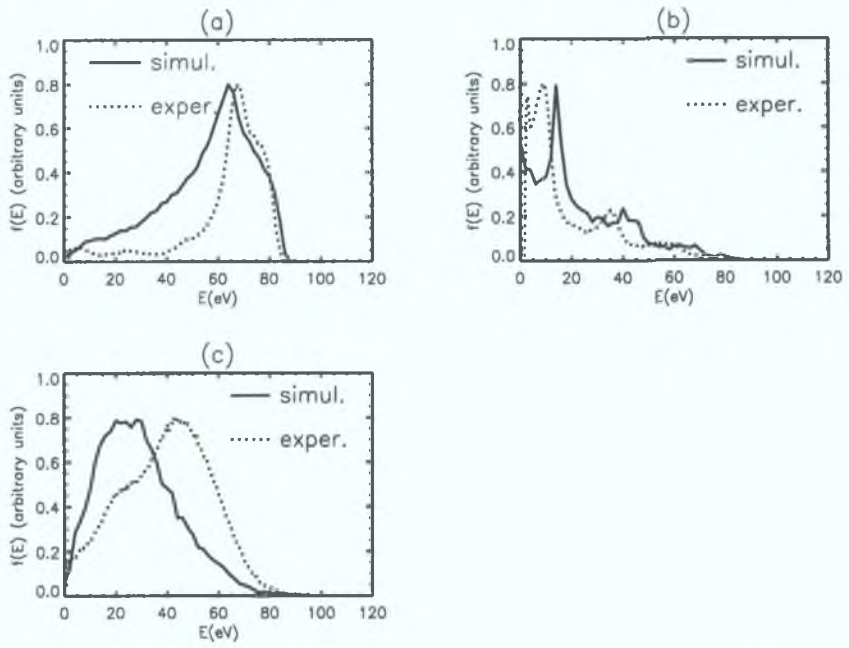

Figure 5.10: Energy distributions of particles of the species (a) H_3^+, (b) H_2^+ and (c) H^+ arriving at the central region of the grounded electrode and their experimental measurements at p = 111 mTorr, V = 200 Volt and f = 13.56 MHz.

while the experiment has a limiting acceptance angle. Therefore H_3^+ particles deflected by collisions in the sheath may hit the electrode with a large velocity component parallel to the electrode relative to the perpendicular component. Such particles can not be sampled in the experiment, but in the simulation the particles are sampled regardless of their colliding angle. In figure 5.10(b) both H_2^+ distributions have the same structure over the entire energy range, except for energies less than 10 eV. However in the experiment the peaks are positioned at lower energies than in the simulation. In figure 5.10(c) the two H^+ distributions do not look as similar as the H_3^+ and the H_2^+ distributions where the distance between the corresponding peaks is just a few eV. In fact, in this case the peak distance is about 20 eV.

5.3.4 Conclusions

In this section a capacitively coupled rf hydrogen plasma discharge created in the CIRIS experiment was modelled with the coupling scheme explained in chapter 4. Particular emphasis was put on the IEDs of the particles arriving at the central area of the grounded electrode. Collisions in the sheath produce the tail in the H_3^+ energy distributions between zero energy and the low energy peak, but a very significant fraction of the H_3^+ particles sampled have an energy not too different from the average sheath potential. In contrast H_2^+ energy distributions are more strongly affected by charge-exchange collisions in the sheath, presenting pronounced secondary peaks at energies significantly less than the time-averaged sheath voltage. H^+ ions are mainly produced in the sheath and their IED peaks at energies always less than half the time-averaged sheath voltage. H_3^+ gives the main contribution to the ion flux on the central region of the grounded electrode. The IEDs measured in the experiment with a Hiden EQP system are compared with the numerical results obtained and a reasonably good agreement has been found for the H_3^+ and H_2^+ ions.

5.4 Inclusion of H^- in the model

In this section H^- particle species is included in the model of rf capacitively coupled H_2 plasma discharges and H^- production by DA of $H_2(0 \leq v \leq 9)$ is modelled self-consistently by using the coupling scheme described in chapter 4. This is the last application of the coupling scheme presented in this chapter and is the one that gave the main motivation to devise and implement the coupling scheme presented in this thesis.

The first part of this section is the natural continuation of the work presented in section 5.1. The collision processes listed in table 5.2 are added to

Table 5.2: Collision processes to be added in the model to include H^- .

Description	Collision process	Reference
Set 5	$e + H_2(v) \longrightarrow e + H_2(v+1)$; (v = 2-3)	[59]
$H_2(v)$ processes	$e + H_2(v+1) \longrightarrow e + H_2(v)$; (v = 2-3)	[59]
(v = 3-9)	$e + H_2 \longrightarrow e + H_2(v = 3\text{-}6)$; e-V	[57, 68]
	$e + H_2(v = 3\text{-}6) \longrightarrow e + H_2$	[57, 68]
	$e + H_2(v = 3\text{-}4) \longrightarrow e + e + H_2^+$	[54]
	$e + H_2 \rightarrow e + H_2^* \rightarrow e + H_2(v = 0\text{-}9) + h\nu$; E-V	[60]
Set 6	$e + H_2(v = 0\text{-}9) \longrightarrow e + H^-$	[93]
H^- processes	$H^- + H_2 \longrightarrow H^- + H_2$	[85]
	$H^- + H \longrightarrow e + H_2$	[61]

the ones listed in table 5.1 to include H^- in the model. The simulation results are obtained under the same operating conditions specified in section 5.1. The H^- production by DA of $H_2(0 \leq v \leq 9)$ can be modelled only if $H_2(0 \leq v \leq 9)$ species are included in the simulation as background species in collisions. In the coupling scheme their density is calculated by the global model, that then delivers the results to the PIC/MC simulation.

Before including H^- in the model, $H_2(3 \leq v \leq 9)$ species are included to obtain model 5 by adding the collision processes in set 5 of table 5.2 to the ones listed in table 5.1. In fact, the cross section data used for the E-V processes, previously explained in subsection 2.4.2, producing $H_2(v)$, are obtained for electronic excitation of H_2 via its B and C singlet states. Therefore the electronic excitations to those states in set 4 of table 5.1 have to be removed from model 5 and following, because already considered in the E-V processes of set 5. The other reactions in set 5 were already included in the global model of section 2.4. The collision processes to be added to the processes included

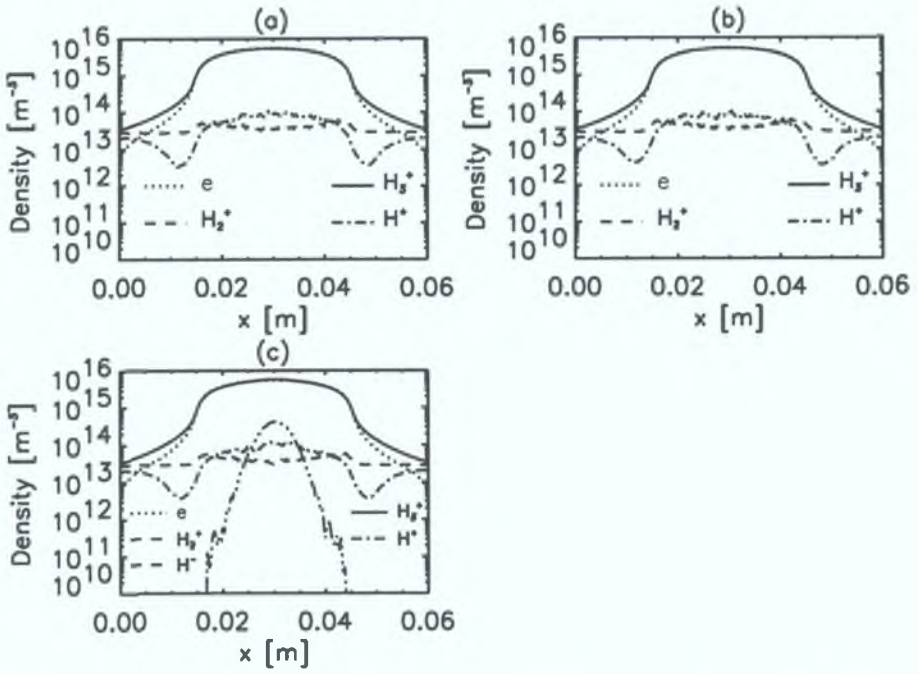

Figure 5.11: Charged particle species time-averaged densities vs. space in the models 4-6.

in model 5 to obtain model 6 are listed in set 6 of table 5.2. They are DA of $H_2(0 \leq v \leq 9)$, H^- elastic scattering and H^- associative detachment (AD). Other important collision processes involving H^-, such as electron detachment and mutual neutralisation with positive ions, that were included in the global model of section 2.4, can not be included here. The reason is that EPIC can not handle collision processes between two superparticles at this stage. Therefore the H^- density is overestimated in this model, because H^- particles can be lost through all these missing processes. But that does not prevent to model properly the H^- production through DA.

In figures 5.11- 5.13 the time-averaged densities of the simulated species, the EEPFs and the heating rates in models 4, 5 and 6 are plotted. In figure 5.11(c) the H^- density obtained in model 6 is plotted, which has a pronounced peak in the center of the discharge, but its maximum is about one order of magnitude less than the maximum of the electron density. As expected, negative ions,

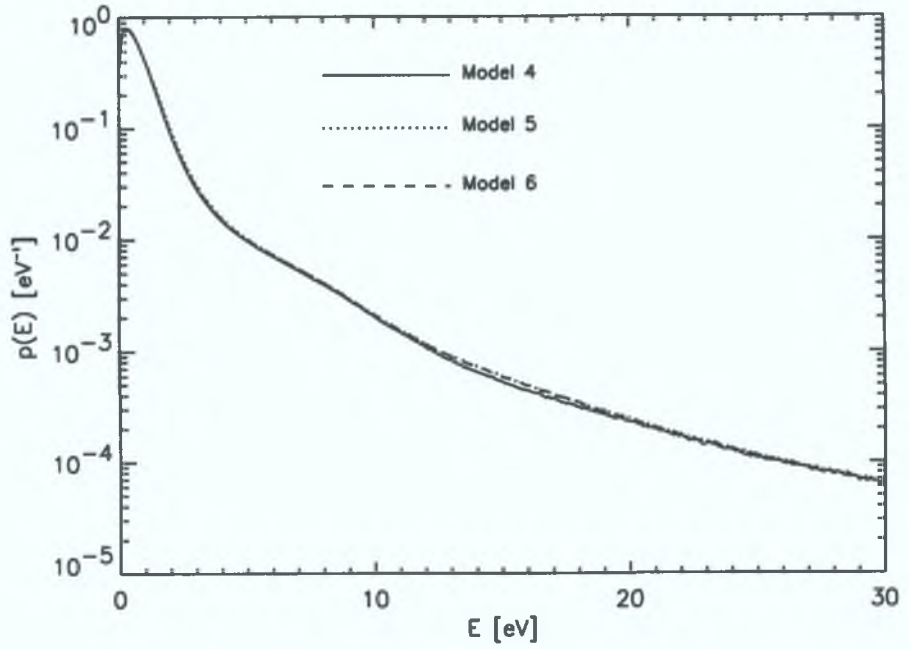

Figure 5.12: Space- and time-averaged EEPFs in the models 4-6.

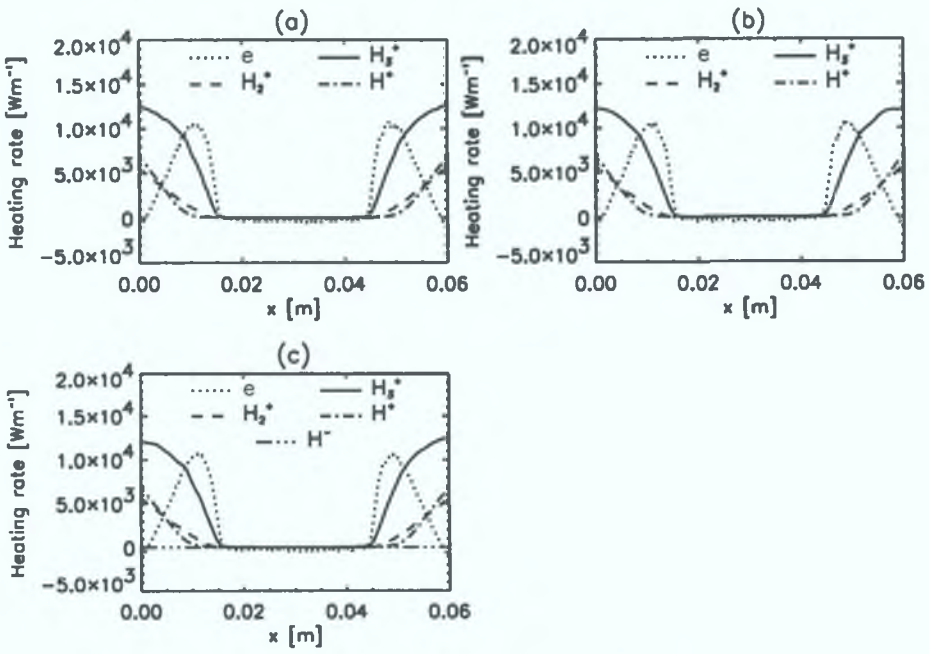

Figure 5.13: Time-averaged heating rate $\mathbf{J} \cdot \mathbf{E}$ vs. space of charged particle species in the models 4-6.

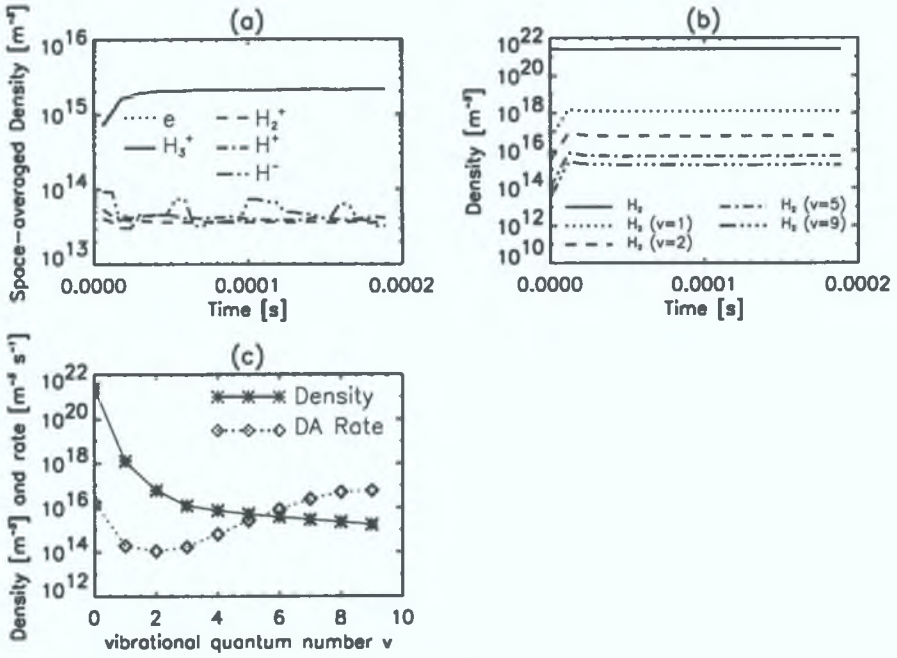

Figure 5.14: (a) charged particle species densities and (b) H_2(v =0-2,5,9) densities vs. time; (c) H_2(v=0-9) density and DA rate vs. vibrational quantum number v.

being much heavier than electrons, are well confined in the central region of the discharge by the time-averaged electric field in the sheath pointing towards the electrodes. Moreover, figure 5.13(c) shows that the H^- heating rate is nearly zero in the whole spatial domain. To finish the analysis started in section 5.1, we conclude that the inclusion in the model of H^- particle species and of the collision processes in table 5.2, does not produce any dramatic change in any of the other quantities plotted in figures 5.11- 5.13 and therefore in the behaviour of the plasma discharge.

In figure 5.14(a)-(b) the time evolution of the charged particle species space-averaged densities and of the H_2(v =0-2,5,9) densities are plotted. While the neutral densities calculated by the global model reach stable values, the H^- density keeps on oscillating significantly. This problem is caused by the fact that AD is the only H^- loss collision process that can be included in the

model at this stage. The DA rate constant used in the H^- particle balance equation of the global model can be calculated only from its number of collision events in the simulation affecting H^- superparticles. If this number is too low, the statistical error caused in the calculation of its rate constant will become too high. In turn, the statistical error in the AD rate constant used in the H^- particle balance equation of the global model produces a statistical error on the H^- density calculated by the global model and thus the oscillations of the H^- density, as seen in figure 5.14(a). However, this problem can be simply solved by obtaining a higher number of collision events to calculate the AD rate constant in the simulation. To achieve that, the sampling time or the number of superparticles used in the simulation has to be increased. Of course, only the inclusion of the missing H^- loss processes may suffice, particularly if some of the missing processes has a significantly higher rate constant than AD, because the total number of H^- loss collision events would then significantly increase.

In figure 5.14(c) the H_2(v =0-9) densities and H^- production rate by DA versus the vibrational quantum number v are plotted. Although the densities of the vibrationally excited states of H_2 are much less than the H_2 density, the contribution of the highest considered vibrational levels of H_2 to the H^- production by DA is even higher than the contribution of H_2. This is caused by the dramatic increase of the maximum of the DA cross section and by the decrease of its threshold energy if the value of v increases. The H density at the steady state, necessary to calculate the AD rate, results 1.76×10^{18} m^{-3}.

Unlike the AD rate constant, the DA rate constants are not affected by any significant statistical error because they are calculated by using the formula 4.4, where the EEPF obtained from the simulation is used to perform the average, not by using the number of collision events happened in the simulation. That

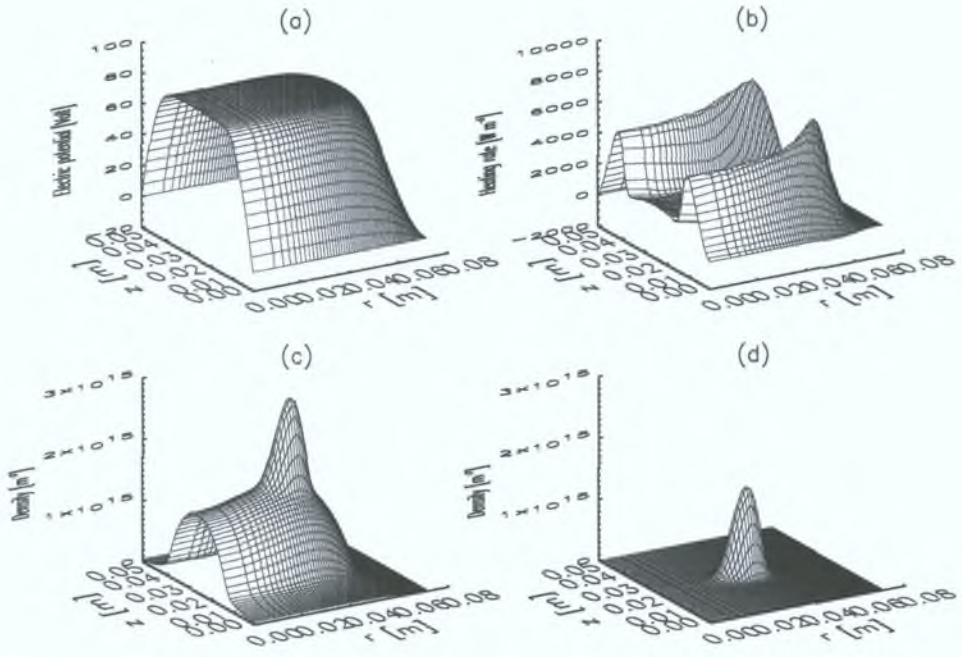

Figure 5.15: Time-averaged (a) electric potential, (b) electron heating rate $\mathbf{J} \cdot \mathbf{E}$, (c) H_3^+ density and (d) H^- density vs. space (r, z).

allows to accelerate enormously the convergence of the time-averaged H^- density towards its value at the steady state, overcoming the problem of its total production rate being much less than the electron and positive ion production rates. If the coupling scheme was not used and the initial H^- density in the simulation was very much different than the H^- density at the steady state, then it would take a much longer time for the H^- density to reach a stable value in the simulation.

A similar study is now performed with 2D simulations of rf capacitively coupled H_2 plasma discharges in cylindrical geometry. We start considering the results of a simulation of a plasma discharge produced in CIRIS with the control parameter values chosen in subsection 5.3.3, but with the inclusion of the collision processes of model 6. In figure 5.15(a) the time-averaged electric potential and in figure 5.15(b) the time-averaged electron heating rate are

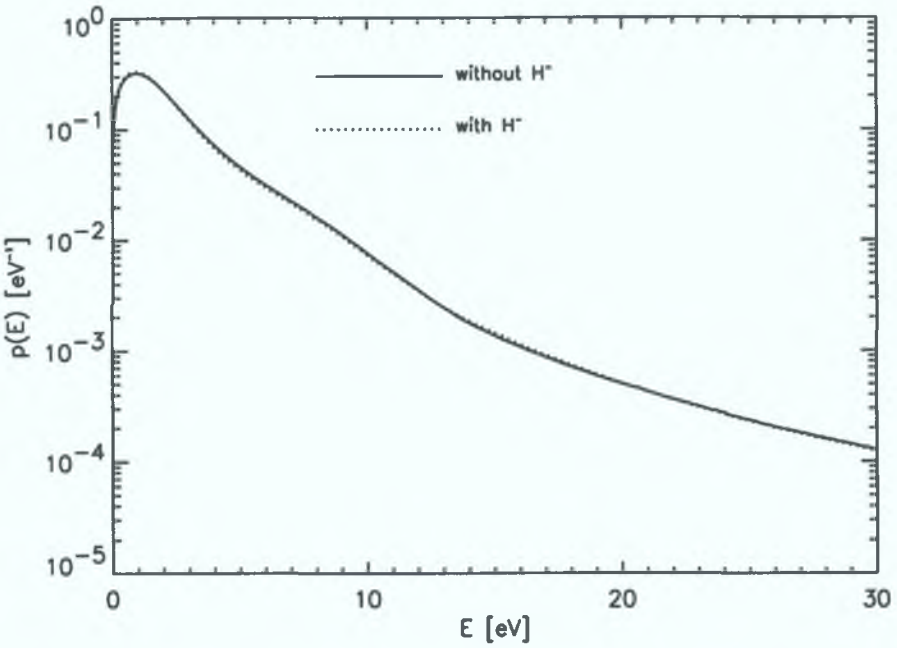

Figure 5.16: Space- and time-averaged EEPFs.

plotted. Sections of the heating rate surface at a constant value of r and not too close to the radial boundary have a similar trend to the same quantity plotted in 1D in figures 5.13(a)-(c). In figure 5.15(c)-(d) the time-averaged H_3^+ and H^- density are shown respectively. The H^- particles are confined in a region halfway between the two electrodes, but not centred in the cylindrical axis of the chamber. Moreover the fraction of the spatial domain occupied by H^- is much less than it was in 1D, see also figure 5.13(c) for comparison. Consequently the maximum of the H^- density becomes of the same order of magnitude of the maximum of the density of H_3^+, the dominant positive ion species. We can see that the H_3^+ density has a pronounced peak in the region occupied by H^-, to satisfy the charge quasi-neutrality in that region of the plasma bulk.

In figure 5.16 the time averaged EEPFs of the 2D model considered in subsection 5.3.3, without H^-, and of the 2D model considered in this section,

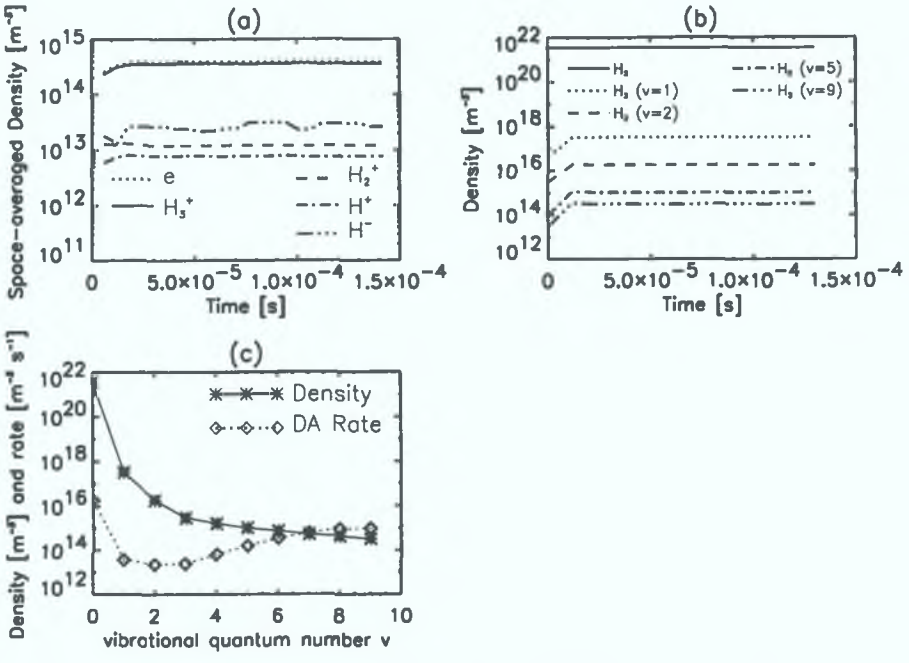

Figure 5.17: (a) charged particle species densities and (b) H_2(v =0-2,5,9) densities vs. time; (c) H_2(v=0-9) density and DA rate vs. vibrational quantum number v.

with H^-, are compared. They are nearly the same, as the EEPFs of the 1D models compared in figure 5.12 are. But we note that the EEPFs of the 2D model obtained at 111 mTorr is more similar to the EEPF of the 1D model obtained at 50 mTorr than to the ones at higher pressure, all shown in figure 5.6. At around the same pressure of 111 mTorr the EEPFs in the 1D and in the 2D model are significantly different.

In figure 5.17(a)-(b) the time evolution of the charged particle species space-averaged densities and of the H_2(v =0-2,5,9) densities are plotted. It has to be noticed that this time the H^- density oscillation is not as pronounced as the one in the 1D model, because of the better statistics of the AD collision events obtained, although the lower H density, 3.77×10^{17} m^{-3}, obtained at the steady state. The better statistics is mainly due to the higher number of superparticles that has to be necessarily used in 2D simulations. The average

electron density is much less than in the 1D model and this causes a much lower population of the vibrationally excited levels of H_2 than in the 1D case, as can be seen by comparing the graphs in figures 5 14 and 5 17 Moreover, it can be seen also that the total DA rate in the 2D model is much less than in the 1D model That is partially caused by the average electron and $H_2(v)$ densities obtained in the 2D model being lower than those obtained in the 1D model, but another important reason of that is the different shape of the EEPFs obtained in the two models considered The DA cross sections are zero below the threshold energy, which is about 3 7 eV for the ground state and less than 1 eV for $H_2(v > 6)$, have a maximum near that energy and the cross section decreases fast if the energy increases Because of such energy dependence of the DA cross sections, it is clear that the electron energy distribution of the 1D model in figure 5 12 is much more effective in producing H^- through DA of the highest considered vibrational levels of H_2 than the distribution of the 2D model in figure 5 12 This is confirmed by the DA rate plots in figures 5 14(c) and 5 17(c) In the 1D model the level v=9 gives the highest rate, while in the 2D model the ground-state level of H_2 gives the highest rate In this case the distribution having the lowest average thermal energy gives the highest total H^- production rate through DA of $H_2(v)$

In figures 5 18 and 5 19 the time-averaged H^- density at the steady state for several 2D numerical models in cylindrical geometry is shown for different values of d, the distance between the electrodes, and of r, their radius, with the control parameter values chosen in subsection 5 3 3 We note that the position of the maximum of the H^- density depends on the dimensions of the cylindrical chamber In figure 5 18 it can be noticed that by making r shorter, the maximum approaches more and more the cylindrical axis and the centre of the chamber In figure 5 19 it can be seen that by making d shorter, the

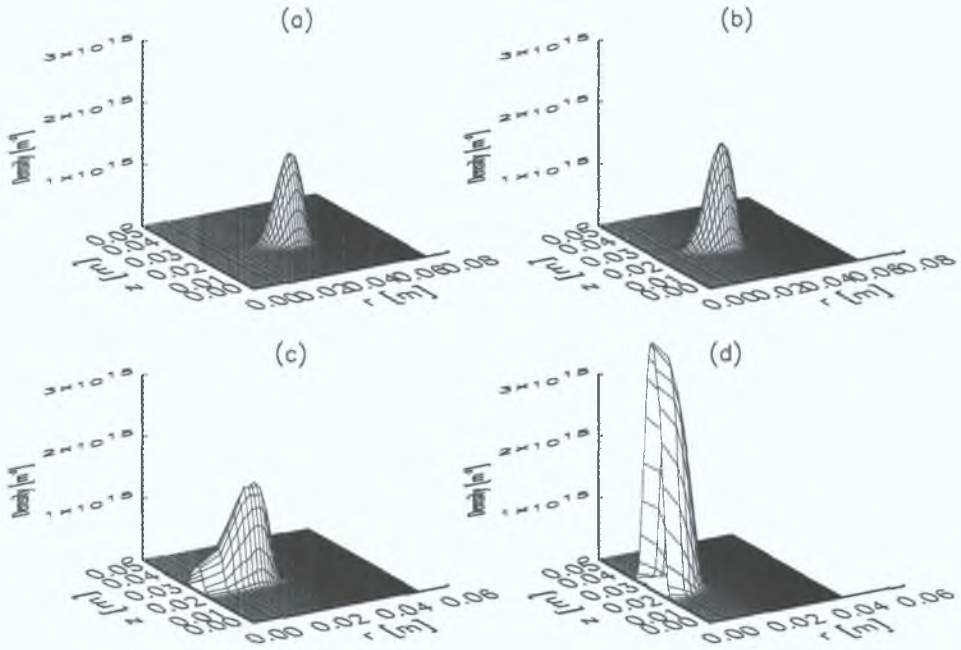

Figure 5.18: Time-averaged H^- density for (a) $r = 70$ mm, (b) $r = 60$ mm, (c) $r = 50$ mm, (d) $r = 40$ mm; $d = 50$ mm.

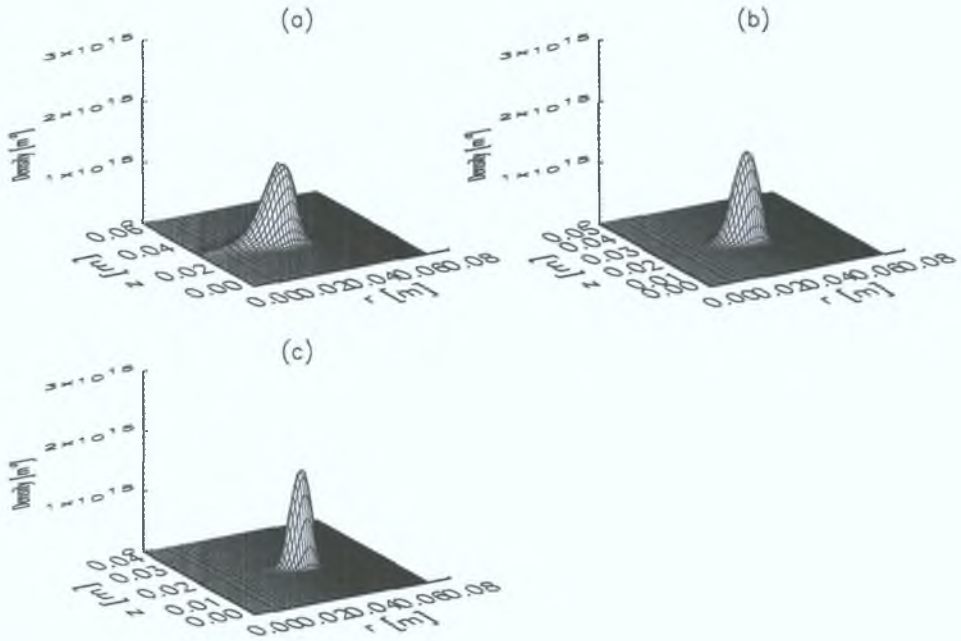

Figure 5.19: Time-averaged H^- density for (a) $d = 60$ mm, (b) $d = 50$ mm, (c) $d = 40$ mm; $r = 70$ mm.

maximum goes even further away from the cylindrical axis

In this section the coupling scheme described in chapter 4 has been used to model self-consistently rf capacitively coupled H_2 plasma discharges in 1D and in 2D The inclusion of H^- in the model has no significant effect on the EEDF, the electron heating rate and the behaviour of the plasma discharge The H^- density profile has a pronounced maximum in the centre of the spatial domain in 1D models and halfway between the electrodes in 2D models The H^- production by DA of $H_2(v)$ is modelled, with particular regard to the contribution associated to the different vibrational levels of H_2 In the 1D and 2D models compared, the relative contribution of the vibrational levels to the total H^- production rate is very different because of the different EEPFs in the two cases The different electron and $H_2(v)$ densities in the two models also contribute to make different the H^- production rates through DA of $H_2(v)$ Finally, the coupling scheme allows to hugely accelerate the H^- density convergence towards its value at the steady-state, if the rate constant of its main production and loss processes have a sufficiently low statistical error In the coupling scheme used that condition can always be satisfied by having a sufficiently large collision events statistics in the simulation for the collision process of interest

Chapter 6

Conclusions

In this thesis low temperature hydrogen rf plasmas discharges were modelled numerically by using both global model and PIC simulation.

A global model of rf inductively coupled hydrogen plasma discharges created in the DENISE experiment, including negative ions, assumed to be mainly produced by dissociative attachment of $H_2(0 \leq v \leq 9)$, was implemented in the GMS code. The values of the electron density and of the electron temperature obtained using GMS compare well with measurements in DENISE. H_3^+ is the dominant positive ion species in the pressure range considered for input power values around a few hundred watts, while the H^+ density reaches the same order of magnitude or becomes higher than the H_3^+ density if the power is a few thousand watts. The negative ion densities obtained are always far less than 0.1 of the electron density even under the most favourable assumptions.

The implementation of the PIC method in EPIC, the numerical code developed and used to perform the work presented in this thesis, has been explained, tested and validated.

A new numerical scheme coupling the PIC and the global model methods was devised and implemented to model rf capacitively coupled hydrogen

plasma discharges, including the effects of the chemistry in the discharge In the scheme a PIC code and a suitably modified version of the global model code are made interact by exchanging information The features and the advantages of this scheme were explained in detail along with the additions and changes to be made to EPIC and GMS to implement it

Several applications of the numerical scheme were then presented Firstly, the effect of the inclusion of various collision processes in the 1D model of an rf capacitively coupled H_2 plasma discharge at certain fixed values of the control parameters have been considered The inclusion in the model of rotational and vibrational excitations has the biggest effect on the EEDF, virtually changing the EEDF from a Maxwellian to a bi-Maxwellian in the case considered Secondly, it was shown that the assumption of Maxwellian EEDF in the calculation of $\mathcal{E}_L$, the energy cost per electron-ion pair created, in cases where the EEDF obtained self-consistently in the simulation is clearly non-Maxwellian strongly affects the result, that may be much bigger than the real value of $\mathcal{E}_L$, calculated by using the EEDF obtained from the PIC simulation without making any assumption Thirdly, the scheme was also used to obtain the energy distribution function of positive ions arriving at the central area of the grounded electrode in 2D simulations in cylindrical geometry of rf capacitively coupled H_2 plasma discharges Some distributions were compared with the energy distributions measured in the CIRIS experiment, giving a reasonable agreement Collisions in the sheath affect the energy distributions of the three positive ion species included in the model H_3^+, H_2^+ and H^+ Finally, negative ions were included in the simulation of rf capacitively coupled hydrogen plasma discharges and the coupling scheme was used to model self-consistently their production by dissociative attachment of $H_2(0 \leq v \leq 9)$ The H^- density profile has a pronounced maximum in the centre of the spatial domain

in 1D models and halfway between the electrodes in 2D models in cylindrical geometry. The inclusion of H^- in the model has no significant effect on the EEDF, the electron heating rate and the behaviour of the plasma discharge. In the 1D and 2D models compared, the relative contribution of the vibrational levels to the total H^- production rate by DA of $H_2(v)$ is very different because of the different EEPFs in the two cases. The coupling scheme allows to hugely accelerate the H^- density convergence towards its value at the steady-state.

There are many possible developments of the work presented in this thesis. It would be interesting to adapt the global model to the geometry of the Applied Radio frequency Ion Source (ARIS) [94], made of an inductively coupled plasma source with adjacent plasma diffusion chamber, having different sizes than the source chamber. The aim would be to obtain the global model results for the plasmas obtained in the two regions, which may have very different densities of the species included in the model and electron temperature. An obvious improvement in EPIC would be the implementation of binary collisions between simulated particles, that unfortunately could not be done only because there was not enough time. Another improvement in EPIC that would not be difficult to implement is the addition of the angle distributions of the ions arriving at the chamber boundary and the distributions both on the energy and the angle. Finally, to model the effects due to non uniformities of the neutral densities, it would be necessary to calculate the neutral densities with an improved modelling of the neutral transport.

Appendix A

Motion equations in cylindrical geometry

Let us assume a particle is in the position

$$\mathbf{r}(t) = (r(t), z(t), \theta(t)) \tag{A 1}$$

and has velocity

$$\mathbf{v} = (v_r, v_z, v_\theta) \tag{A 2}$$

in a cylindrical coordinates frame If the particle evolves for a time Δt so small that the velocity components and the orientation of the reference frame for the velocity do not change dramatically, then

$$r(t + \Delta t) = \sqrt{(r(t) + v_r \Delta t)^2 + (v_\theta \Delta t)^2} \tag{A 3}$$

$$z(t + \Delta t) = z(t) + v_z \Delta t \tag{A 4}$$

and by defining the rotation angle φ as

$$\varphi = tan^{-1}(\frac{v_\theta(t)\Delta t}{r(t) + v_r \Delta t}) \tag{A 5}$$

we obtain the component of the velocity with respect to the reference frame at the new particle position

$$v_r^{new}(t) = v_r(t)cos(\varphi) + v_\theta(t)sin(\varphi) \quad \text{(A 6)}$$

$$v_\theta^{new}(t) = -v_r(t)sin(\varphi) + v_\theta(t)cos(\varphi) \quad \text{(A 7)}$$

$$v_z^{new}(t) = v_z(t), \quad \text{(A 8)}$$

which are used to calculate the values of the velocities at a later time

$$v_r(t+\Delta t) = v_r^{new}(t) + \frac{q}{m}E_r\Delta t \quad \text{(A 9)}$$

$$v_z(t+\Delta t) = v_z^{new}(t) + \frac{q}{m}E_z\Delta t \quad \text{(A 10)}$$

$$v_\theta(t+\Delta t) = v_\theta^{new}(t) \quad \text{(A 11)}$$

Appendix B

Solution of tridiagonal systems of linear algebraic equations

Systems of N linear algebraic equations of the kind

$$b_1 x_1 + c_1 x_2 = d_1 \tag{B.1}$$

$$a_i x_{i-1} + b_i x_i + c_i x_{i+1} = d_i; \quad i = 2, N-1 \tag{B.2}$$

$$a_1 x_{N-1} + b_N x_N = d_N \tag{B.3}$$

can be expressed in matrix form as $\mathbf{A} \cdot \mathbf{x} = \mathbf{d}$, where $\mathbf{A}$ is a tridiagonal matrix, so called because it has non-zero elements only in the main diagonal and in the two adjacent diagonals. A fast recursive method, taking $O(N)$ operations, to solve system of equations of that kind is here described [95]. By introducing auxiliary variables g_i and h_i and using the recursive ansatz

$$x_{i+1} = g_i x_i + h_i; \quad i = 1, ..., N-1 \tag{B.4}$$

in the system of equations, the downward recursion formulae

$$g_{N-1} = -\frac{a_N}{b_N}\ ,\ h_{N-1} = \frac{d_N}{b_N} \tag{B.5}$$

$$g_{i-1} = -\frac{a_i}{b_i + c_i g_i}\ ,\ h_{i-1} = \frac{d_i - c_i h_i}{b_i + c_i g_i} \tag{B.6}$$

are obtained The values of g_i and h_i are known $\forall i = 1, N-1$, therefore by using the ansatz B 4 for $i = 1$ in equation B 1, we obtain

$$x_1 = \frac{d_1 - c_1 h_1}{b_1 + c_1 g_1} \tag{B 7}$$

The remaining unknown x_2, , x_N are then calculated in this order by using again the ansatz B 4 for $i = 1, N-1$

Appendix C

The Dynamic Alternate Direction Implicit method

The Alternate Direction Implicit (ADI) method is a mesh-relaxation method that was developed to solve the time-dependent heat flow equation [76, p 182]

$$\frac{\partial \phi}{\partial t} = \nabla^2 \phi + q, \tag{C 1}$$

but can be used also to solve the Poisson equation with two spatial variables

$$-\nabla^2 \Phi = \frac{\rho}{\varepsilon}, \tag{C 2}$$

and consequently the Laplace equation, if a fictitious time derivative is added to the equation That is because the Laplace operator can be split in two operators L_1 and L_2

$$-\nabla^2 \Phi = L\Phi = (L_1 + L_2)\Phi, \tag{C 3}$$

each associated to the derivatives over one of the variables The expression of the equation to solve to obtain the solution of the Laplace equation is

$$\frac{\partial \Phi}{\partial t} = -(L_1 + L_2)\Phi + q, \tag{C 4}$$

that can be differenced implicitly in two half-steps as follows

$$\frac{\Phi^{n+\frac{1}{2}} - \Phi^n}{\frac{\Delta t}{2}} = -L_1\Phi^{n+\frac{1}{2}} - L_2\Phi^n + q \qquad \text{(C 5)}$$

$$\frac{\Phi^{n+1} - \Phi^{n+\frac{1}{2}}}{\frac{\Delta t}{2}} = -L_1\Phi^{n+\frac{1}{2}} - L_2\Phi^{n+1} + q \qquad \text{(C 6)}$$

and then the following expression for $\Phi^{n+\frac{1}{2}}$ and Φ^{n+1} are obtained

$$(I + \omega L_1)\Phi^{n+\frac{1}{2}} = (I - \omega L_2)\Phi^n + \omega q \qquad \text{(C 7)}$$

$$(I + \omega L_2)\Phi^{n+1} = (I - \omega L_1)\Phi^{n+\frac{1}{2}} + \omega q \qquad \text{(C 8)}$$

with $\omega = \frac{\Delta t}{2}$ L_1 and L_2 and therefore

The operators on the l h s of C 7 and C 8 are the sum of the identity I and of ω multiplied by the operators L_1 or L_2, which express the second derivative over one of the variables Both operators $(I + \omega L_1)$ and $(I + \omega L_2)$ can be expressed by tridiagonal matrices if the ordering of the mesh points is suitably chosen That means that for a fixed value of ω and by knowing Φ^n the system of equations C 7 and C 8 can be solved in sequence to obtain Φ^{n+1}, the latest estimate of the electric potential on the mesh points The procedure can be iterated until a certain convergence condition is satisfied In the ADI algorithm the value of ω is varied cyclically and can assume only certain values decided before the relaxation process starts [76, p 184] In the DADI algorithm [79], instead, to accelerate the relaxation process the value of ω is varied dynamically In this variant of ADI the solution obtained by solving the equations C 7 and C 8 twice with step $\frac{\omega}{2}$ is compared with the solution obtained by solving the equations C 7 and C 8 only once, but with step ω If the results significantly differ, then ω must decrease, otherwise it can be increased or the same value can be kept

Appendix D

The Buneman variant of the cyclic reduction method

The cyclic reduction method is a matrix method, more precisely a rapid elliptic solver, able to solve a set of N_g difference equations of certain classes in $O(N_g log_2 N_g)$ operations [76, p. 199]. The Poisson equation calculated in the points of the two dimensional meshes, whose points are chosen in the way defined in section 3.6, with $\Phi_i = 0$ in all boundary mesh points, produce a system of equations, that can be solved by the cyclic reduction method [76, p. 201], both in Cartesian and in cylindrical geometry.

If we store the values of the electric potential in the $j-th$ row of the mesh in

$$\phi_j = (\Phi_{1,j}, ..., \Phi_{M-1,j}) \tag{D.1}$$

and the values of the r.h.s of the difference equations in the $j-th$ row of the mesh in

$$h_j = (\frac{\rho_{1,j}}{\varepsilon}, \ldots, \frac{\rho_{M-1,j}}{\varepsilon}) \tag{D.2}$$

the system of equations 3.32 can be rewritten as

$$\phi_{j-1} + \Lambda\phi_j + \phi_{j+1} = h_j, \quad j = 1, N-1 \tag{D.3}$$

with Λ being the difference operator on the first variable in a generic row, for example in 2D Cartesian geometry the first term on the r h s of 3 31

If we sum the equations D 2 associated to the indices $j-1$ and $j+1$ to the one associated to the index j, multiplied by $-\Lambda$, the result is

$$\phi_{j-2} + \Lambda^{(1)}\phi_j + \phi_{j+2} = h_j^{(1)} \quad j = 2, 4, \quad , N-2 \tag{D 4}$$

with

$$\Lambda^{(1)} = 2I - \Lambda^2 \tag{D 5}$$

$$h_j^{(1)} = h_{j-1} - \Lambda h_j + h_{j+1} \tag{D 6}$$

By defining

$$h_j^{(0)} = h_j, \quad \forall j = 1, N-1 \tag{D 7}$$

$$\Lambda^{(0)} = \Lambda \tag{D 8}$$

$$h_j^{(r+1)} = h_{j-2^r}^{(r)} - \Lambda^{(r)} h_j^{(r)} + h_{j+2^r}^{(r)} \tag{D 9}$$

$$\Lambda^{(r+1)} = 2I - (\Lambda^{(r)})^2 \tag{D 10}$$

we can iterate the sum procedure and, if $N = 2^n$, after the $(n-1)$-th iteration the only equation remaining is

$$\phi_0 + \Lambda^{(n-1)}\phi_{\frac{N}{2}} + \phi_N = h_{\frac{N}{2}}^{(n-1)} \tag{D 11}$$

which can be rewritten as

$$\Lambda^{(n-1)}\phi_{\frac{N}{2}} = h_{\frac{N}{2}}^{(n-1)}, \tag{D 12}$$

because ϕ_0 and ϕ_N have all components set to 0 by the boundary condition The matrix $\Lambda^{(n-1)}$ by definition can be expressed as a product of $2^{(n-1)}$ tridiagonal matrixes

$$\Lambda^{(n-1)} = -\prod_{k=1}^{2^{(n-1)}} (\Lambda - \beta_k I) = -\prod_{k=1}^{2^{(n-1)}} \Lambda_k^{(n-1)} \tag{D 13}$$

because both I and Λ are tridiagonal The values β_k and therefore the tridiagonal matrixes $\Lambda_k^{(n-1)}$ are calculated by finding the $2^{(n-1)}$ roots of the polynomial $f_{n-1}(x)$ obtained by

$$f_0(x) = x, \quad f_{r+1}(x) = 2 - f_r^2(x), \tag{D 14}$$

associated to $\Lambda^{(n-1)}$ The solution of D 12 can then be obtained by solving $2^{(n-1)}$ system of linear equations expressed by a tridiagonal matrix with the algorithm described in appendix B

After that, by using the known values of ϕ_0, ϕ_N and the value $\phi_{\frac{N}{2}}$, just obtained, the 2 equations remaining at the $(n-2)$-th iteration can be solved in the same way to obtain $\phi_{\frac{N}{4}}$ and $\phi_{\frac{3}{4}N}$ By solving in a similar way the equations remaining at the earlier iterations, the values of the electric potential in all grid points can be calculated

To implement numerically this solution scheme it is necessary to use a formula alternative to D 9 to avoid numerical instability in the calculation In the Buneman variant of the cyclic reduction method [76, p 204] [80, 81], the formulae

$$h_j^{(r)} = \Lambda^{(r)} p_j^{(r)} + q_j^{(r)} \tag{D 15}$$

$$p_j^{(0)} = 0, \quad q_j^{(0)} = h_j, \quad \forall j = 1, N-1 \tag{D 16}$$

with

$$p_j^{(r)} = p_j^{(r-1)} - (\Lambda^{(r-1)})^{-1}(p_{j-2^{(r-1)}}^{(r-1)} + p_{j+2^{(r-1)}}^{(r-1)} - q_j^{(r-1)}) \tag{D 17}$$

$$q_j^{(r)} = q_{j-2^{(r-1)}}^{(r-1)} + q_{j+2^{(r-1)}}^{(r-1)} - 2p_j^{(r)} \tag{D 18}$$

are used instead of D 9

Theorem D 1 *Formulae D 15-D 18 are equivalent to D 9*

Starting from D 15 and D 17-D 18 we have

$$h_j^{(r)} = \Lambda^{(r)} p_j^{(r)} + q_j^{(r)} =$$
$$\Lambda^{(r)}[p_j^{(r-1)} - (\Lambda^{(r-1)})^{-1}(p_{j-2^{(r-1)}}^{(r-1)} + p_{j+2^{(r-1)}}^{(r-1)} - q_j^{(r-1)})] +$$
$$q_{j-2^{(r-1)}}^{(r-1)} + q_{j+2^{(r-1)}}^{(r-1)} - 2p_j^{(r)} \qquad \text{(D 19)}$$

and by using D 10 and D 17 again we obtain

$$h_j^{(r)} =$$
$$[2I - (\Lambda^{(r-1)})^2][p_j^{(r-1)} - (\Lambda^{(r-1)})^{-1}(p_{j-2^{(r-1)}}^{(r-1)} + p_{j+2^{(r-1)}}^{(r-1)} - q_j^{(r-1)})] +$$
$$q_{j-2^{(r-1)}}^{(r-1)} + q_{j+2^{(r-1)}}^{(r-1)} - 2p_j^{(r-1)} -$$
$$2(\Lambda^{(r-1)})^{-1}(p_{j-2^{(r-1)}}^{(r-1)} + p_{j+2^{(r-1)}}^{(r-1)} - q_j^{(r-1)}) \qquad \text{(D 20)}$$

and by eliminating the opposite terms

$$h_j^{(r)} =$$
$$-(\Lambda^{(r-1)})^2 p_j^{(r-1)} + \Lambda^{(r-1)}(p_{j-2^{(r-1)}}^{(r-1)} + p_{j+2^{(r-1)}}^{(r-1)} - q_j^{(r-1)}) +$$
$$q_{j-2^{(r-1)}}^{(r-1)} + q_{j+2^{(r-1)}}^{(r-1)} \qquad \text{(D 21)}$$

and suitably rearranging the remaining terms

$$h_j^{(r)} =$$
$$[\Lambda^{(r-1)} p_{j-2^{(r-1)}}^{(r-1)} + q_{j-2^{(r-1)}}^{(r-1)}] - \Lambda^{(r-1)}[(\Lambda^{(r-1)}) p_j^{(r-1)} + q_j^{(r-1)}] +$$
$$[\Lambda^{(r-1)} p_{j+2^{(r-1)}}^{(r-1)} + q_{j+2^{(r-1)}}^{(r-1)}], \qquad \text{(D 22)}$$

and using D 15 finally we obtain D 9 QED

Appendix E

Comparison of 2-D models of rf capacitive argon discharges

In this appendix some results of a 2-D model in Cartesian geometry of an rf capacitively coupled argon plasma discharge, obtained by using EPIC, are presented and compared with results presented in [31], with the same feedstock gas and geometry. This is done to test and validate EPIC, particularly for the parts of the code used both in the 2-D Cartesian and in the 2-D cylindrical geometry case. For this purposes argon was chosen as feedstock gas instead of hydrogen, because of the much simpler set of collision processes, listed in table E.1, that can be used. The simulated system, shown in figure E.1, is made of a two-dimensional chamber, whose length is $L_x = 40\,\text{mm}$ and height is $L_y = 50\,\text{mm}$. A vertical powered electrode, whose height is $L_{el} = 30\,\text{mm}$, lies at the centre of the left boundary and is connected to the power source and a blocking capacitor having capacitance $C_B = 500\,\text{pF}$. The rest of the boundary belongs to the grounded electrode, except two vacuum dielectric regions, a few millimetres wide, between the powered and grounded electrode. All results presented in this appendix have been obtained with the pressure set

Table E 1 Collision processes used for modelling a low pressure rf plasma discharge, with Argon as feedstock gas

Collision process	Type
$e + Ar \longrightarrow e + Ar$	Elastic scattering
$e + Ar \longrightarrow e + Ar^*$	Excitation
$e + Ar \longrightarrow e + e + Ar^+$	Ionization
$Ar^+ + Ar \longrightarrow Ar^+ + Ar$	Elastic scattering
$Ar^+ + Ar \longrightarrow Ar + Ar^+$	Charge exchange

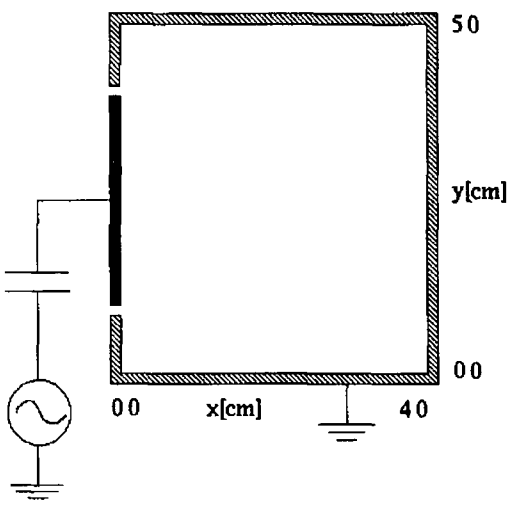

Figure E 1 The simulated system

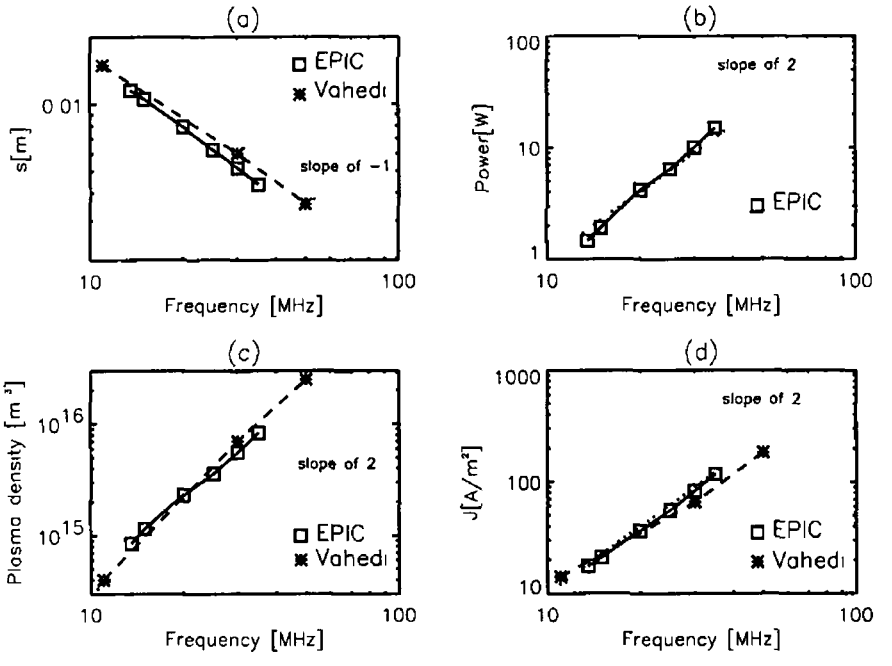

Figure E 2 Logarithmic plot of (a) sheath width at the driven electrode, (b) dissipated power, (c) plasma density at the centre of the chamber and (d) rf current density vs driving frequency

to 10 mTorr and with the amplitude of the applied rf voltage set to 200 Volt The only control parameter changed is the driving frequency

In [31] the results obtained were compared to frequency scaling predictions for capacitive rf discharges In figure E 2 (a) the plot of the sheath width s_D at the powered electrode versus the driving frequency f is shown The sheath widths s_D calculated by both models vary approximately as $s_D \propto f^{-1}$, as predicted [31] In figure E 2 (b)-(d) the power absorbed by the plasma in EPIC, the plasma density and the rf current density at the driven electrode versus the driving frequency f are shown They all show roughly quadratic dependence on f and EPIC results fit well with the results obtained in [31] The biggest difference is in the graph of the sheath width, which perhaps is due to the different condition required to determine the sheath-edge in the two

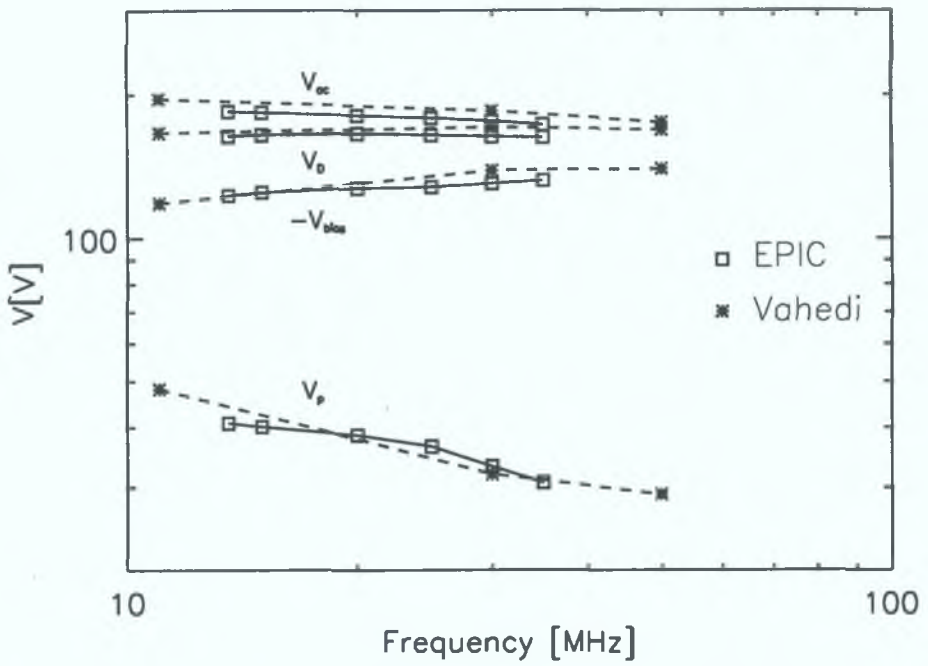

Figure E.3: Plot of the rf voltage at the driven electrode, V_{ac}, the plasma potential V_p, the bias voltage at the driven electrode, V_{bias} and the plasma to driven electrode voltage, V_D vs. driving frequency.

codes. In [31] it is not mentioned how the sheath-edge position is determined. Instead in EPIC, by moving perpendicularly to the powered electrode, from the centre of the electrode itself to the inside of the chamber, the position of the sheath-edge is the position of the first examined mesh point where the quasi-neutrality condition is approximately satisfied. That means the first mesh point where the ratio of the time-averaged charge density over the time-averaged total positive ion density is less than a certain value.

In figure E.3 the rf voltage at the driven electrode, V_{ac}, the plasma potential V_p, the bias voltage at the driven electrode, V_{bias} and the plasma to driven electrode voltage, V_D, are plotted versus the driving frequency. The results of the two models fit reasonably well. The biggest difference would seem to be in the values of V_p below 30 MHz, but perhaps further results of the two models

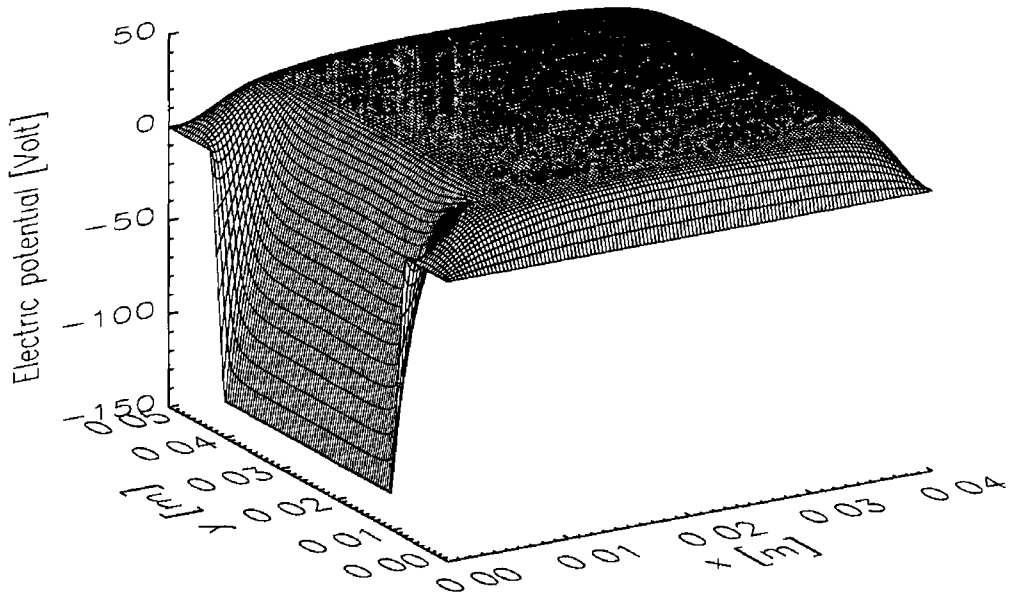

Figure E 4 Time-averaged electric potential in the system at the driving frequency of 30 MHz vs space

below 30 MHz, taken at the same value of the frequency would give a better agreement

In figure E 4 the spatial profile of the time averaged electric potential at the driving frequency of 30 MHz is shown The plasma to driven electrode voltage, V_D, is much bigger than the plasma potential V_p, because of the high value of the ratio between the areas of the grounded electrode and of the powered electrode [11, p 368]

The comparison of the results of a 2-D model in Cartesian geometry of an rf capacitively coupled argon plasma discharge, obtained by using EPIC, with the results presented in [31], with the same feedstock gas, geometry and values of the control parameters, validates the implementation of the PIC/MC method given in EPIC for the case studied

Appendix F

A possible choice of $f(r_d - 1)$ to calculate r_w

The choose the function $f(r_d - 1)$ used to calculate r_w in order to modify the particle weight of the PIC simulation according to the global model estimation of that (expressed by the quantity r_d) as explained in section 4 3, the following criterion has been used the closer the simulated system is to the steady state (according to the global model results) the less has to be perturbed by a particle weight change This criterion is implemented in the function

$$f(x, A, p) = [1 - \exp(-\log(\frac{A}{A-1}\frac{|x|}{p}))]Ax, \quad A > 1, \quad p > 0 \qquad \text{(F 1)}$$

having the following properties

$$f(x = 0, A, p) = 0 \qquad \text{(F 2)}$$

$$f(x = p, A, p) = p \qquad \text{(F 3)}$$

$$\lim_{x \to \infty} f(x, A, p) = Ax \qquad \text{(F 4)}$$

The parameters A and p have to be empirically chosen in the given allowed ranges to accelerate the convergence of the simulated system without perturbing it excessively For any chosen pair of allowed values of the parameters

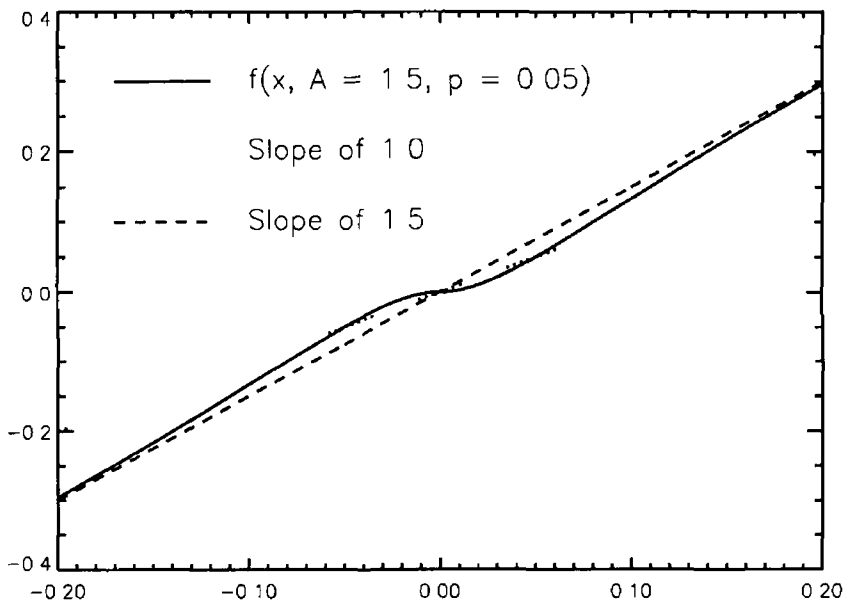

Figure F 1 Graph of $f(x, A = 1\ 5, p = 0\ 05)$ in the range $[-0\ 2, 0\ 2]$

A and p, the function $f(x, A, p)$ has always the trend required by the chosen criterion In figure F 1 the function $f(x, A = 1\ 5, p = 0\ 05)$ is plotted in the range $[-0\ 2, 0\ 2]$ It is evident that the properties F 2- F 4 are satisfied and the closer to zero is x the lower is the ratio $f(x, A, p)/x$, as requested by the chosen criterion However this function can be used only if $f > -1\ 0$ (which should always be the case), because otherwise the particle weight in the simulation will become negative

Bibliography

[1] F A Chen *Plasma physics and controlled fusion*, volume 1 Plasma Physics Plenum Press, 2nd edition, 1984

[2] R O Dendy, editor *Plasma physics an introductory course* Cambridge University Press, 1993

[3] J J Duderstadt and G A Moses *Inertial confinement fusion* John Wiley & Sons, 1982

[4] D B Graves Plasma processing *IEEE Trans on Plasma Science*, 22(1) 31–42, 1994

[5] N Hershkowitz Role of plasma aided manufacturing in semiconductor fabrication *IEEE Trans on Plasma Science*, 26(6) 1610–1620, 1998

[6] J T Dakin Nonequilibrium lighting plasmas *IEEE Trans on Plasma Science*, 19(6) 991–1002, 1991

[7] J F Waymouth Lte and near-lte lighting plasmas *IEEE Trans on Plasma Science*, 19(6) 1003–1012, 1991

[8] A Sobel Plasma displays *IEEE Trans on Plasma Science*, 19(6) 1032–1047, 1991

[9] Th. Callegari, R. Ganter, and J.-P. Boeuf. Diagnostic and modeling of a macroscopic plasma display panel cell. *J. Appl. Phys.*, 88(7):3905–3913, 2000.

[10] H. Conrads and M. Schmidt. Plasma generation and plasma sources. *Plasma Sources Sci. Technol.*, 9(4):441–454, 2000.

[11] M.A. Lieberman and A.J. Lichtenberg. *Principles of Plasma Discharges and Material Processing.* John Wiley & Sons, New York, USA, 1994.

[12] R.A. Cairns. *Radiofrequency heating of plasmas.* Plasma physics. Adam Hilger, 1991.

[13] Y. Ohara. Development of high power ion sources for fusion. *Rev. Sci. Instrum.*, 69(2):908–913, 1998.

[14] R. Aymar. The ITER project. *IEEE Trans. on Plasma Science*, 25(6):1187–1195, 1997.

[15] K.W. Ehlers. High current negative ion sources (invited). *Rev. Sci. Instrum.*, 61(1):662–664, 1990.

[16] M. Bacal and G.W. Hamilton. H^- and D^- production in plasmas. *Phys. Rev. Lett.*, 42(23):1538–40, 1979.

[17] W.G. Graham. The kinetics of negative hydrogen ions in discharges. *Plasma Sources Sci. Technol.*, 4(2):281–292, 1995.

[18] D. Riz and J. Pamela. Modeling of negative ion transport in a plasma source. *Rev. Sci. Instrum.*, 69(2):914–919, 1998.

[19] K.N. Leung, C.A. Hauck, W.B. Kunkel, and S.R. Walther. Optimization of H^- production from a small multicusp ion source. *Rev. Sci. Instrum.*, 60(4):531–538, 1989.

[20] C Lee, D B Graves, M A Lieberman, and D W Hess Global model of plasma chemistry in a high density oxygen discharge *J Electrochem Soc* , 141(6) 1547–1555, 1994

[21] C Lee and M A Lieberman Global model of Ar, O_2, Cl_2 and Ar/O_2 high density plasma discharges *J Vac Sci Technol A*, 13(2) 368–380, 1995

[22] Y T Lee, M A Lieberman, A J Lichtenberg, F Bose, H Baltes, and R Patrick Global model for high pressure electronegative radio-frequency discharges *J Vac Sci Technol A*, 15(1) 113–126, 1997

[23] R Zorat, J Goss, D Boilson, and D Vender Global model of a radiofrequency H_2 plasma discharge in DENISE *Plasma Sources Sci Technol* , 9(2) 161–168, 2000

[24] R Zorat and D Vender Global model for an rf hydrogen inductive plasma discharge in the deuterium negative ion source experiment including negative ions *J Phys D Appl Phys* , 33(14) 1728–1735, 2000

[25] J -P Boeuf Numerical model of rf glow discharges *Phys Rev A*, 36(6) 2782–2792, 1987

[26] R A Stewart, P Vitello, and D B Graves Two-dimensional fluid model of high density inductively coupled plasma sources *J Vac Sci Technol B*, 12(1) 478–485, 1994

[27] M M Meyyappan and J P Kreskovsky Glow discharge simulation through solutions to the moments of the Boltzmann transport equation *J Appl Phys* , 68(4) 1506–1512, 1990

[28] D Vender and R W Boswell Numerical modeling of low-pressure rf plasmas *IEEE Trans on Plasma Science*, 18(4) 725–732, 1990

[29] C.K. Birdsall. Particle-In-Cell charged-particle simulations, plus Monte Carlo collisions with neutral atoms, PIC-MCC. *IEEE Trans. on Plasma Science*, 19(2):65–85, 1991.

[30] M. Surendra and D.B. Graves. Particle simulation of radio-frequency glow discharges. *IEEE Trans. on Plasma Science*, 19(2):144–157, 1991.

[31] V. Vahedi, C.K. Birdsall, M.A. Lieberman, G. DiPeso, and T.D.Rognlien. Verification of frequency scaling laws for capacitive radio-frequency discharges using two-dimensional simulations. *Phys. Fluids. B*, 5:2719–2729, 1993.

[32] V. Vahedi, G. DiPeso, C.K. Birdsall, M.A. Lieberman, and T.D. Rognlien. Capacitive rf discharges modelled by Particle-In-Cell Monte Carlo simulation. I: analysis of numerical techniques. *Plasma Sources Sci. Technol.*, 2(4):261–272, 1993.

[33] V. Vahedi and M. Surendra. A Monte Carlo collision model for the Particle-In-Cell method: applications to argon and oxygen discharges. *Comput. Phys. Commun.*, 87:179–198, 1995.

[34] D.J. Economou, T.J. Bartel, R.S. Wise, and D.S. Lymberopoulos. Two-dimensional Direct Simulation Monte Carlo (DSMC) of reactive neutral and ion flow in high density plasma reactor. *IEEE Trans. on Plasma Science*, 23(4):581–590, 1995.

[35] C. Wu, C. Li, J. Tsai, and F.F. Young. Solving the Boltzmann equation in a 2-D-configuration and 2-D-velocity space for capacitively coupled rf discharges. *IEEE Trans. on Plasma Science*, 23(4):650–660, 1995.

[36] W.N.G. Hitchon, D.J. Koch, and J.B.Adams. An efficient scheme for convection-dominated transport. *J. Comput. Phys.*, 83:79–95, 1989.

[37] T J Sommerer, W N G Hitchon, R E P Harvey, and J E Lawler Self-consistent kinetic calculations of helium rf glow discharges *Phys Rev A*, 43(8) 4452–4472, 1991

[38] C Chen, T Wei, L R Collins, and J Phillips Modelling the discharge region of a microwave generated hydrogen plasma *J Phys D Appl Phys* , 32(6) 688–698, 1999

[39] N Sato and H Tagashira A hybrid Monte Carlo/fluid model of RF plasmas in SiH_4/H_2 mixture *IEEE Trans on Plasma Science*, 19(2) 102–112, 1991

[40] J -P Boeuf and L C Pitchford Pseudospark discharges via computer simulation *IEEE Trans on Plasma Science*, 19(2) 286–296, 1991

[41] P L G Ventzek, R J Hoekstra, and M J Kushner Two-dimensional modeling of high plasma density inductively coupled sources for materials processing *J Vac Sci Technol B*, 12(1) 461–477, 1994

[42] A Bogaerts, R Gijbels, and W Goedheer Hybrid modeling of a capacitively coupled radio frequency glow discharge in argon combined Monte Carlo and fluid model *Jpn J Appl Phys* , 38(7B) 4404–4415, 1999

[43] I B Bernstein and T Holstein Electron energy distribution in stationary discharges *Phys Rev* , 94 1475, 1954

[44] L D Tsendin Energy distribution of electrons in a weakly ionized current-carrying plasma with a transverse inhomogeneity *Sov Phys JETP*, 39 805, 1974

[45] V V Serikov, S Kawamoto, and K Nanbu Particle-in-Cell plus Direct Simulation Monte Carlo (PIC-DSMC) approach for self-consistent plasma gas simulations *IEEE Trans on Plasma Science*, 27(5) 1389–1398, 1999

[46] P McNeely, D Boilson, N Curran, M Hopkins, and D Vender Recommissioning the deuterium negative ion source experiment ion source for studies in support of ignition device to test engineering concepts *Rev Sci Instrum* , 69(2) 983–985, 1998

[47] J T Gudmundsson and M A Lieberman Model and neasurements for a planar inductive oxygen discharge *Plasma Sources Sci Technol* , 7(1) 1–12, 1998

[48] R B Bird, W E Stewart, and E N Lightfoot *Transport Phenomena*, chapter 16, page 511 John Wiley & Sons, Inc , 1960

[49] J F O'Hanlon *A user's guide to vacuum technology*, page 33 John Wiley & Sons, Inc , 1989

[50] V A Godyak *Soviet Radio Frequency Discharge Research* Delphic Associates, Falls Church, VA, USA, 1986

[51] J D Huba *1998 Revised NRL plasma formulary*, page 39 Naval Research Laboratory, 1998

[52] W H Press, B P Flannery, S A Teulkosky, and W T Vetterling *Numerical recipes in C, The art of scientific Computing*, chapter 8, page 272 Cambridge University Press, 1986

[53] H C Straub, B M Renault, B G Lindsay, K A Smith, and R F Stebbings Absolute partial cross sections for electron-impact ionization of H_2,

N_2, and O_2 from threshold to 1000 ev. *Phys. Rev. A*, 54(3):2146–2153, 1996.

[54] C. Gorse, R. Celiberto, M. Cacciatore, A. Laganà, and J. Bretagne. From dynamics to modeling of plasma complex systems: negative ion (H^-) sources. *Chem. Phys.*, 117(1-2):177–195, 1987.

[55] D.T. Stibbe and J. Tennyson. Near-threshold electron impact dissociation of H_2 within the adiabatic nuclei approximation. *New Journal of Physics*, 1:2.1–2.9, 1998. `http://www.njp.org/`.

[56] A.P.P. Natalense, C.S. Sartori, L.G. Ferreira, and M.A.P. Lima. Electronic excitation of H_2 by electron impact using soft norm-conserving pseudopotentials. *Phys. Rev. A*, 54(6):5435–5437, 1996.

[57] H. Tawara, Y. Itikawa, H. Nishimura, and M. Yoshino. Cross sections and related data for electron collisions with hydrogen molecules and molecular ions. *J. Phys. Chem. Ref. Data*, 19(3):617–636, 1990.

[58] K. Onda. Low energy heavy particle collisions relevant to gas divertor physics. In H. Tawara, editor, *Present status on atomic and molecular date relevant to fusion plasma diagnostic and modeling*, number 39 in NIFS-DATA, pages 62–76. National Institute for Fusion Science, Nagoya, Japan, 1997.

[59] Hong Gao. Vibrational excitation of H_2 by electron impact: An energy-dependent vibrational-frame-transformation approach. *Phys. Rev. A*, 45(9):6895–6898, 1992.

[60] J.R. Hiskes. Atomic processes, cross sections, and reaction rates necessary for modeling hydrogen negative-ion sources and identification of optimum H^- current densities. *Rev. Sci. Instrum.*, 63(4):2702–2704, 1992.

[61] R K Janev, W D Langer K Jr Evans, and D E Jr Post *Elementary processes in Hydrogen-Helium plasmas* Springer Verlag, Berlin, Germany, 1987

[62] C F Barnett, editor *Collisions of H, H_2, He and Li atoms and ions with atoms and molecules*, volume 1 Oak Ridge National Laboratory, Tennesee, USA, 1990 ORNL-6086

[63] C Gorse, M Capitelli, M Bacal, J Bretagne, and A Laganà Progress in the non-equilibrium vibrational kinetics of hydrogen in magnetic multicusp H^- ion sources *Chem Phys* , 117(1-2) 177–195, 1987

[64] J R Hiskes and A M Karo Analysis of the H_2 vibrational distribution m a a hydrogen discharge *Appl Phys Lett* , 54(6) 508–510, 1989

[65] P Berlemont, D A Skinner, and M Bacal Negative ion volume production model state of the experimental confirmation *Rev Sci Instrum* , 64(10) 2721–2728, 1993

[66] L A Pinnaduwage and L G Christophorou Verification of H^- formation m ultraviolet-laser irradiated hydrogen implications for negative ion and neutral beam technologies *J Appl Phys* , 76(1) 46–54, 1994

[67] J R Hyskes Molecular Rydberg states in hydrogen negative ion discharges *Appl Phys Lett* , 69(6) 755–757, 1996

[68] P L Gertitchke and W Domcke Time-dependent wave-packet description of dissociative electron attachment *Phys Rev A*, 47(2) 1031–1044, 1993

[69] J M Wadhera and J N Bardsley Vibrational- and rotational-state dependence of dissociative attachment in e-H_2 collisions *Phys Rev Lett* , 41(26) 1795–1798, 1978

[70] W.F. Bailey and A. Garscadden. Production of negative ions under non-equilibrium conditions. In Th. Sluters, editor, *Proceedings of the second international symposium on the production and neutralization of negative ions and beams*, pages 33–41, Upton, NY, USA, 1980.

[71] M.J.J. Eerden, M.C.M. van de Sanden, D.K. Otorbaev, and D.C. Schram. Cross section for the mutual neutralization reaction $H_2^+ + H^-$, calculated in a multiple-crossing Landau-Zener approximation. *Phys. Rev. A*, 51(4):3362–3365, 1995.

[72] M. Capitelli, C. Gorse, P. Berlemont, D.A. Skinner, and M. Bacal. Theoretical non-equilibrium electron energy and vibrational distributions of H_2 in magnetic multicusp plasmas: an analysis of the input cross section data. *Chem. Phys. Lett.*, 179(1-2):48–51, 1991.

[73] P.J. Eenshuistra, M. Gochitashvili, R. Becker, A.W. Kleyn, and H.J. Hopman. Negative hydrogen ion densities and drift velocities in a multicusp ion source. *J. Appl. Phys.*, 67(1):85–96, 1990.

[74] A.M. Bruneteau, G. Hollos, M. Bacal, and J. Bretagne. Temperature and relative density of atomic hydrogen in a multicusp H^- volume source. *J. Appl. Phys.*, 67(12):7254–7264, 1990.

[75] C.K. Birdsall and A.B. Langdon. *Plasma physics via computer simulation.* McGraw-Hill Book Company, New York, 1985.

[76] R.W. Hockney and J.W. Eastwood. *Computer simulation using particles.* Institute of Physics Publishing, Bristol and Philadelphia, 1988.

[77] M.A. Lieberman, J.P. Booth, P. Chabert, J.M. Rax, and M.M. Turner. Standing wave and skin effects in large-area, high-frequency capacitive discharges. *Plasma Sources Sci. Technol.*, 11(3):283–293, 2000.

[78] J P Verboncoeur, M V Alves, V Vahedi, and C K Birdsall Simultaneous potential and circuit solution for 1D bounded plasma particle simulation codes *J Comput Phys* , 104 321–328, 1993

[79] D J Larson D H Hewett and S Doss Solution of simultaneous partial differential equations using dynamic ADI solution of the streamlined darwin field equations *J Comput Phys* , 101 11–24, 1992

[80] J Stoer and R Bulirsch *Introduction to numerical analysis* Springer Verlag, New York and Berlin Heidelberg, 1980

[81] G H Golub B L Buzbee and C W Nielson On direct methods to solve Poisson's equation *SIAM J Numer Anal* , 7(4) 627–656, 1999

[82] V Vahedi and G DiPeso Simultaneous potential and circuit solution for two-dimensional bounded plasma simulation codes *J Comput Phys* , 5 149–163, 1997

[83] M Allan and S F Wong Effect of vibrational and rotational excitation on dissociative attachment in hydrogen *Phys Rev Lett* , 41(26) 1791–1794, 1978

[84] T Šimko, V Martišovitš, J Bretagne, and G Gousset Computer simulations of H^+ and H_3^+ transport parameters in hydrogen drift tubes *Phys Rev E*, 56(5) 5908–5919, 1997

[85] A V Phelps Cross sections and swarm coefficients for H^+, H_2^+, H_3^+, H, H_2 and H^- in H_2 for energies from 0 1 eV to 10 keV *J Phys Chem Ref Data*, 19(3) 653–675, 1990

[86] S.J. Buckman and A.M. Phelps. JILA Information Center. Technical Report 27, University of Colorado, 1985. `ftp://jila.colorado.edu/collision_data`.

[87] R.K. Janev, editor. *Atomic and molecular processes in fusion edge plasmas*, page 41. Plenum press, New York, 1995.

[88] V. A. Godyak and R. B. Piejak. Abnormally low electron temperature and heating transition in a low-pressure rf discharge at 13.56 MHz. *Phys. Rev. Lett.*, 65(8):996–999, 1990.

[89] M. M. Turner, R. A. Doyle, and M. B. Hopkins. Measured and simulated electron energy distribution functions in a low-pressure radio frequency discharge in argon. *Appl. Phys. Lett.*, 62(25):3247–3249, 1993.

[90] E. Kawamura, V. Vahedi, M.A. Lieberman, and C.K. Birdsall. Ion energy distributions in rf sheats; review, analysis and simulation. *Plasma Sources Sci. Technol.*, 8(3):R45–64, 1999.

[91] R. Zorat, D. O'Connell, D. Vender, M.M. Turner, and A.R. Ellingboe. 2D model of an rf hydrogen plasma and comparison with ion energy distribution measurements. In R. d'Agostino, P. Favia, F. Fracassi, and F. Palumbo, editors, *16th International Symposium on Plasma Chemistry, abstracts and full-papers CD*, page 212, Taormina, ITALY, June 2003.

[92] C. Wild and P. Koidl. Ion and electron dynamics in the sheath of radio-frequency glow discharges. *J. Appl. Phys.*, 69(5):2909–2922, 1991.

[93] Y. Xu, G.A. Gallup, and I.I. Fabrikant. Dissociative electron attachment to vibrationally and rotationally excited H_2 and HF molecules. *Phys. Rev. A*, 61(5):052705, 2000.

[94] F. Soberón, R. Faulkner, and A.R. Ellingboe. Plasma diffusion into a picket-fence magnetic field in ARIS (Applied Radio-frequency Inductive Source). In Santolo De Benedictis and Giorgio Dilecce, editors, *Proceedings of Frontiers in Low Temperature Plasma Diagnostics V*, pages 172–175, Villaggio Cardigliano, Specchia (LE), April 2003. Organizing Committee Workshop FLTPDV, Bari, Italy.

[95] F.J. Vesely. *Computational physics. An introduction*, pages 30–31. Plenum, New York, USA, 1993.